Studying protein-ligand binding by spectroscopy and calorimetry

Erick Alejandro Meneses Ramirez

Degree of Doctor of Philosophy

Department of Chemistry

McGill University

Montreal, Quebec, Canada

August 2014

A Thesis submitted to McGill University in partial fulfillment of the requirements for the degree of Doctor of Philosophy

Abstract

Different molecular, thermodynamic, and kinetic aspects of protein-ligand binding were studied in the present thesis. This was accomplished using diverse techniques such as Nuclear Magnetic Resonance (NMR), fluorescence spectroscopy, and calorimetry.

Chapter 1 introduces the basic concepts to understand the dynamics and thermodynamics of binding for systems where a ligand receives just one binding molecule.

Chapter 2 gives an up-to-date technical background on NMR experimental techniques to study dynamics and thermodynamics of protein-ligand binding. These techniques were key to the research developed in chapters 3, 4 and to a lesser extent in Chapter 5.

Chapters 3 and 4 focused on the interaction between the Fyn SH3 domain and several proline rich peptides. Chapter 3 describes the role of electrostatic interactions in the binding pathway of transient protein complexes formed by the SH3 domain and three proline-rich peptides. We showed that the electrostatic enhancement of binding for this weak (≥μM K_D), short-lived complex with lifetimes on the order of milliseconds is much less, and basal association rates are greater than those previously observed for tight (<nM K_D) long-lived systems with lifetimes on the order of minutes or longer. This suggests that electrostatics may play different roles in short-lived and long-lived protein complexes.

Chapter 4 mapped the changes in volume for the association pathway for the Fyn SH3 domain and a proline rich peptide. Via pressure we were able

to quantify changes in molar volume between the free, bound and transition states for this system. This is, to our knowledge, the first measurement of the activation volume for a protein-ligand binding reaction. The results agree with a protein-ligand binding pathway involving significant desolvation of the binding surfaces. We found that the volume of transition state is very close to that of the fully bound state. This suggests that the rearrangement of solvating water molecules and protein and ligand and conformational changes occur before the transition state.

Chapter 5 explored different NMR experimental approaches for studying the interaction between bisphophonate inhibitors and human farnesyl pyrophosphate synthase. Different isotopic protein labeling patterns were used to study this system together with a series of NMR experiments designed to exploit these specifically labeled proteins.

Résumé

Dans cette thèse nous avons étudié plusieurs aspects de biologie moléculaire, de thermodynamique, et de cinétique chimique liés aux processus d'union entre une protéine et son ligand. Afin de mener ces études, diverses techniques telles que la Résonance Magnétique Nucléaire (RMN), la spectroscopie de fluorescence et la calorimétrie ont été utilisées.

Le premier chapitre introduit les concepts de base afin de comprendre la dynamique et la thermodynamique d'union entre protéines. Un modèle simplifié dans lequel une protéine joint seulement un ligand sera utilisé.

Le deuxième chapitre donne une mise à jour des techniques RMN récentes que l'on peut utiliser pour étudier la thermodynamique et la cinétique d'union d'une protéine avec son ligand. Ces techniques sont cruciales pour développer les travaux de recherche expliqués dans les chapitres 3, 4 et d'une manière plus limitée dans le chapitre 5.

Le troisième et quatrième chapitres traitent de l'interaction entre le domaine d'union SH3 de la tyrosine kinase fyn et plusieurs peptides riches en prolines. Nous avons démontré que l'influence des forces électrostatiques dans la constante de vitesse est plus faible pour les systèmes ayant un temps de demi-vie de l'ordre de la milliseconde et

possèdent des faibles constantes d'affinités ($\geq \mu M\ K_D$) par rapport aux complexes plus stables, avec un temps de demi-vie de l'ordre d'heures ou de jours, qui possèdent constantes d'affinités plus élevées ($< nM\ K_D$). Nous avons également démontré que les vitesses d'association basales, indépendantes des forces électrostatiques, sont plus importantes dans la formation de complexes transitoires. Cela suggère que les forces électrostatiques jouent un rôle différent dans les complexes transitoires et les complexes stables.

Le quatrième chapitre cartographie les changements de volume pour l'association entre le domaine SH3 et un peptide riche en prolines. En utilisant la pression hydrostatique nous avons mesuré les volumes molaires relatifs de l'état libre, l'état de transition et du complexe final protéine-ligand uni. D'après nous, c'est la première fois que le volume d'activation pour un processus d'union entre protéines est mesuré. Les résultats sont en accord avec une libération d'eau d'hydratation des surfaces d'union entre la protéine et le peptide. Nous avons observé que le volume de l'état de transition est très proche de celui du complexe final.

Dans le cinquième chapitre différentes approches expérimentales de RMN ont été explorées afin d'étudier l'interaction entre les inhibiteurs type bisphosphonates et la protéine humaine farnesyl pyrophosphate synthase.

Différents systèmes de marquage isotopique de la protéine ont été essayés afin d’étudier cette interaction.

Acknowledgments

First and foremost I would like to thank my supervisor Dr. Anthony Mittermaier for his support and guidance during my Ph. D. studies. He took an extremely shy and confused individual at the beginning of his graduate studies, and patiently, he was able to guide me in becoming someone who is a little less shy and at least a little bit more able to do some research.

Dr. Tara Sprules was also an unconditionally kind and always opportune voice of support while I was learning (as I always will be) all the instrumental tools as an NMR spectroscopist. Thank you so much for all the patience and careful explanation of NMR experiments.

I would also like to thank all of the evaluation committee members throughout my studies: Professors Amy S. Blum, Gonzalo Cosa, Nicolas Moitessier, and Masad Dahma. Annual discussions on research were always an interesting time for learning.

I would like to thank Jean-Philippe Demers. Hardworking craziness is perhaps the best way to learn about biological NMR from someone who is an outstanding researcher.

I wish to acknowledge my friend and lab mate Pierre Karam for his always nice voice of support and his endless corridor planed jokes. Also I wish to thank all the actual and past lab members, Pat, Lee, Teresa, Jason, Eric H, Siqi, Stephane, Rob H., Justin, and Eric. They made my journey through graduate studies more pleasant.

Finally I would like to thank to the three more important people in my life. My always supportive Mother Flor Marina, my wife Andrea, who changed her professional, nice and comfortable life in Colombia to come over to Canada to follow our dreams. Thank you Andrea for bringing that little piece of joy and cuteness that is healthy growing inside you.

Table of Contents

Abstract....................i
Résumé....................iii
Acknowledgments....................vi
Table of Contents.....................viii
List of Figures....................xi
List of Tables....................xiv
Abbreviations....................xv

1. Introduction....................1
  1.1 Importance of studying protein-ligand binding....................2
  1.2 Rigid two-body binding....................4
  1.3 Binding equilibrium constants in a system exchanging between two states....................6
  1.4 Protein-ligand dynamics....................10
  1.5 Protein ligand binding limited by diffusion....................16
  1.6 Association rate constants k_{on} and transition state....................21
  1.7 Relation between diffusion coefficient and viscosity....................24
  1.8 Measuring protein-ligand binding thermodynamics....................28
    1.8.1 Isothermal Titration Calorimetry, model for 1:1 binding....................29
    1.8.2 Intrinsic tryptophan Fluorescence and protein ligand binding....................31
  1.9.Biological systems....................33
    1.9.1 Protein interaction domains....................34
    1.9.2 Proline rich motifs and polyproline II conformation....................35
    1.9.3 Fyn SH3....................36
    1.9.4 hFPPS....................38

2. Analyzing Protein-Ligand Interactions by Dynamic NMR Spectroscopy....................41
  2.1 Summary....................42
  2.2 Introduction....................43
  2.3 Materials....................51
    2.3.1 NMR samples....................51
    2.3.2 Spectral Analysis....................53
  2.4 Methods....................55
    2.4.1 Titration analysis....................55
      2.4.1.1 NMR-derived binding isotherms....................55

2.4.1.2 Line-shape analysis 58
2.4.2 Carr-Purcell-Meiboom-Gill (CPMG) experiments 61
2.4.2.1 CPMG overview 61
2.4.2.2 CPMG data analysis 65
2.4.3 Magnetization exchange spectroscopy (EXSY) 70
2.4.3.1 EXSY overview 70
2.4.3.2 EXSY data analysis 72
2.5 Notes 75
2.5.1 NMR Titrations 75
2.5.2 CPMG experiments 76
2.5.3 EXSY experiments 79

3. Electrostatic interactions in the binding pathway of a transient protein complex studied by NMR and isothermal titration calorimetry 80
3.1 Abstract 81
3.2 Introduction 82
3.3 Materials and methods 90
3.3.1 ITC 90
3.3.2 NMR 91
3.3.3 Electrostatic Enhancements 95
3.3.4 Stopped-flow binding kinetics 95
3.3.5 NMR-derived binding kinetics 98
3.4 Results and discussion 99
3.4.1 NMR titration experiments 99
3.4.2 Isothermal Titration Calorimetry 102
3.4.3 NMR kinetics experiments 104
3.4.4 Comparison of NMR and stopped-flow binding kinetics 108
3.4.5 Electrostatic enhancement of association rates 110
3.4.6 Arginine interactions in the transition state and bound state 115
3.4.7 Ionic strength dependence of dissociation rates 118
3.5 Conclusions 120
3.6 Acknowledgements. 122

4. Mapping volume changes in the binding pathway of an SH3 domain and a proline rich peptide 123
4.1 Summary. 124

4.2 Introduction. 126
4.3 Experimental. 131
4.3.1 Protein and peptide purification 131
4.3.2 Intrinsic tryptophan fluorescence experiments 131
4.3.3 Changes upon binding in molecular volume ΔV_M, thermal volume ΔV_T, and measurement of accessible solvent surfaces for the free and bound states 132
4.3.4 CPMG experiments 134
4.5 Results 136
4.5.1 Intrinsic tryptophan fluorescence experiments 136
4.5.2 Measurement of ΔV_M, ΔV_T and analysis of ΔV_I 141
4.5.3 CPMG NMR kinetic experiments 144
4.6 Conclusion 147

5. NMR experimental approaches to study binding of bisphophonates to human Farnesyl Pyrophosphate Synthase (hFPPS) 149
5.1 Overview. 150
5.2 hFPPS expression and purification 154
5.3 HSQC NMR experiments on hFPPS. 155
5.4 Further experiments on hFPPS 158
5.4.1 Lysine methylation of hFPPS. 162
5.4.2 hFPPS deuteration 166
5.4.3 . hFPPS perdeuteration and 1H-13C labeling of methyl groups on isoleucines, leucines and valines using metabolic precursors 169

6. Further research directions 174
6.1 Overview 175
6.2 Electrostatic interactions in the binding pathway of a transient protein complex studied by NMR and isothermal titration calorimetry. 175
6.3 Mapping volume changes in the binding pathway of an SH3 domain and a proline rich peptide 177
6.4 NMR experimental approaches to study binding of bisphophonates to human Farnesyl Pyrophosphate Synthase (hFPPS). 178

References 180

List of Figures

Chapter 1

Figure 1.1 Cylinder containing a semi-permeable piston m 24

Figure 1.2 Diffusion of a dissolved substance in a differential volume dx. 25

Figure 1.3 Human Fyn SH3 domain binding to peptide VSLARRPLPPLP 38

Chapter 2

Figure 2.1 Effect of ligand-binding on an NMR signal 46

Figure 2.2. Schematic representation of a 2D NMR ^{1}H–^{15}N correlation experiment 47

Figure 2.3 Titration monitored by heteronuclear correlation spectroscopy 50

Figure 2.4 Simulated binding isotherms 56

Figure 2.5 Dissociation constant from a global analysis of ^{15}N and ^{1}H chemical shift displacements 58

Figure 2.6 Schematic representation of a 15N CPMG experiment 64

Figure 2.7. Exchange rates from CPMG dispersion curves 70

Figure 2.8 Schematic representation of an EXSY pulse sequence. 72

Chapter 3

Figure 3.1 Regions of ^{15}N-^{1}H HSQC spectra of the Fyn SH3 domain titrated with RR SR and SS peptides 99

Figure 3.2 Structure of the Fyn SH3 domain in complex with a ligand identical to the RR peptide but containing Val rather than Trp at position -8, PDB 4EIK 100

Figure 3.3 Isothermal Titration Calorimetry raw thermograms and integrated heats for RR, SR and SS peptides binding to the Fyn SH3 domain at 40°C and different ionic strength. 102

Figure 3.4 Base 10 logarithms of affinity constants, KA, of the Fyn SH3 domain for RR, SR, and SS peptides plotted as a function of ionic strength. 103

Figure 3.5 NMR 15N CPMG relaxation dispersion data for the backbone amide signal of W36 collected at 500 and 800 MHz and 0M NaCl. 105

Figure 3.6 Comparison of $\Delta\omega^2$ 15N chemical shift parameters extracted from CPMG relaxation dispersion NMR experiments performed on the Fyn SH3 domain partially-saturated with the RR peptide (0M NaCl) and $\Delta\delta^2$ peak displacements from a comparison of the Fyn SH3 domain spectra free and saturated with the RR peptide (0 M NaCl). 106

Figure 3.7 Stopped-flow fluorescence data for the Fyn SH3 domain rapidly mixed with buffer and with a solution of the RR peptide. 109
Figure 3.8 Ionic strength dependence of association rates 111
Figure 3.9 Enhancements in affinities ($K_A^{SR,RR}/K_A^{SS}$) and association rates ($k_{on}^{SR,RR}/k_{on}^{SS}$) for the RR and SR peptides relative to the SS peptide, plotted as a function of f_{ion} 115

Chapter 4

Figure 4.1 Chicken Fyn SH3 domain intrinsic Trytophan fluoresence spectra 137
Figure 4.2 r vs center of spectral mass for binding between chicken fyn SH3 domain and Ac-FSLARRPLPPLP-NH_2 peptide. 138
Figure 4.3 Change in free energy of binding as a function of pressure for the system chicken fyn SH3 domain/Ac-FSLARRPLPPLP-NH_2 peptide 140
Figure 4.4 Cavity volume calculations for the free and bound states using castP. 142
Figure 4.5 Change in free energy between the bound state and the transition state as a function of pressure for the system chicken fyn SH3 domain / Ac-FSLARRPLPPLP-NH_2 peptide. 145
Figure 4.6 Plot of $|(\Delta\delta_i)_{HSQC}|$ vs $|(\Delta\omega_i)_{CPMG}|$ for every residue used to calculate kinetic parameters at every the pressures. 146
Figure 4.7. Volume change map for binding between a chicken fyn SH3 domain and Ac-FSLARRPLPPLP-NH_2 peptide 147

Chapter 5

Figure 5.1 Schematic representation of the mevalonate pathway. 151
Figure 5.2 The structure of some simple bisphophonates. 152
Figure 5.3 ^1H-^{15}N HSQC spectrum for the Apo form of hFPPS. 156
Figure 5.4 ^1H-^{15}N HSQC for 15N labeled hFPPS saturated with magnesium, the bisphophonate Zoledronate and pyrophosphate. 158
Figure 5.5 Reaction for ^{13}C reductive methylation of lysines. 164
Figure 5.6 ^1H-^{13}C HSQC spectrum of hFPPS 13C lysine methylated in the apo state...165
Figure 5.7 ^1H-^{15}N HSQC spectrum for a partially deuterated sample of hFPPS............168
Figure 5.8 ^1H-^{15}N HSQC spectrum for a partially deuterated sample of hFPPS saturated with magnesium, Zoledronate and pyrophosphate 168
Figure 5.9 ^1H-^{15}N spectrum TROSY-HSQC experiment for perdeuterated, methyl labeled hFPPS in the apo state. 171
Figure 5.10 shows a ^1H-^{13}C methyl HMQC experiment for a 300uM hFPPS in the apo state. 171

Figure 5.11 1H-13C methyl HMBC experiment of hFPPS perdeuterated and methyl labeled on ILV, saturated with magnesium, Zoledronate an pyrophospate 173

List of tables

Table 3.1. Electrostatic enhancement of protein association rates 85
Table 3.2. Thermodynamic and kinetic binding parameters for the Fyn SH3 domain 101
Table 4.1. Pressure effect on the binding between chicken fyn SH3 domain and a proline rich peptide. 139
Table 4.2. Kinetic parameters of binding between Fyn SH3 domain and a proline rich peptide at different pressures. 144

Abbreviations

‡	Transition State
A	Alanine
Å	Angstroms
Ala	Alanine
Arg	Arginine
B	Static magnetic field vector
B_0	Static magnetic field strength
C	Cysteine or carbon
CD	Circular dichroism
CPMG	Carr-Purcell-Meiboom-Gill
CSA	Chemical shift anisotropy
C-terminus	Carboxyl (COOH) moiety that defines the 3' end of a polypeptide
Cys	Cysteine
D_A	Diffusion coefficient of A
DD	Dipole-dipole
DMAPP	Dimethylallyl pyrophosphate
DNA	Deoxyribonucleic acid
DSC	Differential Scanning Calorimetry
DSS	Sodium 2,2-dimethyl-2-silapentane-5-sulfonate
E	Glutamic Acid
e. Coli	Escherichia coli
EXSY	Exchange spectroscopy
F	Phenylalanine or fluorescence
f	Force
FYN	Fyn tyrosine kinase
G	Glycine or Gibbs free energy or time-domain NMR signal
Glu	Glutamic Acid

Gly	Glycine
GPP	Geranyl pyrophosphate
H	Histidine or enthalpy or Hydrogen
hFPPS	Human farnesyl pyrophosphate synthase
HPLC	High performance liquid chromatography
HSQC	Heteronuclear single quantum coherence
HMQC	Heteronuclear multiple quantum coherence
Hz	Hertz
I	Isoleucine or Nuclear spin angular momentum quantum number or intensity or ionic strength
Ile	Isoleucine
IPP	Isopentenyl pyrophosphate
ITC	Isothermal titration calorimetry
J_L	Flux of L
K	Lysine or Kelvin
K_A	Association equilibrium constant
k_A	Exchange rate from state A to state B
k_B	Boltzmann constant or Exchange rate from state A to state B
K_D	Dissociation equilibrium constant
K_{eq}	Equilibrium constant
k_{ex}	Apparent exchange rate between states A and B
k_{on}	Association rate constant
k_{off}	Dissociation rate constant
L	Leucine or Ligand
Leu	Leucine
M	Methionine or Molar
MES	2-(4-morpholino) ethanesulfonic acid
MW	Molecular weight
NMR	Nuclear Magnetic Resonance
N_A	Avogadro's number

N-BP	Nitrogen containing bisphophonates
NOE	Nuclear overhouser effect
N-terminus	Amino (NH3) moeity that defines the 5' end of a polypeptide
P	Proline or Protein
p	Pressure
P_b	Relative population of the bound state
PDB	Protein Data Bank
P_f	Relative population of the free state
Phe	Phenylalanine
PL	Protein-ligand complex
p.p.m.	Parts per million
PRD	Proline recognition domain
Pro	Proline
Q	Glutamine
q	Heat of injection
r	Radius
R	Arginine or Gas constant or Diameter
R_1	Longitudinal Relaxation Rate
R_2	Transverse Relaxation Rate
R_2^0	Exchange-free R2 value
$R_{2,A}$	R2 of state A
$R_{2,B}$	R2 of state B
R_{ex}	Chemical exchange relaxation rate
RF	Radio Frequency
RMSD	Root mean square deviation
RNA	Ribonucleic acid
RSDM	Reduced spectral density mapping
S	Serine or entropy or surface area
S_2	Model-free generalised order parameters
SH3	Src Homology 3

T	Threonine or Temperature or Tesla
T_1	Longitudinal Relaxation Time
T_2	Transverse Relaxation Time
Thr	Threonine
Tm	Unfolding midpoint
TROSY	Transverse relaxation optimized spectroscopy
Trp	Tryptophan
Tyr	Tyrosine
μ	Viscosity
V	Valine or volume or potential energy
Val	Valine
W	Tryptophan
Y	Tyrosine
γ	Magnetogyric ratio
ν	Central of spectral mass
σ	Experimental uncertainty
δ	Chemical shift
$\Delta\sigma$	Chemical shift anisotropy
$\Delta\delta$	Chemical shift perturbations
$\Delta\omega$	Difference in resonance frequency between two states
τ_{cp}	Delay between 180° pulses in a CPMG pulse train
υ_{CPMG}	CPMG pulse train frequency
φ	Hydrophobic amino acid
χ^2	Chi-squared function

1. Introduction

1.1. Importance of studying protein-ligand binding

Many biological processes involve binding between two or more biomolecules. In most of the cases at least one of the binding partners is a protein. In order to understand biological phenomena driven by protein-ligand binding it is important to identify the binding molecules that play a role in the formation of the bound complex. At the same time, it is also crucial to elucidate the mechanisms and the main driving forces that control the association process. Studying protein binding is an interesting and intense field of work in molecular biology. The main subject in the present document will be to describe spectroscopic and calorimetric techniques to study dynamics (or kinetics) and thermodynamics of protein-ligand association processes. This will be further illustrated using different biological systems in chapters 3, 4 and 5.

Studying protein-ligand binding is fundamental to understanding life. Particular association processes can shed light upon a number of fundamental phenomena in molecular biology. Understanding protein-ligand binding can be useful in order to appraise exquisite mechanisms of enzymatic function (1). It can also provide underpinning information about signaling processes inside the cell (2). Beautiful and sometimes intricate cooperative binding systems can be unveiled through protein-ligand binding analysis (3). Studying protein ligand dynamics and thermodynamics together with binding computational models have been exquisitely used in drug design (4).

Information on binding is also vital to describe self organization of cellular structures (5). Finally, protein-ligand studies have certainly helped to recognize the driving forces and key steps in the formation of relevant multi-component molecular complexes in biology(6).

In the present work we will consider a system comprising a protein and a binding species. The latter will be called the ligand. The nature of the ligand can be as wide-ranging as but not limited to a small organic molecule, an ionized metal molecule, a small peptide or even a bigger molecule such another protein.

In many cases the formation of the protein-ligand bound complex can be explained using a simple general model that provides useful information about the binding pathway. The insights about the binding pathway can be used to identify the driving forces behind the association process and how they act. This information helps to define the limits in the energy pathway of binding. This binding energy pathway or stability landscape drives the formation of the final bound state(7).

1.2. Rigid two-body binding

Binding between two rigid bodies is perhaps the simplest model that can be used to explain protein-ligand binding. Despite of its apparent simplicity, this model is very useful and can be adapted to explain elementary protein-ligand binding processes in nature(8).

Consider binding between a protein (P) and a ligand (L) that will form a final bound complex PL. This process can be modeled using the following pseudo chemical reaction equation:

$$P + L \rightleftharpoons PL \tag{1.1}$$

We can write an expression for the association equilibrium constant (K_A) for this process as:

$$K_A = \frac{[PL]_{eq}}{[P]_{eq}\,[L]_{eq}} \tag{1.2}$$

Where $[P]_{eq}$, $[L]_{eq}$ and $[PL]_{eq}$ are the concentrations at equilibrium for the protein, ligand and bound complex respectively.

To have an idea about how tightly a ligand binds to a protein, we can make explicit the units chosen to express the concentration of the biding species.

i.e., a value of K_A=10^6 M^{-1} means that at sufficiently high concentrations the bound state PL is the predominant species at thermodynamic equilibrium. This is equivalent to say that the bound state is more populated at equilibrium, or equally means that the equilibrium is displaced towards the formation of the species PL. Values of K_A are usually mathematically more convenient to operate with and they can be used to quantify the change in free energy for the association process (ΔG_A) using the expression(9):

$$\Delta G_A = -RTLn(C^o K_A) \tag{1.3}$$

Where R is the universal gas constant, T is the absolute temperature at which the equilibrium binding constant is measured and C^o is the concentration of the standard state. In the present text the concentration of the standard state will be fixed to 1 mol l^{-1}. We can also measure how tightly a protein binds to its ligand using the equilibrium dissociation constant, K_D:

$$K_D = \frac{1}{K_A} = \frac{[P]_{eq}\,[L]_{eq}}{[PL]_{eq}} \tag{1.4}$$

The numerical value of K_D can be understood intuitively, since it tells what would be the concentration of free unbound ligand in equilibrium, $[L]_{eq}$, when the concentrations of the free and bound states are the same $\left([PL]_{eq} = [P]_{eq}\right)$. i.e., K_D= 1 x 10^{-6} (M) = 1 (μM) means that given a binding equilibrium where the protein is half saturated (same concentrations of PL and L, or equivalently, same relative populations of states PL and L) we will have a concentration of free ligand $[L]_{eq}$ = 1 x 10^{-6} mol l^{-1}.

The relative populations of the bound (p_b) and free (p_f) states of the protein are given by:

$$p_b = \frac{[PL]_{eq}}{[PL]_{eq} + [P]_{eq}} \ ; \ p_f = \frac{[P]_{eq}}{[PL]_{eq} + [P]_{eq}} \tag{1.5}$$

From equation (1.6) we can shown that $p_f = (1 - p_b)$. Both populations, p_b and p_f have a range of [0,1] . $p_b = 0$ or equivalent to $p_f = 1$ meaning fully free unbound protein; and $p_b = 1$ or equivalent to $p_f = 0$ meaning fully saturated or completely bound protein.

1.3. Binding equilibrium constants in a system exchanging between two states

Measuring protein ligand binding equilibrium constants is possible through the use of different experimental tools. In most of the cases a mathematical model must be defined first, and then subsequent data analysis is required to extract K_A. Fortunately, for most of all the experimental techniques the model shares the same mathematical structure.

Suppose we have an experimentally measured variable called δ that is a linear function of the relative populations at equilibrium of the protein in the free and bound states $\delta(p_b, p_f)$.

This variable can be expressed for any values of p_b and p_f as:

$$\delta(p_b, p_f) = p_b\delta_{sat} + p_f\delta_{free} = p_b\delta_{sat} + (1 - p_b)\delta_{free} \tag{1.6}$$

Where δ_{free} and δ_{sat} are the values that δ takes when p_f and $p_b$are respectively equal to 1. Rearranging equation (1.7) we obtain:

$$\delta(p_b, p_f) = p_b(\delta_{sat} - \delta_{free}) + \delta_{free} = \delta_{free} - p_b \Delta\delta_{max} \tag{1.7}$$

Where $\Delta\delta_{max} = (\delta_{sat} - \delta_{free})$. From (1.8) we can derive a couple of useful relationships:

$$p_b = \frac{\delta - \delta_{free}}{\delta_{sat} - \delta_{free}} = \frac{\delta - \delta_{free}}{\Delta\delta_{max}} \tag{1.8}$$

and:

$$p_f = \frac{\delta - \delta_{sat}}{\delta_{free} - \delta_{sat}} = \frac{\delta_{sat} - \delta}{\Delta\delta_{max}} \tag{1.9}$$

We want to obtain an expression for δ as a function of experimentally measurable variables such as the initial (total) concentrations of the protein $[P]_{total}$, and the ligand $[L]_{total.}$ In order to extract the association equilibrium constant, this function must have K_A as an experimentally extractable parameter that can be fitted or adapted to the model.

For this reason, we rewrite the binding equilibrium equation (1.3) as:

$$K_A = \frac{[PL]_{eq}}{([P]_{total} - [PL]_{eq})([L]_{total} - [PL]_{eq})} \tag{1.10}$$

Because the total mass of the protein must be conserved, we can write: $[P]_{total} = [PL]_{eq} + [P]_{eq}$. Replacing this in equation (1.6) we obtain:

$$[PL]_{eq} = p_b[P]_{total} \tag{1.11}$$

Replacing (1.12) into (1.11) gives:

$$K_A = \frac{p_b/[P]_{total}}{(1-p_b)(R-p_b)} \tag{1.12}$$

Where R is the ratio $[L]_{total}/[P]_{total}$.

Expanding and rearranging equation (1.12) gives:

$$\frac{p_b}{K_A[P]_{total}} = (1-p_b)(R-p_b) = R-(R+1)p_b + p_b^2 \tag{1.13}$$

Which can be expressed as a quadratic expression of p_b :

$$p_b^2 - \left(1 + R + \frac{1}{K_A[P]_{total}}\right)p_b + R = 0 \tag{1.14}$$

The real root of this equation is:

$$p_b = \frac{b - \sqrt{b^2 - 4R}}{2} \tag{1.15}$$

Where $b = 1 + R + \frac{1}{K_A[P]_{total}}$. Replacing the value of p_b from equation (1.8) in equation (1.15) gives (10):

$$\delta = \delta_{free} - \left(\frac{\Delta\delta_{max}}{2}\right)\left(b - \sqrt{b^2 - 4R}\right) \tag{1.16}$$

Equation (1.16) represents the variable δ as a function of $[L]_{total}$ and $[P]_{total}$ as we wanted. It also has the affinity binding constant K_A as a fitting parameter. This equation is a basic tool for the analysis of any titration curve in a system exchanging between two states described in equation (1.1).

δ can be measured using several physical techniques. It is desirable that the selected property to be measured changes linearly with the extent of the association process. This will make easier the fitting procedure that is used to measure the affinity binding constant K_A.

δ potentially can be intrinsic fluorescence intensity of the protein or the ligand. For some other systems δ can be the frequency associated with a magnetic resonance signal coming from nuclear spins present in the protein or the ligand. In all the previous scenarios our function δ will provide a tool to quantify the association equilibrium constant K_A.

The final goal of studying protein ligand binding thermodynamics is to understand how the binding landscape is modulated by changes in free energy, entropy and enthalpy upon binding. This approach can be used to identify the main driving forces behind the association process and in some cases can provide underpinning molecular information relative to binding. However, studying thermodynamics of binding alone will provide just a "static picture" of the relative stabilities between the free and bound states. In this way we will obtain valuable quantitative information on the change in thermodynamic variables upon binding. However, any information about intermediate states, or transition states that exist between the free species and the final bound complex are therefore invisible. Any stability or molecular changes in those intermediate states are essentially unknown. In theory, an infinite number of energy pathways can similarly explain the changes in thermodynamic variables between the free unassociated species and the final bound protein-ligand complex(11).

If we want to gain more information about the intermediate states during protein-ligand binding it is essential to measure dynamics (or kinetics) of the association process. Some experimental techniques, such as Nuclear Magnetic Resonance (30) can provide detailed atomic resolution information on intermediate states during protein-ligand association(12). Without the use of NMR some of these intermediate states would be virtually undetectable or "invisible".

Following the analogy that describes protein-ligand binding thermodynamics as a tool that provides a "static picture" of the relative stabilities of the free and bound states, we can take the analogy one step further saying that the study of protein-ligand binding kinetics will deliver an extra and helpful "snapshot" of the relative stability of any intermediate binding state.

1.4. Protein-ligand dynamics

There is an additional and perhaps complementary view to understand the binding equilibrium reaction described in equation (1.1). This approach implies that any binding equilibrium is dynamic. The measured macroscopic value of any equilibrium constant is merely a consequence of the principle of detailed balance(13). This principle states that for a complex reaction in equilibrium the speed of every forward process is equal to the speed of the reverse process. This is valid for every single elementary process in the binding mechanism. The equilibrium concentration values of the binding species can be found after counting the total number of P and L particles that are associating at the "on" rate to form the bound complex minus the total number of the PL species disaggregating at the "off" rate into the free (P and L) species. This can be illustrated by writing the following equation that describes a bimolecular reversible binding reaction:

$$P + L \underset{k_{off}}{\overset{k_{on}}{\rightleftharpoons}} PL \tag{1.17}$$

Where k_{on} the "on" or association is rate constant and k_{off} is the dissociation or "off" rate constant. Equation (1.18) is a condensed expression of the following differential equations:

$$-\frac{d[P]}{dt} = k_{on}[P][L] - k_{off}[PL] \tag{1.18}$$

$$-\frac{d[L]}{dt} = k_{on}[P][L] - k_{off}[PL] \tag{1.19}$$

$$-\frac{d[PL]}{dt} = k_{off}[PL] - k_{on}[P][L] \tag{1.20}$$

In this particular case $[P], [L]$, and $[PL]$ are the protein, ligand and bound complex concentrations at any time t. These differential equations define binding dynamics (kinetics) for a bimolecular system following a second order binding reaction. $[P], [L]$, and $[PL]$ are not limited to equilibrium values anymore. In fact, at equilibrium, all the time derivatives of the concentrations are zero, and equations (1.19), (1.20) and (1.21) are equivalent to equation (1.3).

From this is clear that:

$$K_A = \frac{1}{K_D} = \frac{[PL]_{eq}}{[P]_{eq}\,[L]_{eq}} = \frac{k_{on}}{k_{off}} \tag{1.21}$$

Equations (1.19) through (1.21) describe a simple one step reversible bimolecular binding reaction formerly introduced in equation (1.1).

If we define the following boundary conditions: At $t = 0$, $[P] = [P]_0$, $[L] = [L]_0$ and $[PL] = [PL]_0$; At $t = t$, $[P] = [P]_0 - [x]$, $[L] = [L]_0 - [x]$ and $[PL] = [PL]_0 + [x]$, where $[x]$ is either the increase in the concentration of the species PL at an arbitrary time t compared to $[PL]_0$, or the decrease in the concentration of the species P and L at time t compared to the respectively initial values $[P]_0$ and $[L]_0$.

We can now write the following differential equation:

$$\frac{d[x]}{dt} = k_{on}([P]_0 - [x])([L]_0 - [x]) - k_{off}([PL]_0 + [x]) \tag{1.22}$$

After expanding we obtain:

$$\frac{d[x]}{dt} = k_{on}[P]_0[L]_0 - k_{off}[PL]_0 - \{k_{on}([P]_0 + [L]_0) + k_{off}\}[x] + k_{on}[x]^2 \tag{1.23}$$

If we define: $\gamma = k_{on}[P]_0[L]_0 - k_{off}[PL]_0$; $\beta = -\{k_{on}([P]_0 + [L]_0) + k_{off}\}$; $\alpha = k_{on}$. We can write equation (1.24) as:

$$\frac{d[x]}{dt} = \gamma + \beta[x] + \alpha[x]^2 \tag{1.24}$$

A solution for this differential equation is:

$$Ln\left(\frac{[x] + \left(\beta - \sqrt[2]{q}\right)/2\gamma}{[x] + \left(\beta + \sqrt[2]{q}\right)/2\gamma}\right) = \sqrt[2]{q}\; t + \theta \tag{1.25}$$

Where: $q = \beta^2 - 4\alpha\gamma$; $\theta = Ln\left(\left(\beta - \sqrt[2]{q}\right)/\left(\left(\beta + \sqrt[2]{q}\right)\right)\right)$.

We can also find a more simple and experimental useful solution defining the following boundary conditions: $t = 0$, $[P]_{total} = [L]_{total}$, $[PL] = 0$;

Equation (1.26) can be written now as (14):

$$Ln\left(\frac{2[P] + \left(\frac{k_{off}}{k_{on}}\right)(1+\zeta)}{2[P] + \left(\frac{k_{off}}{k_{on}}\right)(1-\zeta)}\right) = k_{off}\zeta t + C \tag{1.26}$$

Where $\zeta = \sqrt[2]{1 + 4[P]_{total}k_{on}/k_{off}}$ and $C = Ln\left(\frac{2[P]_{total} + \left(\frac{k_{off}}{k_{on}}\right)(1+\zeta)}{2[P]_{total} + \left(\frac{k_{off}}{k_{on}}\right)(1-\zeta)}\right)$, is a constant.

Equations (1.26) or (1.27) are some of the fitting tools that we can use to measure the dissociation (k_{off}) rate constant and the dissociation rate constant (k_{off}) for a bimolecular reversible binding system. They will also provide a value for the equilibrium constant $K_A = \frac{k_{on}}{k_{off}}$. The only requirement to do so, is to select a physical measurable property that can be a linear function of the values of $[P]$, $[L]$ or $[PL]$ between the free and the equilibrium state.

We will use again the function δ to track the association process, but in this case δ will be also a function of time. We need to define a time dependent function such as:

$$\delta(t) = p_{free}(t)\delta_{free} + p_{eq}(t)\delta_{sat} \tag{1.27}$$

Where: $p_{free}=\frac{[P](t)}{[P]_{total}}$, $p_{eq} = \frac{[P]_{eq}}{[P]_{total}} = \frac{[P]_{total}-[P](t)}{[P]_{total}}$, δ_{free} and δ_{sat} are the values that $\delta(t)$ takes respectively at the free unbound state and at the fully saturated bound system.

Under these conditions we can write equation (1.28) as:

$$\delta(t) = \frac{[P](t)}{[P]_{total}}\delta_{free} + \frac{[P]_{total} - [P](t)}{[P]_{total}}\delta_{sat} \tag{1.28}$$

$$or$$

$$[P](t) = \frac{\delta(t) - \delta_{bound}}{\delta_{free} - \delta_{bound}}[P]_{total} \tag{1.29}$$

Equation (1.30) makes $[P]$ a variable that only depends of time. In some cases $\delta(t)$ can be fluorescence, optical absorbance, circular dichroism, infrared, electron paramagnetic resonance or light scattering, measured as a function of time during protein-ligand binding. In order to be experimentally useful, $\delta(t)$ must be well defined and measurable at the free unbound state and at the thermodynamic equilibrium.

Measuring binding kinetics using the previous approach requires the rapid mixing of free protein and free ligand. Then, during the association time the formation of the bound complex is followed or measured using an appropriate physical variable $\delta(t)$. The system obviously starts far from thermodynamic equilibrium. Under these circumstances binding kinetics becomes a study case of mass transport phenomena coupled to a collision-docking event. This means that the protein-ligand binding process can be separated into two fundamental steps: First, diffusion of protein and ligand in a concentration gradient towards their binding partners(15); and second, a collision-docking event that requires either the right orientation and the proper kinetic energy in order to make this final step a binding event(16).

Studying protein-ligand binding dynamics through mixing techniques requires that the time of mixing of the reagents must be faster than the time that the association process takes place, otherwise the measure of protein ligand binding kinetics is not feasible. There is a maximum upper limit for the binding association rate(17). This theoretical limit considers a diffusion-controlled reaction. In this theoretical binding scheme every single collision between the protein and ligand will form a final bound complex. This upper limit describing binding at the diffusion limit can be mathematically calculated after defining certain conditions in the system(15).

1.5. Protein ligand binding limited by diffusion

We will consider again the reversible bimolecular binding reaction $P + L \rightleftharpoons PL$. It will be assumed that protein (P) and ligand (L) are spherical uncharged molecules without any potential energy of interaction between them. We want to calculate an expression for the rate at which P and L collide. Under these conditions, we will obtain an expression for the bimolecular rate constant for a system binding at the diffusion limit. In a first instance we can assume that P is an immobile protein molecule, and that molecules of L diffuse into P colliding with it to form the bound complex PL(14). Using first Fick´s law we can write an expression to calculate the rate of flow of L molecules per unit area in the space (Flux, J_L) as:

$$J_L = -D_L \nabla C_L \tag{1.30}$$

Where D_L is the diffusion coefficient for the ligand in the solution and C_L is the ligand concentration in molecules per volume unit.

It will be assumed that the concentration of L only changes with the distance (r) measured from the center of mass of every protein. For this reason we can set the following conditions using spherical coordinates: $\frac{\partial C_L}{\partial \Theta} = 0$ and $\frac{\partial C_L}{\partial \phi} = 0$.

Now Fick's equation becomes:

$$J_L = -D_L \frac{\partial C_L}{\partial \mathrm{r}} \tag{1.31}$$

We can calculate the number of molecules of L flowing inwards a spherical shell of radius r per unit area ($\mathbb{J}_L$) as:

$$\mathbb{J}_L = -4\pi r^2 J_L = 4\pi r^2 D_L \frac{\partial C_L}{\partial \mathrm{r}} \tag{1.32}$$

Under steady state conditions the concentration gradient of L is constant in time. This will make $\mathbb{J}_L$ a constant parameter independent of r. For these reasons we can now rewrite equation (1.33) using absolute differentials for the radial distance and ligand concentration as:

$$\mathbb{J}_L r^{-2} dr = 4\pi D_L dC_L \tag{1.33}$$

Before solving the previous differential equation we will define r_0 as the minimum distance between the molecular centers of the protein and the ligand. The value of r_0 is the distance of the molecular centers when protein and ligand collide. In our model, a collision between P and L forms, by definition, the final bound complex PL.

The origin of the spherical coordinate system $(r = 0)$ is at the center of mass of every single static protein (P). Equation (1.34) can now be integrated for a particular protein molecule using the following boundary conditions: at $r = r_0$, $C_L = 0$ (after binding there is an instantaneous formation of the final bound complex) and at $r = \infty$, $C_L = [L]$ (far from the protein surface the ligand concentration is constant and is equal to the ligand's concentration in the bulk solution $[L]$).

Setting these limits gives:

$$\mathbb{J}_L \int_{r_0}^{\infty} r^{-2} dr = 4\pi D_L \int_0^{[L]} dC_L \tag{1.34}$$

Integration provides:

$$\mathbb{J}_L = 4\pi D_L r_0 [L] \tag{1.35}$$

Equation (1.36) calculates the number of collisions of the ligand with the protein per unit time considering that the all the protein molecules are motionless. If we want to account also for the diffusion of the protein into the ligand, we obtain the following expression(15):

$$\mathbb{J}_{PL} = 4\pi(D_P + D_L) r_0 [P][L] \tag{1.36}$$

Where ($\mathbb{J}_{PL}$) accounts for the total number of collisions per unit time between the protein and the ligand. Protein and ligand are at bulk concentrations $[P]$ and $[L]$ respectively.

Equation (1.37) can also be written as:

$$\mathbb{J}_{PL} = 4\pi(D_P + D_L) r_0 [P][L] = k'[P][L] \tag{1.37}$$

Where $k' = 4\pi(D_P + D_L)r_0$. Using Avogadro´s number (N_A), we can use the value of k' to finally calculate the bimolecular association rate constant for protein-ligand binding, k_{on}, as:

$$k_{on} = N_A k' = N_A 4\pi(D_P + D_L)r_0 \tag{1.38}$$

Expression (1.38) sets a theoretical limit for the maximum speed of the association rate under the conditions previously defined. There are systems that show even higher association binding rates than those derived for a diffusion-controlled binding reaction. This is the case for a protein and ligand binding under the effect of an attractive electrostatic potential. An example of such a system will be illustrated in chapter 3.

Systems binding close to diffusion limit are considered fast binders. Measurement of fast binding kinetics in protein-ligand binding is a challenging experimental task. In most of the cases, mixing methods used to measure dynamics are not suitable to measure fast binding kinetics(14). In these cases, other techniques, such as relaxation methods, are recommended. The principle behind relaxation techniques is to start with a protein-ligand system at equilibrium. A pulse signal (temperature, pressure, radiation) is suddenly applied displacing the system towards a new equilibrium. The speed at which the pulse is applied must be much faster that the time that takes to the system to move or "relax" to the new equilibrium. The time that the system takes to arrive at the new equilibrium is measured (relaxation time). This is done following over the time a physical variable that measures the change in concentration of the binding species through the transition between equilibria. The interesting part of the relaxation methods is that the shape of the curve that tracks the changes on concentration also encodes the values of the on and off rates of the system.

In our particular case, when the association process is in the millisecond to microsecond time scale, certain NMR relaxation dispersion techniques can be used to measure protein binding kinetics. We will have a look to these and other techniques in chapter 2.

At this point we have considered that every single collision between the protein and ligand leads to the formation of the final bound complex (PL). This is not the general rule and it is only true in a very few exceptional cases in biological systems(18). A more realistic picture to describe a true collision between protein and ligand can be illustrated in the following paragraphs.

We can have two types of collisions in bimolecular protein ligand binding. In one of them protein and ligand collide to form an unproductive protein-ligand encounter complex. In this case, after the collision, the protein and ligand dissociate. In a second type of protein-ligand encounter pair, protein and ligand have the right geometrical orientation and favorable kinetic energy. This will make this protein-ligand collision a productive encounter complex. A productive encounter complex will have the highest probability to evolve towards the formation of the final bound state. This type of favorable binding collisions or productive complexes are sometimes indistinctively named as the "encounter complex"(19), the "encounter pair"(20), the "activated complex"(21) or the "transition state"(22). We will use the term transition state to describe this type of productive collisions in the remaining part of this document.

1.6. Association rate constants k_{on} and transition state

As explained previously, protein ligand association process can be studied as a diffusion step coupled to a docking event. If the docking event is faster than the diffusion step, k_{on} is a direct measure of the number of productive collisions between ligand and protein. The binding process in this case is said to be diffusion controlled(16).

If the formation of the stereo-specific complex is slower than the diffusion rate, the association process is governed by this particular "activated" step and the kinetics of binding is said to be under activation control(18). How do we know if a particular binding process is diffusion controlled or otherwise an activated one? What is the meaning of k_{on} in both binding processes?

In order to answer the second question we will use an approach where chemical kinetics will be considered as a valid approximation to describe kinetics of protein ligand biding. We can start by looking again to equation (1.22): $K_A = \frac{k_{on}}{k_{off}}$. This expression sets a bridge between dynamics and thermodynamics of bimolecular reversible binding processes. Taking the temperature derivative of the natural logarithm on both sides of equation (1.22) gives:

$$\frac{d(Ln(K_A))}{dT} = \frac{d(Ln(k_{on}))}{dT} - \frac{d(Ln(k_{off}))}{dT} \tag{1.39}$$

Left-hand side of equation (1.40) can be expressed using Van't Hoff's equation:

$$\frac{d(Ln(K_A))}{dT} = \frac{\Delta H_A}{k_B T^2} \tag{1.40}$$

We can now rewrite equation (1.40) as:

$$\frac{\Delta H_A}{k_B T^2} = \frac{d(Ln(k_{on}))}{dT} - \frac{d(Ln(k_{off}))}{dT} \tag{1.41}$$

Van't Hoff was the first person to hint that both terms in the right-hand term of equation (1.41) could be expressed in the form (18,23):

$$\frac{d(Ln(k_i))}{dT} = \frac{\varepsilon}{k_B T^2} + \alpha \tag{1.42}$$

However, it was Svante Arrhenius who proposed for the first time a molecular model to explain association and dissociation rate constants. He suggested that certain reactant molecules (in our case P and L binding species) must be in an "activated state" that lead them to form the final product (final bound state in our case). These "active" molecules must be also in equilibrium with the rest of the reactant molecules and the rate constant must be proportional to the difference in energy between the active to normal reactant molecules(24).

If we apply Van't Hoff's equation to the equilibrium described by Arrhenius i.e., the equilibrium between active and regular reactant molecules, we obtain:

$$\frac{d(Ln(k_{on}))}{dT} = \frac{\Delta H_A^{\ddagger}}{k_B T^2} \qquad (1.43)$$

Where $\Delta H^{\ddagger}$ denotes the change in enthalpy between the active molecules and the normal reactant molecules. $\Delta H_A^{\ddagger}$ is in this way defined as the activation energy for the reaction process. In our case $\Delta H_A^{\ddagger}$ is the activation energy for the protein-ligand association process.

We can finally write a more familiar equation for k_{on} after integrating equation (1.44):

$$k_{on} = Ae^{-\frac{\Delta H_A^{\ddagger}}{k_B T}} \qquad (1.44)$$

Where constant A is an integration constant.

In chapter 3 it will be illustrated how ionic strength can modulate "on" rates in protein-ligand binding driven by electrostatic interactions. The relationship between electrostatics and association rate constants can provide insights about the molecular structure of the transition state. This will be illustrated in a protein-ligand system that binds under diffusion control. Chapter 4 will show the effect of pressure in the association rate constant for a bimolecular reversible binding system. Analysis of k_{on} as a function of pressure provided information about the relative change in volume of the transition state. This value can be correlated to changes in solvation of the system through binding.

The additional question remaining to be answered consists in finding a way to identify when a bimolecular reversible binding process is controlled by diffusion.

1.7. Relation between diffusion coefficient and viscosity

Imagine a sealed cylindrical tube with unitary transverse area containing a semi-permeable movable piston m. The cylinder is initially filled with two diluted solutions A and B containing the same solute at different concentrations. The solutions are separated by the piston and only the molecules of the solute can freely go through m as illustrated in Figure 1.1

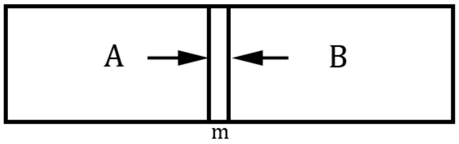

Figure 1.1 Cylinder containing a semi-permeable piston m.

Concentration of A is higher than the concentration of B. Under these conditions a force directed towards the left ($\vec{f_l}$) must be applied at m to keep the piston fixed. The magnitude of $\vec{f_l}$ must be equal to the difference of osmotic pressures times the transverse area. For sake of simplicity the transversal surface will have an area of value 1 for a given arbitrary area units. If $\vec{f_l}$ is removed, the piston will displace towards the right to achieve a final equilibrium. At equilibrium, the solute concentration at both sides of m must the same. Therefore, diffusion driven by osmotic pressure will match solute concentration at both sides of m. This experiment shows that osmotic pressure can be seen as the driving force in diffusion processes(25).

Imagine now that diffusion is taking place inside the cylinder with a net displacement of the dissolved substance in the direction x of the axis of the cylinder (Figure 1.2). We want to calculate the osmotic forces that will drive the diffusion of the dissolved substance between the planes l and l'separated by a differential distance dx.

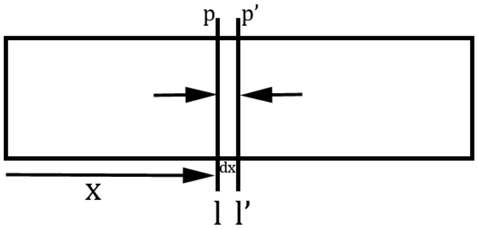

Figure 1.2. Diffusion of a dissolved substance in a differential volume dx.

Osmotic pressure force p is applied towards the right in plane l and the force p' is applied in the opposite direction in l'. The resultant osmotic pressure force applied over the differential volume segment dx is: $p - p'$. If we want to calculate the volumetric osmotic pressure (K), i.e. the osmotic pressure force that acts in the dissolved substance contained between l and l' per unit volume, we obtain:

$$K = \frac{p - p'}{dx} = -\frac{p' - p}{dx} = \frac{dp}{dx} \tag{1.45}$$

Any diluted solute is known to exert an osmotic pressure (p) over the solvent that follows Van't Hoff's equation(26):

$$p = C_i RT \tag{1.46}$$

Where C_i the molar concentration of the dissolved particle, R is is the gas constant and T is the absolute temperature of the system. Because the diffusion process is proceeding on the x direction is obvious that the concentration of the dissolved particle is a function of x. From equation (1.16) and (1.47) we can write:

$$K = -RT\frac{dC_i}{dx} \tag{1.47}$$

Now we need to calculate the kinetic force κ necessary to move a particle that is diffusing at a speed v_∞ through the planes l and l'. Calculation of κ involves the solution of differential equations (Navier-Stokes equations) that cannot be integrated for a general case. However, we can define certain boundary conditions close to experimental circumstances that will make Navier-Stokes equation soluble. The boundary conditions assume a spherical diffusing particle with a much bigger diameter than the solvent particles. Also, the speed at which the sphere moves through the solution, v_∞, must be very slow i.e. "Stokes flow". This means that the diffusing particle must move at a speed slow enough to cause a laminar flow (low Reynolds number condition) between the moving sphere and the surrounding solvent. Under these conditions we can calculate the kinetic force κ to move at a speed v_∞ one sphere of diameter R as(27):

$$\kappa = 6\pi\mu R v_\infty \tag{1.48}$$

Where μ is the solution viscosity. in equation (1.49) κ is the force to move just one molecule of the diffusing particle. We want to calculate the total force per unit volume (K) to move all the particles in the differential volume dx between the planes l and l'. We can now write:

$$K = \kappa C_i N_A = 6\pi\mu R v_\infty C_i N_A = -RT\frac{dC_i}{dx}$$

or (1.49)

$$v_\infty C_i = -\frac{RT}{6\pi\mu R N_A}\frac{dC_i}{dx}$$

Where N_A is Avogadro's number. The left hand expression of equation (1.50) is just the number of molecules of the diffusing substance that are flowing through the cylinder cross section per unit time. This is equivalent to the flux of the diffusing species J_i. Now equation (1.50) can be written as:

$$J_i = -\frac{RT}{6\pi\mu RN_A}\frac{dC_i}{dx} \tag{1.50}$$

Applying Fick's law for one-dimensional diffusion gives:

$$D_i = \frac{RT}{6\pi\mu RN_A} \tag{1.51}$$

We have previously defined the association rate constant for a reversible bimolecular binding reaction under diffusion control as $k_{on} = N_A k' = N_A 4\pi(D_P + D_L)r_0$. From equation (1.52) we have found that the diffusion coefficient D_i is a function of $\frac{1}{\mu}$. From these results is clear that if a binding reaction is diffusion limited, an increase in the viscosity of the system must be correlated with a proportional decrease in the association rate constant k_{on}.

1.8. Measuring protein-ligand binding thermodynamics

In this section a couple of experimental techniques used to measure protein-ligand binding stability will be described. Isothermal Titration Calorimetry (ITC) in chapter 3, and Intrinsic Tryptophan fluorescence in chapter 4 are used to measure binding thermodynamics. The main objective here is to explain the basics of these techniques and how they are used to quantify changes in thermodynamic variables for the association process.

1.8.1. Isothermal Titration Calorimetry, model for 1:1 binding

Isothermal Titration Calorimetry (ITC) is a method used to gain thermodynamic information of chemical reactions or binding processes(28). We will describe the use of this technique to measure protein-ligand binding thermodynamics. A typical ITC apparatus consists of a small reaction cell. In the reaction cell one of the unbound binding partners is initially confined. The free binding counterpart is loaded in a syringe. During the experiment the sample in the syringe is injected stepwise into the reaction cell.

For sake of simplicity assume that free unbound protein is initially loaded in the reaction cell and the free ligand is loaded in the syringe. During the titration, the ligand is isothermically injected and mixed in n steps into the reaction cell. After every injection, the reaction cell achieves eventually a new thermodynamic equilibrium at constant temperature. Before the ith injection, the reaction cell will contain an equilibrium solution with a total ligand to protein concentration ratio $\frac{[L]_{0,i}}{[P]_{0,i}}$. Where $[L]_{0,i}$ and $[P]_{0,i}$ are respectively the total ligand and protein concentration. Through stepwise injections of the ligand into the reaction cell, different concentrations ratios $\frac{[L]_{0,i}}{[P]_{0,i}}$ are obtained, and therefore different populations of the final bound state are sampled. The experiment is usually designed to start with injections that will provide solutions at equilibrium where the bound state (PL) is more populated, and the titration will likely finish with injections where the equilibrium solution in the cell is almost completely displaced towards the unligated state (P+L). The instrumental setup in a calorimeter measures the power required to maintain the reaction cell at the desired experimental temperature. This power is compared with the power dissipated as heat in a reference cell that is also kept at the same experimental temperature. The difference between these powers, also called differential power is followed and recorded during the time and it is used to measure the amount of heat q_i released or absorbed after every single ligand injection. By doing so, the experiment provides a titration curve where values of q_i are plotted as a function of the ligand to protein concentration ratio.

If the amount of heat released at each injection is only due to protein ligand binding, the value of q_i in the ith injection will be proportional to the net formation of the final PL complex in the reaction cell volume V_0. At each injection, ITC apparati are usually designed to displace an equal volume v_i from the reaction cell. Under these conditions we can calculate the total concentration of the protein $[P]_{0,i}$ and the ligand $[L]_{0,i}$ before the ith injection of the ligand as:

$$[L]_{0,i} = [L]_0\left(1 - d^i\right) \tag{1.52}$$

$$[P]_{0,i} = [P]_0\left(d^i\right) \tag{1.53}$$

Where $d = 1 - \left(\frac{v_i}{V_0}\right)$ is the dilution factor, $[L]_0$ is the ligand concentration in the syringe and $[P]_0$ is the initial protein concentration in the reaction cell. For every equilibrium achieved after the ith injection we can write:

$$\frac{[PL]_i}{\left([P]_{0,i} - [PL]_i\right)\left([L]_{0,i} - [PL]_i\right)} = K_A \tag{1.54}$$

Expressions (1.47), (1.48) and (1.49) can be used to calculate the number of moles of bound complex formed Δn_i after the ith injection as:

$$\Delta n_i = V_0[PL]_i - (V_0 - v)[PL]_{i-1} = V_0([PL]_i - d[PL]_{i-1}) \tag{1.55}$$

We finally can write an expression for the heat q_i associated with the ith injection as:

$$q_i = \Delta n_i \Delta H_A \tag{1.56}$$

Where ΔH_A is the enthalpy change for the association process. In this model we dismiss the heat of dilution of the ligand. Expressions (1.47) through (1.51) can be used to fit K_A and ΔH_A. An additional thermodynamic binding parameter, the entropy change of binding, ΔS_A, can be calculated since $\Delta S_\mathrm{A} = RLn(K_A) - \frac{\Delta H_A}{T}$.

1.8.2. Intrinsic tryptophan Fluorescence and protein ligand binding

Fluorescence can be used to study protein-ligand binding. Fluorescence emission of naturally occurring fluorophores (intrinsic fluorophores) or those externally added to the system (extrinsic fluorophores) can be used as reporters to study dynamics and thermodynamics of binding in several biological phenomena. The most significant intrinsic fluorophore in proteins is the indole group of tryptophan. Intrinsic tryptophan fluorescence can be used to study dynamics and thermodynamics of biding as explained in sections (1.2) and (1.3). Centre of mass for the fluorescence emission spectra and fluorescence intensity are two properties that can be used to study dynamics and thermodynamics of binding. More details about these measurement techniques can be seen in chapter 4.

A protein's intrinsic tryptophan fluorescence depends on the polarity of the solvent in which this fluorophore is dissolved. The indole group in tryptophan can show a displacement in the maximum fluorescence emission spectrum according the solvent used (Stokes shift(29)). The stokes shift can be also useful in order to understand structural changes in the protein during the association process. Tryptophan fluorescence intensity may show Stokes shifts towards lower wavelengths when indole group changes from a polar solvent accessible environment towards a non-polar one. This can be used to understand protein conformational changes upon ligand binding(30). The same principle can be used to gain information about the structure and stability of the transition state. Chapter 3 makes extensive use of NMR dispersion relaxation experiments together with intrinsic tryptophan fluorescence measurements to study dynamics and thermodynamics of protein ligand binding. Kinetics and thermodynamics of binding are used to map volume changes in protein-ligand association processes.

1.9. Biological systems

Experimental results described in chapters 3 through chapter 5 were obtained using several protein-ligand complexes. These biological systems were selected to study dynamics and thermodynamics of binding. The protein used in the first case is the chicken isoform of Src Homology 3 (SH3) binding domain of the tyrosine kinase FYN(31). Chapters 3 and 4 used recombinant protein FYN SH3 domain that binds to a series of dodecapeptides containing a proline rich motif. This short proline motif is recognized by the SH3 domain as a canonical binding sequence.

Chapter 5 briefly describes some techniques used to obtain special patterns of isotopic labeling of human Farnesyl Pyrphosphate Synthase (hFPPS)(32). Isotopically labeled ^{1}H-^{15}N hFPPS was initially expressed and purified to study binding of the protein with bisphosphonates and allosteric inhibitors. However, bidimensional NMR spectra lacked of enough signal resolution to perform these studies. Special isotopic labeling techniques were used aiming to improve NMR spectral quality. Different isotopic labeled versions of hFPPS were successfully expressed and purified. These proteins were nevertheless not suitable to perform NMR experiments to study binding of hFPPS with inhibitors.

1.9.1. Protein interaction domains

Many protein-protein interactions are mediated in nature by modular interaction domains(33). These domains are also important in protein interactions with other biomolecules including DNA, RNA and membrane lipids. Interaction domains are usually 30 to 200 amino acids size proteins that can share similar structural and binding characteristics. They modulate several biological functions including cell growth, polarity, motility, differentiation and signaling. There is a group of interaction domains that recognize proline as a binding target. This domains are called proline recognition domains (PRD's)(34).

A special group of PRD's consist in small ~60 amino acid interaction modules named Src Homology 3 (SH3) domains(35). These domains are ubiquitous in eukaryotes and accomplish a wide variety of functions in signaling processes inside the cell. SH3 domains have evolved to bind to a many different ligands. This binding promiscuity explains in part the implication of SH3 domains in numerous cellular processes. Most of SH3 domains bind to a proline rich motif consisting of the sequence PxxP, where P is proline and x is any amino acid. Proline rich sequences usually binds to SH3 domains in two canonical ways:

+xΦPxΦP or type I, and ΦPxΦPx+ or type II. Where + is a positively charged residue, x is any amino acid, Φ is a hydrophobic residue and P is proline. Both types of proline rich motifs adopt a helical conformational structure called polyproline II (PPII)(36). This is a left-handed helix that is not only recognized by SH3 domains but by all the PRD's(37).

1.9.2. Proline rich motifs and polyproline II conformation

Any amino acid involved in protein binding must be preferentially located in the solvent exposed surface of the protein(37). This makes it more accessible to the binding counterpart. From all the naturally occurring amino acids proline is perhaps the most suitable residue to accomplish this function(38). Proline usually breaks secondary structures such as α-helices and β-sheets(39). These disrupting points are usually exposed to solvent(38). For this reason proline is more likely found on the surface of the protein and less likely found at internal buried residues(38). Furthermore, proline forms a five ring heterocycle between the side chain and its backbone. This restricts the dihedral angle Φ for this residue to an approximate value of -60º which reduces the number of conformations that proline rich peptides can tolerate. The most probable conformation that two or more sequential prolines can adopt consists of polyproline II (PPII). This left handed helix has 3 residues per turn with a conformation less rigid than an ideal alpha helix. An ideal alpha helix has an average pitch of 3.6 residues. PPII conformation occurs naturally when certain number of proline residues are present in a given polypeptide sequence. Formation of PPII helices by free-unbound proline rich motifs seems to reduce the entropy penalty of any binding domain that interacts with these sequences(37). PPII has sidechains and carbonyl groups pointing towards outside the helix, making them more exposed to interact with binding counterparts. Additionally, the lack of an amide proton in proline hinders intra-molecular hydrogen bonds with carbonyl group in a PPII conformation. This gives more freedom to carbonyl groups to interact with binding sites. Changes in the constituent residues in a proline rich region usually preserve the PPII conformation. This is the reason why so many different combinations of proline and non-proline residues form PPII structures. This explains the relative promiscuity of PRD's and the flexibility that SH3 domains show to mediate in binding in so many different cellular signaling processes(40).

1.9.3. Fyn SH3

The Fyn SH3 domain is illustrated in Figure 1.3. It shows a human Fyn SH3 domain binding to a proline rich motive type II: VSLARRPLPPLP (PDB 4EIK). Fyn SH3 domains display a typical beta barrel structure with five anti-parallel beta sheets and several loops. The most significant ones are the n-src loop and the RT loop. The latter is a disordered region that contains a conserved RT amino acid sequence. Fyn associates with type I (+xΦPxΦP) and type II (ΦPxΦPx+) proline rich motives using three binding pockets. Site 1 (Figs. 1.3b, 1.3c) is a selectivity pocket that receives a positively charged residue located at the canonical site (+) in the ligand peptide. Residue (+) forms an ion pair with a negatively charged residue in the binding pocket (D or E). Electrostatic interactions of the charged residue (+) are usually enhanced by long distance electrostatic interactions. These are due to the presence of additional negatively charged residues close to the specificity pocket. Site 2 and site 3 (Figs 1.3b, 1.3c) can either dock consensus proline residues or consensus hydrophobic residues when respectively binds proline rich peptides type I (Fig. 1.3b) or type II (Fig. 1.3c). Experimental results shown in chapter 3 also confirm that proline rich peptides lacking the consensus residue (+) can also bind to the FYN SH3 binding domain. This is a proof that the absence of electrostatics interactions usually present in the selectivity pocket when Fyn binds to proline rich peptides, does not hamper ligand recognition by Fyn.

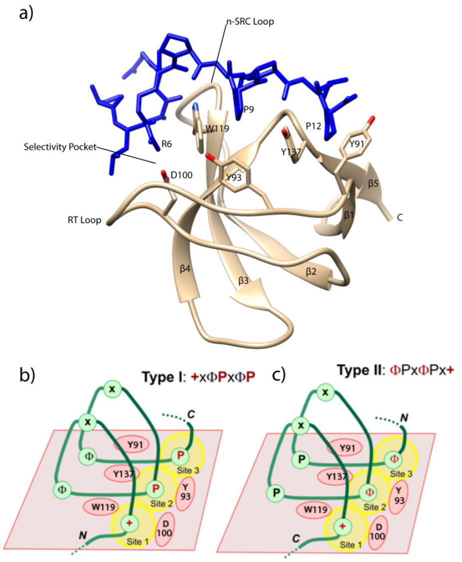

Figure 1.3. Human Fyn SH3 domain binding to peptide VSLARRPLPPLP (PDB 4EIK) (a). Illustration shows binding of a proline rich peptide type I (b) or type II (c) to the SH3 domain.

1.9.4. hFPPS

Human Farnesy Pyrophosphate Synthase (hFPPS)(41) produces Farnesyl pyrophosphate (FPP). This isoprenoid is fundamental for several cellular processes(42). The enzyme acts in the first branching point in the mevalonate pathway(43). At this point, the main function of hFPPS is the condensation of isopentenyl pyrophosphate (IPP) to the target substrate. It first helps in the synthesis of dimethylallyl pyrophosphate (DMAPP) to geranyl pyrophosphate (GPP) by the condensation of a molecule of IPP and subsequently attaches a second molecule of IPP to GPP to produce farnesyl pyrophosphate (FPP). FPP is used in the cell to prenylate GTPases that are involved in several cellular signaling processes. Prenylated GTPases can be then carried out to different cellular locations(44). Blocking prenylation of GTPases can obstruct several specific cellular processes (45). For this reason the design of hFPPS inhibitors is of pharmacological importance. Some inhibitors of hFPSS have been under clinical use for several years (46). These includes nitrogen containing bisphophonates (N-BPs)(47). N-BPs have been effectively used in the treatment of several bone related diseases(48). They are used in treatments where bone re-absorption is required. Additionally, N-BPs have been used for the treatment of bone cancer and have also been explored more broadly as general anticancer agents(49).

N-BPs action on hFPPS has been previously studied through crystallographic and calorimetric studies (50). N-BPs bind to DMAPP/GPP pocket and mimic the natural substrates, thus blocking the binding site. This causes a conformational change that closes the DMAPP/GPP pocket and causes an allosteric conformational change in the C-tail of the protein(51). This causes a partial closure of IPP binding site. Further addition of IPP to the system causes a total closure of IPP pocket and finally locks the protein in an almost irreversible inactive state.

Structural and thermodynamic changes on binding between hFPP and N-BPs has been previously studied (50). However, there is no information reported about binding kinetics for this process. One of the main ideas for the system hFPPs-N-BPs was to apply different NMR techniques in order to understand in more detail the dynamics of binding. The approach used and the results obtained are shown in chapter 5.

2. Analyzing Protein-Ligand Interactions by Dynamic NMR Spectroscopy

I have coauthored this book chapter with:

Anthony Mittermaier

This book chapter was published in:

Mittermaier, A., and Meneses, E. (2013) Analyzing protein-ligand interactions by dynamic NMR spectroscopy. Methods in molecular biology 1008, 243-266

2.1. Summary

Nuclear Magnetic Resonance (NMR) spectroscopy can provide detailed information on protein-ligand interactions that is inaccessible using other biophysical techniques. This chapter focuses on NMR-based approaches for extracting affinity and rate constants for weakly-binding transient protein complexes with lifetimes of less than about a second. Several pulse sequences and analytical techniques are discussed, including line-shape simulations, spin-echo relaxation dispersion methods (CPMG), and magnetization exchange (EXSY) experiments.

Key words: protein dynamics by NMR spectroscopy, NMR relaxation dispersion methods, NMR-derived protein-ligand interactions, line-shape analysis of NMR spectra, protein sample for solution NMR spectroscopy

2.2. Introduction

Solution NMR spectroscopy is a powerful and versatile technique for obtaining structural and dynamic information on biological molecules and complexes (52,53). A wide variety of NMR-based approaches can be applied to different aspects of biological interactions, including the elucidation of the three-dimensional structures (54-56) and internal motions (57,58) of protein complexes, the characterization of transiently-populated states in binding pathways (59,60), the rapid screening of small molecule libraries (61,62), and the determination of the thermodynamic and kinetic parameters of binding. This chapter focuses on the last application, the determination of biophysical interaction parameters by NMR.

NMR offers several advantages compared to alternative techniques for measuring the affinities and timescales of protein interactions. Firstly, NMR spectra are generally quite sensitive to complex formation, even when interactions are weak and are not accompanied by large structural rearrangements (63). Thus NMR is a powerful diagnostic tool for determining whether two molecules interact. Secondly, simple analyses of the spectral changes produced by binding rapidly identify those portions of the molecules that are most involved in the interaction (64,65). Thirdly, NMR can accurately measure the binding kinetics for transient complexes with extremely short bound lifetimes of less than 1 ms (66). Such lifetimes are outside the range of most stopped-flow instruments, because the time required to mix the protein and ligand solutions is comparable to the time required for the binding reaction to proceed nearly to completion. Furthermore, NMR kinetics experiments are performed at equilibrium in solution, which avoids the complication of mass transport effects that are inherent to surface plasmon resonance measurements

(67). Lastly, each NMR-active nucleus in the protein and ligand represents a potential probe of the binding process. Comparisons of data obtained for different nuclei can discriminate between two-state and multi-state binding, and can shed light on mechanisms of allostery (3,59,68). The main disadvantages of using NMR to study binding kinetics are the requirement for quite concentrated (roughly 50 μM to 2 mM) isotopically-labeled protein samples and restrictions on protein molecular weight (less than about 100 kDa (69), although larger systems have been successfully studied).

The following sections will deal mainly with proteins and ligands that bind in a two-state manner with 1:1 stoichiometry, and in which interactions are detected via NMR signals from the protein. In these cases, the binding reaction can be described by the following simple scheme,

$$L + P \underset{k_{off}}{\overset{k'_{on}}{\rightleftarrows}} PL \quad , \tag{2.1}$$

where L and P are the free ligand and protein, PL is the complex, k_{off} is the first-order dissociation rate constant such that $1/k_{off}$ is the average lifetime of the bound state, and k'_{on} is a pseudo-first order association rate constant given by $k_{on}[L]$, where k_{on} is the second-order association rate constant and [L] is the equilibrium concentration of free ligand. The affinity of the interaction is represented by the equilibrium dissociation constant, given by the expression

$$K_D = \frac{[L][P]}{[PL]} = \frac{k_{off}}{k_{on}'} \,. \tag{2.2}$$

The timescale of exchange is described by the parameter k_{ex},

$$k_{ex} = k_{on}' + k_{off} = \frac{k_{off}}{1-f_{PL}} \,, \tag{2.3}$$

where f_{PL} is the fraction of proteins in the bound state. It is evident from this relationship that the timescale of exchange is largely governed by the dissociation rate constant, k_{off}. For example, at the binding midpoint (f_{PL}=0.5) of any system, the exchange rate constant is given by $k_{ex} = 2k_{off}$.

NMR detects ligand binding through changes in the resonant frequencies (chemical shifts) of NMR-active nuclei. Throughout this chapter we will use ω to refer to frequencies expressed in rad s^{-1}, and ν for frequencies expressed in Hz. Suppose that a nucleus in a protein precesses at a frequency ω_P in the absence of ligand. Ligand binding alters the local electronic environment of the nucleus, resulting in a shift of the resonant frequency to ω_{PL}. The resulting NMR signal from the ensemble of nuclei in the sample depends on the fraction of binding sites that are occupied by ligand, f_{PL}, the difference in resonant frequency between the free and bound states, $\Delta\omega = \omega_{PL} - \omega_P$, and the exchange rate, k_{ex}.

When $k_{ex} << \Delta\omega$, the system is in the slow exchange regime and spectra contain separate peaks at ω_P and ω_{PL}. If ligand is gradually added, the intensity (I_P) of the "free" peak at ω_P decreases while the intensity (I_{PL}) of the "bound" peak at ω_{PL} increases, according to $I_{PL} \propto f_{PL}[P]_T$ and $I_P \propto (1-f_{PL})[P]_T$, where $[P]_T$ is the total protein concentration. This is shown for simulated 1D NMR spectra in Fig. 2.1a.

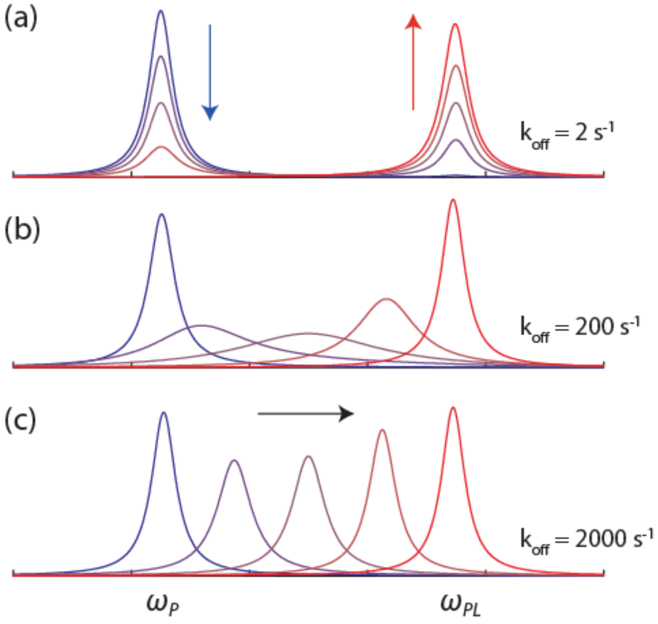

Figure 2.1. Effect of ligand-binding on an NMR signal. Superposition of simulated 1D NMR spectra for a nucleus with a resonant frequency ω_P in the free state and ω_{PL} in the bound state of a protein that is 1%, 25%, 50%, 75%, and 99% ligand-bound. The spectrum of the free state is transformed into that of the bound state in a manner which depends upon the rate of exchange between the two-states. (a) slow exchange regime where $k_{ex} << \Delta\omega$, (b) intermediate exchange regime where kex ≈ $\Delta\omega$ (c) fast exchange regime where $k_{ex} >> \Delta\omega$, where $k_{ex} = k_{off} + k_{on}[L]$ and $\Delta\omega = |\omega_{PL} – \omega_P| = 100\pi$ rad s^{-1}, in the simulations.

In contrast, when $k_{ex} >> \Delta\omega$, the system is in the fast exchange regime and the spectrum contains a single peak at the population-weighted average chemical shift. If ligand is titrated into the sample, the position of the peak gradually shifts from ω_P to ω_{PL}, according to $\omega_{obs} = \omega_P + f_{PL}\cdot\Delta\omega$ (Fig. 1c). Furthermore, when kex and $\Delta\omega$ are of comparable magnitudes, stochastic fluctuations in the resonant frequency caused by ligand association and dissociation lead to weak, broad peaks in NMR spectra (Fig. 2.1b). Thus, analyses of peak shapes, intensities and positions can yield quantitative information on the populations of different conformational states at atomic resolution.

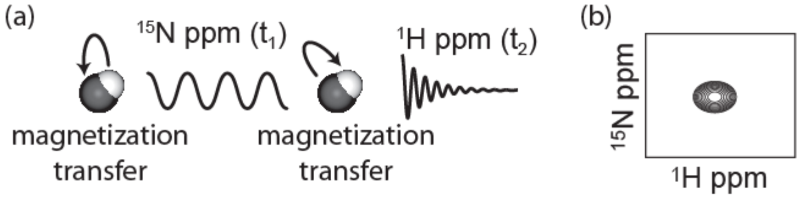

Figure 2.2. Schematic representation of a 2D NMR ^{1}H(white)–^{15}N(gray) correlation experiment. (a) Simulataneous radio-frequency pulses transfer magnetization from ^{1}H to a ^{15}N nucleus to which it is covalently bonded, magnetization evolves on the ^{15}N nucleus during and incremented delay t_1, and is transferred back to ^{1}H where it is detected during a time t_2. (b) Fourier analysis of signal variation during t_1 and t_2 extracts characteristic frequencies for each bonded pair of ^{15}N and ^{1}H nuclei.

NMR studies of proteins typically employ multi-dimensional techniques that resolve individual signals for tens to hundreds of chemically distinct nuclei in the molecules. A common class of experiment correlates the frequencies of directly-bonded ^{15}N and ^{1}H nuclei, as depicted schematically in Fig. 2.2a. In this approach, the equilibrium magnetization of the ^{1}H nucleus is transferred to the directly attached ^{15}N, the ^{15}N frequency is measured indirectly via a variable delay (t_1), the magnetization is transferred back to ^{1}H, and the ^{1}H frequency is directly detected during the acquisition period (t_2) (70). The resultant 2D spectrum contains (at least) one peak for each NH pair, located at the chemical shifts of the ^{1}H and ^{15}N nuclei in the x and y dimensions (Fig. 2.2b, Fig. 2.3). Furthermore, each peak in the 2D spectrum can be assigned to the corresponding nuclei in the protein using standard methods (52). Thus a $^{1}H/^{15}N$ correlation spectrum represents an atomic-resolution "fingerprint" of the protein, and forms the basis for many specialized NMR methods, as described below. Ligand titrations monitored using 2D NMR follow similar exchange behavior to that described above for 1D NMR line-shapes. As an example, a series of protein $^{1}H/^{15}N$ correlation spectra for a ligand titration are overlaid in Fig. 2.3a. The peaks shift rather than doubling as the ligand is added, indicative of association/dissociation kinetics that are fast on the NMR timescale. The residues whose peaks shift the most upon addition of ligand are those which experience the largest changes in local electronic environment due to binding. For this example, chemical shift displacements are mapped onto the three-dimensional structure of the protein in Fig. 2.3b. As expected, the largest changes are observed for residues in the binding site. Chemical shift mapping approaches, such as this, are a very powerful way to identify protein binding sites, provided that the structure of the protein is known (64,65).

Direct inspection and quantitative analysis of NMR line-shapes and titration data can yield information on binding kinetics and affinities, as described in Subsection 2.3.1. In addition, we will consider two specialized dynamic NMR techniques that yield even more detailed information, depending on the timescale of association-dissociation kinetics. In the case of relatively rapid dynamics (k_{ex} values of roughly 10 s^{-1} to 10^4 s^{-1}), Carr-Purcell-Meiboom Gill (CPMG) relaxation dispersion methods can be analyzed to give the populations, interconversion rates, and chemical shift differences of exchanging states (71) (Subsection 2.3.2). In cases of slower binding kinetics (k_{ex} values of roughly 0.5 to 20 s^{-1}) NMR magnetization exchange (EXSY) experiments (72) quantify the kinetics of exchange, and help to correlate protein spectra obtained in the free and bound forms (Subsection 2.3.3).

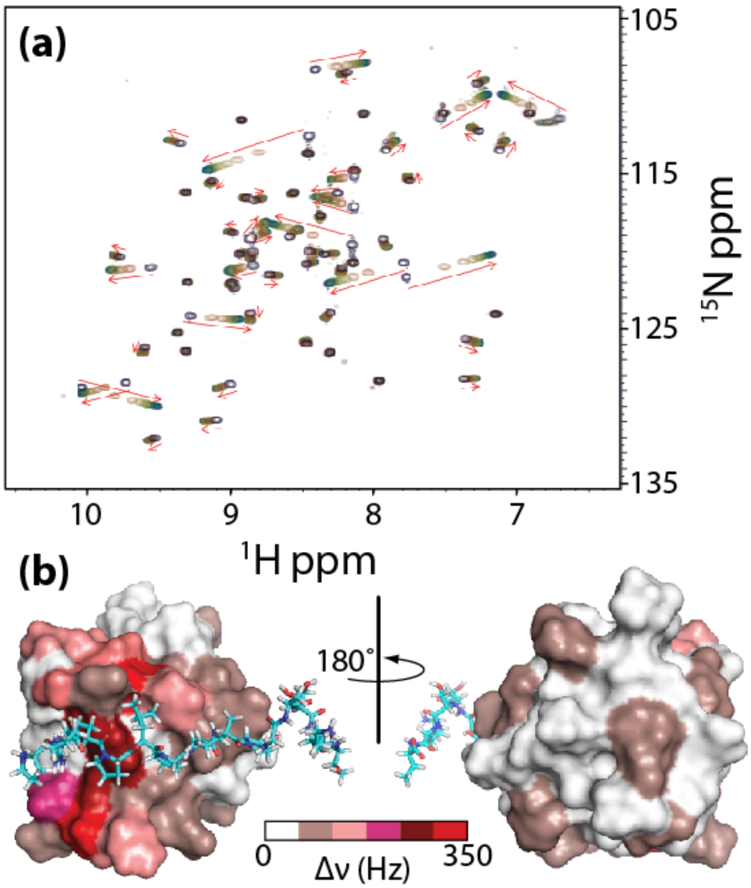

Figure 2.3. Titration monitored by heteronuclear correlation spectroscopy. (a) Overlaid ^{1}H/^{15}N NMR correlation spectra obtained at 18.8 Tesla for a titration of the SH3 domain from the Fyn tyrosine kinase with a proline-rich peptide (Ac-WSLASSPLPPPLP-NH_2). Both fast and intermediate-exchange behaviours are observed. Arrows indicate peak displacements. (b) Maximum ^{1}H peak displacements (Δν) illustrated on the surface of the Fyn SH3 domain bound to a proline-rich peptide (1AZG (73)).

2.3. Materials

2.3.1. NMR samples

In order to study ligand binding using multi-dimensional heteronuclear NMR (as in Fig. 2.2), protein samples need to be isotopically enriched ^{15}N and/or ^{13}C. In the case of larger molecules (with molecular weights greater than about 25 kDa), additional enrichment with ^{2}H can significantly improve spectral quality (74). Isotopically-labeled protein samples can be over-expressed in bacteria grown in minimal media containing $^{15}NH_4Cl$ and/or ^{13}C glucose as the sole sources of nitrogen and/or carbon, respectively (75). Protein samples are typically isolated with several stages of liquid chromatography that often conclude with size-exclusion chromatography. Sample purity is of utmost importance, since even minimal protease contamination can cause extensive protein degradation during data collection. Protein NMR samples are usually 300 to 600 µL in volume, contain 5% to 10% D_2O (for the spectrometer frequency lock), and are usually buffered at a pH below 7.5, since base-catalyzed exchange of hydrogen atoms between protein and solvent can lead to signal loss under more alkaline conditions (76). Samples can also contain small amounts of EDTA and other protease inhibitors, as well as NaN_3 to prevent microbial contamination. The minimum protein concentration required for NMR analyses varies, depending on the spectrometer and particular experiment. In our experience, NMR titrations can be performed with protein concentrations as low as 0.1 to 0.2 mM, using Varian INOVA spectrometers with field strengths of 11.7 to 18.8 T and employing standard room-temperature probes. Analyses of dynamics experiments (CPMG and EXSY) are quite sensitive to uncertainties in peak intensity, and we find that concentrations of about 0.5 to 1.5 mM are preferable.

When preparing ligands for NMR binding studies, it is important to ensure that the buffer conditions match those of the protein sample as closely as possible. Otherwise, addition of the ligand may produce protein spectral changes that are due to perturbation of the solution conditions rather than binding. Buffer matching is most easily accomplished by dialyzing the protein and ligand in separate dialysis membranes in the same container of buffer. Alternatively, powdered ligands may be dissolved directly in the protein dialysis buffer. However, special care must be taken when ligands contain ionizable groups, since dissolving such molecules in the protein buffer can significantly alter the pH. Optimal ligand:protein ratios vary, depending on the experiment (Note 1). NMR titrations should include spectra collected in the absence of ligand, spectra with ligand concentrations spanning the mid-point (f_{PL}=0.5), and spectra of proteins nearly saturated with ligand (Note 2).

CPMG and EXSY experiments require only a single sample; EXSY is most sensitive when both free and bound proteins give intense signals, therefore samples with f_{PL}≈0.5 are preferable. The choice of ligand:protein ratio for CPMG experiments is somewhat more complicated, since the overall exchange rate (k_{ex}) increases with increasing ligand concentration, according to Equation 2.3. The extent of spectral broadening varies with both f_{PL} and k_{ex} (Equation 2.2.18 and Equation 2.2.19), thus careful tuning of the ligand concentration can have a substantial impact on the quality of CPMG data (77). Typically, a bound fraction, f_{PL}, between about 5% and 95% is suitable, since molecules must spend appreciable amounts of time in both the free and bound states in order to produce exchange broadening. A final important consideration is the choice of temperature (Note 3), since this can significantly affect both the affinity and kinetics of binding. In one example, we found that binding kinetics shifted from the slow exchange regime, through the intermediate regime, and into the fast exchange regime as the temperature was raised from 10°C to 50°C (66).

2.3.2. Spectral Analysis

Several different software packages for processing and analyzing NMR spectra are available (for example NMRView (78), matNMR (79), FELIX (Felix NMR Inc.), CcpNmr (80), NMRLab (81), and NMRPipe-NMRDraw (82)). NMR line-shape analyses fit NMR spectra directly, as described in Subsection 2.3.1. This can be accomplished by outputting the spectral data in a generic format (such as text with the pipe2text command in NMRPipe) and applying freely available (83) or in-house scripts. The analysis of EXSY and CPMG data involve fitting peak intensities (volumes), which may be extracted by either automatic or manual peak-picking. In the sections below, kinetic and thermodynamic parameters are extracted from NMR data by minimizing a χ^2 target function,

$$\chi^2 = \sum \frac{\left(Y_{\exp} - Y_{calc}\right)^2}{\delta Y_{\exp}^2}, \tag{2.4}$$

in which Y_{exp} is an experimental datum, δY_{exp} is the associated experimental uncertainty, Y_{calc} is a function of the physical parameters, calculated using one of the equations below, and the sum runs over all data points analyzed. Parameter optimization can be performed using a variety of search algorithms (Simplex, Levenberg-Marquardt, etc. (84)) and software packages, for example MATLAB (Mathworks) or Mathematica (Wolfram Research).

2.4. Methods

2.4.1. Titration analysis

2.4.1.1. NMR-derived binding isotherms

The affinity of a protein-ligand interaction can be determined by analyzing how the fraction of proteins bound to ligand, f_{PL}, depends on the total concentration of ligand, [L]T. Rearrangement of Equation **2.2** yields the simple relationship,

$$f_{PL} = \frac{[L]}{[L]+K_D}, \tag{2.5}$$

where [L] is the concentration of free ligand and K_D is the equilibrium dissociation constant. When the concentration of protein is extremely low ($<0.01\times K_D$), the amount of bound ligand is negligible compared to the total ligand concentration and $[L]\approx[L]_T$, yielding the familiar Langmuir binding isotherm (85). However, this situation rarely holds in NMR titrations, since the technique requires protein concentrations that are greater than about 100 μM. Instead, the quadratic form of the binding isotherm applies (86):

$$f_{PL} = \frac{1}{2}\left(1+r_L+\frac{1}{c}-\sqrt{\left(1+r_L+\frac{1}{c}\right)^2-4r_L}\right), \tag{2.6}$$

where $r_L = [L]_T/[P]_T$ and $c = [P]_T/K_D$. This has implications for the range of affinities that may be determined by NMR. A series of simulated binding isotherms for titrations with a total protein concentration of 100 μM and affinities ranging from 10 mM to 10 nM are shown in Fig. 2.4. Notably, the titration midpoints are nearly identical for $K_D \leq 10$ μM, and the curves are virtually superimposable for $K_D \leq 1$ μM. This is due to the fact that when $[P]_T$ greatly exceeds K_D, nearly all added ligand binds immediately to protein, until the binding sites are saturated. In other words, when $[P]_T >> K_D$ and $[P]_T > [L]_T$, $f_{PL} \approx r_L = [L]_T/[P]_T$, independently of KD. Thus values of K_D that are significantly less than the protein concentration cannot be determined with accuracy using this technique. Fortunately, many interactions of biological importance have relatively weak affinities that are readily characterized using NMR.

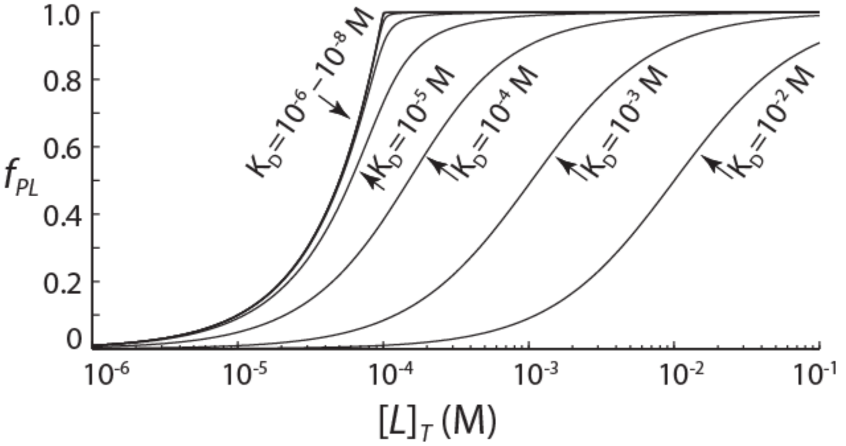

Figure 2.4. Simulated binding isotherms (fraction protein bound, f_{PL}, versus total ligand concentration, $[L]_T$) for titrations of a 100 μM protein sample with ligands whose equilibrium dissociation constants range from 10^{-2} M to 10^{-8} M.

In the case of slow association/dissociation kinetics, NMR spectra obey the expressions

$$I_{PL}\left(\left[L\right]_T\right)_i = \lambda_{PL,i} \cdot f_{PL} \cdot \left(\frac{V_0}{V_0 + V_L}\right)$$

$$I_P\left(\left[L\right]_T\right)_i = \lambda_{P,i} \cdot \left(1 - f_{PL}\right) \cdot \left(\frac{V_0}{V_0 + V_L}\right) \tag{2.7}$$

where $I_{PL}([L]_T)_i$ and $I_P([L]_T)_i$ are the peak intensities of residue i in the bound and free forms for a given ligand concentration, $[L]_T$, V_0 is the initial sample volume, V_L is the volume of added ligand solution, $\lambda_{PL,i}$ and $\lambda_{P,i}$ are normalization constants, and f_{PL} is given by Equation 2.6. Peak intensities can be fitted simultaneously (using Equation 2.7) to yield $\lambda_{PL,i}$ and $\lambda_{P,i}$ on a per-peak basis and a single global value of K_D. The term $V_0/(V_0+V_L)$ accounts for dilution of the protein sample, with the assumption that peak intensity is directly proportional to protein concentration.

In the case of fast association/dissociation kinetics, the displacement of peak i from its initial location in the spectrum is given by the expression

$$\omega_{disp,i}\left(\left[L\right]_T\right) = f_{PL} \cdot \Delta\omega_i \, , \tag{2.8}$$

where f_{PL} is again given by Equation 2.6, $\Delta\omega_i = \omega_{PL,i} - \omega_{P,i}$, and $\omega_{PL,i}$, $\omega_{P,i}$ are the resonant frequencies of nucleus i in the bound and free states, respectively. When 2D NMR datasets are employed, displacements in the two frequency dimensions can be analyzed separately (Fig. 2.5). Peak positions can be fitted simultaneously to yield a global value of K_D, as well as $\Delta\omega_i$ values on a per-nucleus basis (usually this means one value of $\Delta\omega_i$ per peak per spectral dimension). An example of this analysis is shown in Fig. 2.5, for the peak displacements illustrated in Fig. 2.3.

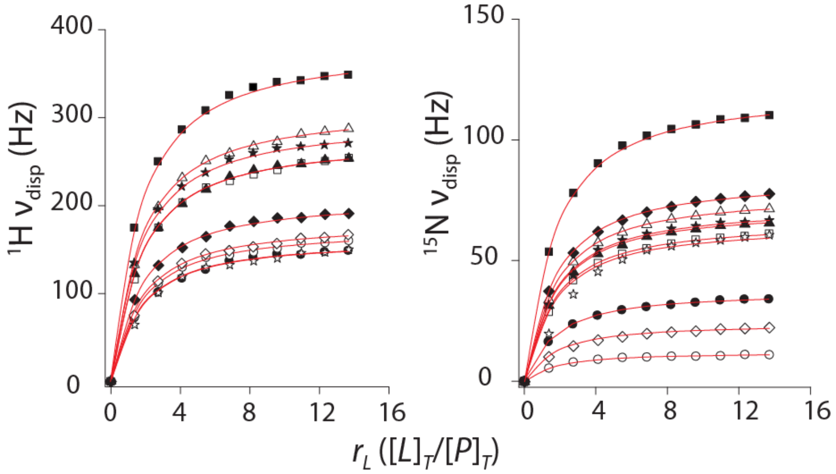

Figure 2.5. Dissociation constant from a global analysis of ^{15}N and ^{1}H chemical shift displacements ($\nu_{disp} = \omega_{disp}/(2\pi)$). Displacements for amide groups of the Fyn SH3 domain, titrated with a proline-rich peptide, as illustrated in Fig. 2.3, plotted as a function of the mole ratio of ligand:protein, r_L. The lines represent the best fit according to a simultaneous analysis of all data using Equations 2.6 & 2.8.

2.4.1.2. Line-shape analysis

Association/dissociation kinetics can lead to time-dependent fluctuations in chemical shifts that cause NMR signals to become broadened, as illustrated in

Fig. 2.1. The effect of dynamics on NMR line-shapes can be quantitatively modeled, permitting kinetic parameters to be extracted by non-linear least-squares fitting. A compact mathematical formulation of the problem treats the precession and transverse relaxation of magnetization as rotation and decay in the complex plane, according to the expressions

$$G(t) = e^{i\omega t} \cdot e^{-R_2^0 t}$$

$$\frac{dG(t)}{dt} = \left(i\omega - R_2^0\right) \cdot G(t) \quad , \qquad (2.9)$$

where G(t) represents the time-domain NMR signal, ω is the frequency of precession, and $\boldsymbol{R_2^0}$ is the transverse relaxation rate (87). In the case of 1:1 stoichiometry, association/dissociation kinetics are described by the coupled differential equations:

$$\frac{d}{dt}[P] = -k'_{on}[P] + k_{off}[PL]$$

$$\frac{d}{dt}[PL] = +k'_{on}[P] - k_{off}[PL] \quad . \qquad (2.10)$$

Combining Equations 2.9 and 2.10 gives the matrix form of the McConnell Equations (88),

$$\frac{d}{dt}\begin{bmatrix} G_P(t) \\ G_{PL}(t) \end{bmatrix} = \mathbf{A}\begin{bmatrix} G_P(t) \\ G_{PL}(t) \end{bmatrix} , \qquad (2.11)$$

where

$$\mathbf{A}=\begin{bmatrix} i\omega_P - R_{2,P}^0 - k'_{on} & k_{off} \\ k'_{on} & i\omega_{PL} - R_{2,PL}^0 - k_{off} \end{bmatrix}$$

, $k'_{on} = f_{PL}k_{ex}$, $k_{off} = f_P k_{ex}$ and $f_P + f_{PL} = 1$.

The total time-domain signal is then given by

$$G(t) = G_P(t) + G_{PL}(t) = \begin{bmatrix} 1 & 1 \end{bmatrix} \exp\{\mathbf{A}\mathrm{t}\} \begin{bmatrix} G_P(0) \\ G_{PL}(0) \end{bmatrix}, \qquad (2.12)$$

where $G_P(0)=f_P$, $G_{PL}(0)=f_{PL}$ and the matrix exponential can be evaluated numerically. The 1D NMR spectrum, g(ω), is given by the Fourier transform of G(t). These calculations can be extended to systems of arbitrary complexity by increasing the number of states and adding appropriate exchange terms (83). In the case of two-state exchange, g(ω) has the analytical solution (89,90)

$$g(\omega) = \lambda \frac{\left(P\left[1+\tau\left(f_{PL}R_{2,P}^0 + f_P R_{2,PL}^0\right)\right] + QU\right)}{P^2 + U^2}, \qquad (2.13)$$

where

$$P = \tau\left(R_{2,P}^0 R_{2,PL}^0 - (\bar{\omega}-\omega)^2 + \tfrac{1}{4}\Delta\omega^2\right) + f_P R_{2,P}^0 + f_{PL} R_{2,PL}^0,$$

$$Q = \tau\left(\bar{\omega} - \omega - \tfrac{1}{2}\Delta\omega\left(f_P - f_{PL}\right)\right),$$

$$U = (\bar{\omega}-\omega)\left(1+\tau\left(R_{2,P}^0 + R_{2,PL}^0\right)\right) + \tfrac{1}{2}\Delta\omega\left(R_{2,PL}^0 - R_{2,P}^0 + f_P - f_{PL}\right),$$

$$\bar{\omega} = \tfrac{1}{2}\left(\omega_P + \omega_{PL}\right),$$

$$\tau = k_{ex}^{-1} = \frac{1-f_{PL}}{k_{off}}$$

and λ is a normalization constant. Although the equations above were derived for 1D NMR spectra, they can also be applied to peak cross-sections extracted from multi-dimensional spectra, provided that peak heights are scaled to account for broadening of the other nuclei (83). An NMR line-shape analysis of titration data comprising spectra obtained with a range of ligand concentrations can yield global values of K_D and k_{off}, as well as normalization constants, λ, free and bound resonant frequencies, ω_P, ω_{PL}, and free and bound transverse relaxation rates, $\boldsymbol{R^0_{2,P}}$, $\boldsymbol{R^0_{2,PL}}$, for each nucleus studied. When NMR data deviate significantly from the two-state model, such as when additional peaks appear during a titration, this implies that the binding mechanism includes more than two well-populated states (91).

2.4.2. Carr-Purcell-Meiboom-Gill (CPMG) experiments

2.4.2.1. CPMG overview

As discussed above, association/dissociation dynamics can lead to stochastic fluctuations in nuclear precession frequencies on ms to μs timescales. This dephases transverse magnetization and results in an added contribution to transverse relaxation, such that

$$R_2 = R_2^0 + R_{ex}, \tag{2.14}$$

where R_2 is the observed transverse relaxation rate, R_{ex} is the exchange contribution, and $\boldsymbol{R_2^0}$ is the relaxation rate in the absence of exchange. Line-shape analyses fit R_2, and thus R_{ex} indirectly, since peak height is proportional to $1/R_2$ and the full width at half height is equal to R_2/π. In contrast, Carr-Purcell-Meiboom-Gill (CPMG) experiments can provide detailed dynamical exchange information by studying R_{ex} more directly (92,93). In the CPMG approach, R_2 is measured while R_{ex} is suppressed with variable numbers of refocusing pulses applied during a constant relaxation delay (Fig. 6a) (71). The dependence of R_2, and hence R_{ex}, on the pulse repetition rate can be analyzed to extract the populations, exchange rates and chemical shifts of interconverting states (94). There are other advantages to the CPMG approach. Whereas, line-shape analyses require a series of spectra be recorded as ligand is titrated into the sample, CPMG experiments require only a single NMR sample. Furthermore, CPMG experiments can yield detailed information on weakly-populated protein states that are "invisible" in standard NMR correlation spectra (95).

The CPMG experiment is based on the Hahn spin-echo experiment, which consists of two equal delays of length τ, during which magnetization precesses (rotates) in the transverse plane, separated by a 180° refocusing pulse (τ-180-τ) (96). A spin's precession is completely refocused during the spin echo, provided that its precession frequency is equal in the two τ periods (Fig. 2.6a). If an association or dissociation event causes a change in frequency ($\omega_P \leftrightarrow \omega_{PL}$) during the spin echo, the magnetization is incompletely refocused, which contributes to dephasing of the NMR signal and consequent loss of intensity. When pulses are applied infrequently (large τ), at least one association/dissociation event will occur during most τ delays, magnetization is largely de-phased, and the resulting NMR signal is weak. When pulses are applied rapidly, most pairs of τ delays are free of association/dissociation events, magnetization is largely refocused, and the resulting NMR signal is strong (Fig. 2.6b). Transverse relaxation rates (Fig. 2.6c) are directly related to peak intensities by the expression

$$R_2(\nu_{CPMG}) = -\frac{1}{T_{relax}}\ln\left(\frac{I(\nu_{CPMG})}{I_0}\right) \tag{2.15}$$

where $\nu_{CPMG} = (4\tau)^{-1}$, $I(\nu_{CPMG})$ is the intensity of the peak obtained with a given pulse repetition rate, Trelax is the length of the relaxation delay, and I_0 is the intensity measured when T_{relax}=0. Optimization of the length of T_{relax} is important in obtaining good signal intensity throughout the range of ν_{CPMG} values used (Note 4).

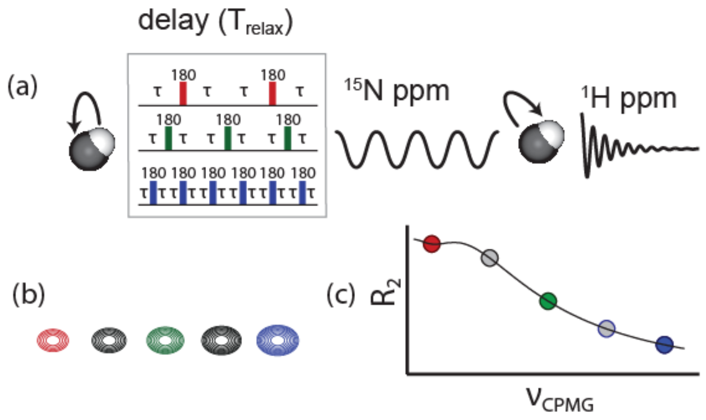

Figure 2.6. Schematic representation of a ^{15}N CPMG experiment. (a) Equilibrium magnetization is transferred from the ^{1}H to the ^{15}N nucleus, the signal is then allowed to decay for a period Trelax, during which refocusing pulses are applied at times characterized by a delay τ, magnetization is returned to the attached ^{1}H, and the signal is detected. Each ^{1}H/^{15}N spin pair is characterized by two frequencies and a signal intensity which depends on the number exchange events during T_{relax} (b) The experiment is repeated with different numbers of refocusing pulses applied during T_{relax}, yielding a series of 2D spectra with peak intensities that vary as a function of $\nu_{CPMG}=1/(4\tau)$. (c) The dispersion profile is calculated based on these peak intensities and Equation 2.2.15.

Diverse CPMG experiments have been developed to measure the exchange broadening of different types of nucleus and magnetization (97-103), and to characterize the structures and dynamics of excited protein states (104-106). In addition, $R_{1\rho}$ relaxation dispersion experiments are similar to CPMG methods, with continuous-wave radio-frequency irradiation replacing trains of refocusing pulses (107). Here we focus on CPMG experiments directed at single-quantum coherences, as illustrated schematically for an ^{15}N/^{1}H spin pair in Fig. 2.6 (71,108).

2.4.2.2. CPMG data analysis

The shape of the CPMG relaxation dispersion profile (i.e. the CPMG frequency dependence of R_2 – Fig. 2.6c) can be calculated numerically, analogously to Equation 2.2.11. In the case of two-state exchange, the magnetization following n pairs of spin echoes, n×(τ-180-τ- τ-180-τ) is given by (94)

$$\begin{bmatrix} \boldsymbol{G_P(n)} \\ \boldsymbol{G_{PL}(n)} \end{bmatrix} = (\mathbf{exp\{A\tau\}\ exp\{B\tau\}\ exp\{B\tau\}\ exp\{A\tau\}})^{\boldsymbol{n}} \begin{bmatrix} \boldsymbol{G_P(0)} \\ \boldsymbol{G_{PL}(0)} \end{bmatrix} \qquad (2.16)$$

where

$$\mathbf{A} = \begin{bmatrix} -R^0_{2,P} - k'_{on} & k_{off} \\ k'_{on} & i\Delta\omega - R^0_{2,PL} - k_{off} \end{bmatrix},$$

$$\mathbf{B} = \begin{bmatrix} -R^0_{2,P} - k'_{on} & k_{off} \\ k'_{on} & -i\Delta\omega - R^0_{2,PL} - k_{off} \end{bmatrix},$$

$\Delta\omega=\omega_{PL}-\omega_P$, $G_P(0)=f_P$ and $G_{PL}(0)=f_{PL}$. The opposite signs of the $i\Delta\omega$ terms in A and B account for the refocusing of precession during each spin echo. The transverse relaxation rate, R_2, of the unbound peak can be obtained for any value of T_{relax} and ν_{CPMG} using the expression

$$\boldsymbol{R_2(n) = -\frac{1}{4n\tau}\ln\left(\frac{G_P(n)}{G_P(0)}\right)} \tag{2.17}$$

where $\tau = 1/(4\nu_{CPMG})$ and $n = \nu_{CPMG} \times T_{relax}$.

If separate peaks are obtained for the free and bound forms (i.e. for systems in the slow exchange regime), the R_2 value for the bound peak can be obtained by substituting G_P with G_{PL} in the expression above. It is assumed that $\boldsymbol{R^0_{2,P} = R^0_{2,P}}$ in the expressions above, since the intrinsic relaxation rates of the protein are generally not dramatically affected by ligand binding, and it is not possible, in general, to extract separate values for $\boldsymbol{R^0_{2,P}}$ and $\boldsymbol{R^0_{2,P}}$from CPMG data (109) (Note 5). This approach for calculating CPMG relaxation dispersion profiles can be generalized to systems containing arbitrary numbers of states by extending the matrices A and B of Equation 2.16 with additional chemical shift differences ($\Delta\omega$) and relaxation rates (R_2) along the diagonal together with exchange rate constants in the appropriate elements (110).

In the case of two-state exchange, the transverse relaxation rate of the more populated form ($R_{2,A}$) is given by the analytical expression (111,112)

$$R_{2,A}\left(\nu_{CPMG}\right) = \tfrac{1}{2}\left(R^0_{2,A} + R^0_{2,B} + k_{ex} - 2\nu_{CPMG}\cosh^{-1}\left(D_+\cosh\left(\eta_+\right) - D_-\cosh\left(\eta_-\right)\right)\right) \tag{2.18}$$

where

$$D_{\pm} = \tfrac{1}{2}\left(\pm 1 + \frac{\psi + 2\Delta\omega^2}{\sqrt{\psi^2 + \xi^2}} \right),$$

$$\eta_{\pm} = \frac{\sqrt{2}}{4\nu_{CPMG}} \sqrt{\pm\psi + \sqrt{\psi^2 + \xi^2}},$$

$$\psi = \left(R^0_{2,A} - R^0_{2,B} + f_B k_{ex} - f_A k_{ex} \right)^2 - \Delta\omega^2 + 4 f_A f_B k_{ex}^2,$$

$$\xi = 2\Delta\omega\left(R^0_{2,A} - R^0_{2,B} + f_B k_{ex} - f_A k_{ex} \right),$$

$$\left(A,B\right) = \begin{cases} \left(P,PL\right), & f_{PL} \le 0.5 \\ \left(PL,P\right), & f_{PL} \ge 0.5 \end{cases}.$$

This expression applies to the signal from the major form of the protein (i.e. to the free state where ligand concentration is relatively low, and to the bound state close to saturation). In the limit of fast exchange ($k_{ex} >> \Delta\omega$) this equation is well approximated by the simpler expression (113)

$$R_2\left(\nu_{CPMG}\right) = f_P R^0_{2,P} + f_{PL} R^0_{2,PL} + \frac{\Phi_{ex}}{k_{ex}}\left(1 - \frac{4\nu_{CPMG}}{k_{ex}} \tanh\left(\frac{k_{ex}}{4\nu_{CPMG}} \right) \right), \qquad (2.19)$$

where $\Phi_{ex} = f_P f_{PL} \Delta\omega^2$.

A typical CPMG experiment consists of series of roughly ten to twenty 2D correlation spectra obtained with a range of ν_{CPMG} values and yielding R_2 values for each amide, calculated using Equation 2.2.15. For systems in intermediate timescale exchange, the analysis proceeds with non-linear least-squares fitting of R_2 values using Equation 2.2.18, while for systems in fast exchange Equation 2.2.19 is employed. The exchange regime can be determined from an inspection of line-shapes throughout the titration, as discussed in Section 2.1. Series of experiments should be performed at a minimum of two different static magnetic field strengths under otherwise identical conditions (114) (Note 3). Additional information useful in selecting the appropriate equation for analyses is provided by the dependence of exchange broadening at different static field strengths as expressed by the parameter α (115)

$$\alpha = \frac{d \ln R_{ex}}{d \ln B_0} \quad , \qquad (2.20)$$

where B_0 is the NMR spectrometer field strength and R_{ex} is the exchange contribution to transverse relaxation. R_{ex} may be estimated as the difference between the experimental R_2 values obtained with maximal and minimal ν_{CPMG} (i.e. the reduction in R_2 with increasing frequency). In the intermediate exchange regime, $\alpha \approx 1$, and R_{ex} scales roughly linearly with field strength. In the fast exchange regime, $\alpha \approx 2$, and R_{ex} scales as the square of the field strength. Note that different peaks may be in different exchange regimes depending on their values of Δω, such that data for peaks with smaller Δω values may obey the fast-exchange Equation 2.2.19, while peaks with larger Δω values may require the intermediate exchange Equation 2.2.18.

Fits of multiple-field data from one residue using Equation 2.2.18 yield the parameters k_{ex}, f_{PL}, and $\Delta\omega^2$, and an $\boldsymbol{R_2^0}$ value for each spectrometer field strength (again assuming that $\boldsymbol{R_{2,P}^0} = \boldsymbol{R_{2,PL}^0} = \boldsymbol{R_2^0}$)(Fig. 2.7a). The dissociation rate constant is then given by $k_{off} = (1-f_{PL})k_{ex}$ and the second-order association rate constant is calculated as $k_{on}=K_D/k_{off}$. Fits with the fast-exchange Equation 2.2.19 yield the parameters k_{ex}, Φ_{ex}, and values of $\boldsymbol{R_2^0}$ (Fig. 2.7b). Note that in the fast exchange regime, f_{PL} and $\Delta\omega^2$ cannot be determined separately, as both are subsumed into Φ_{ex}. In this case, the value of f_{PL} can be determined from observed peak displacements relative to the maximum peak displacements (ligand-free versus ligand-saturated spectra) according to Equation 2.8, or from an analysis of dependence of Φ_{ex} on $\Delta\omega^2$ (Note 7). More accurate results can be obtained by fitting dispersion profiles for all residues simultaneously, with values of k_{ex} and f_{PL} optimized globally and values of $\Delta\omega^2$ and $\boldsymbol{R_2^0}$ extracted on a per-residue basis (116). If exchange for all residues is in the fast regime, then only k_{ex} is determined globally, while Φex and $\boldsymbol{R_2^0}$ are obtained on a per-residue basis. The extracted values of $\Delta\omega^2$ or Φ_{ex} can be used to validate the use of the two-state exchange model (Note 7).

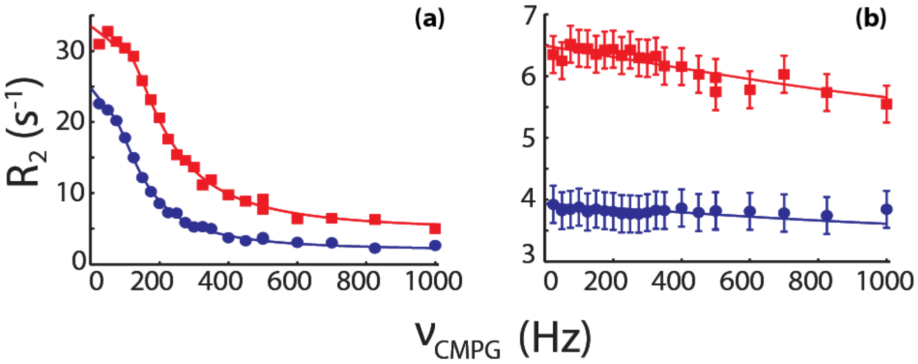

Figure 2.7. Exchange rates from CPMG dispersion curves. Data for Thr14 in the Fyn SH3 domain, partially saturated with proline rich peptides, obtained at 11.7 T (circles) and 18.8 T (squares). (a) Protein 7% bound to a peptide with sequence Ac-WSLARRPLPPLP-NH_2. Exchange is in the intermediate regime, with $k_{off} \approx 200\ s^{-1}$. Lines correspond to best fits with Equation 2.2.18. (b) Protein is 10% bound to a peptide with sequence Ac-WSLASSPLPPPLP-NH_2. Exchange is in the fast regime, with koff ≈ 2000 s^{-1}. Lines correspond to best fits with Equation 2.2.19.

2.4.3. Magnetization exchange spectroscopy (EXSY)

2.4.3.1. EXSY overview

EXSY techniques can be applied when association/dissociation kinetics are slow on the NMR chemical shift timescale. Under these conditions, separate peaks are observed for some residues in the bound and free forms of the protein midway through titrations with ligand (Fig. 2.1a). EXSY experiments are essentially simple variants of multi-dimensional pulse sequences with delays inserted between the indirect and direct acquisition periods. For example, exchange rates may be quantified using a modified $^1H/^{15}N$ correlation experiment that includes a variable delay of length T_{mix} between the ^{15}N and ^{1}H chemical shift detection periods (72), as illustrated schematically in Fig. 2.8. If a free protein binds a ligand during T_{mix}, it will give rise to a cross-peak at ($\omega_P(^{15}N)$, $\omega_{PL}(^{1}H)$). Conversely, if a bound protein releases its ligand during T_{mix}, it will give rise to a cross-peak at (($\omega_{PL}(^{15}N)$, $\omega_P(^{1}H)$). Each exchanging amide group can therefore produce four peaks in this experiment: two self-peaks corresponding to the free and bound forms, and two cross-peaks that are produced by interconversion (Note 8). The intensities of self-peaks and cross-peaks vary as a function of the mixing time T_{mix} and depend on the association and dissociation rate constants, k'_{on} and k_{off}, as well as the longitudinal ^{15}N relaxation rates in the two states, $R_{1,P}$ and $R_{1,PL}$. The intensities of the cross-peaks are low when $T_{mix} \approx 0$, increase due to exchange at moderate values of T_{mix}, and ultimately decay due to the dominant effect of longitudinal relaxation at large T_{mix}. Intensities of the self-peaks are initially high and decrease because of both interconversion and longitudinal relaxation. The dependences of self-peak and cross-peak intensities on Tmix can be analyzed to yield binding kinetic information, as described below.

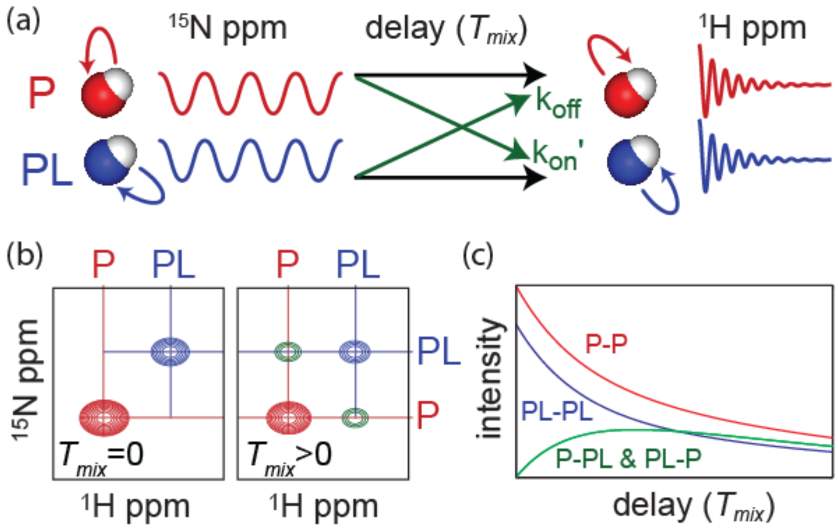

Figure 2.8. Schematic representation of an EXSY pulse sequence. Equilibrium ^{1}H magnetization is transferred to the directly attached ^{15}N, the resonant frequency is measured, magnetization is aligned along the z-axis during T_{mix}, the magnetization is returned to the ^{1}H and the signal is detected. (b) Simulated spectra for a ^{1}H/^{15}N spin pair undergoing slow exchange. Diagonal peaks P and PL correspond to the self-peaks of a residue in the free and bound states respectively, while the off-diagonal cross-peaks are produced by ligand association and dissociation during T_{mix}. (c) Simulated intensity profiles calculated using Equation 2.2.23.

2.4.3.2. EXSY data analysis

Magnetization exchange during T_{mix} is described by the differential equation (94):

$$\frac{\partial}{\partial t}\begin{bmatrix} I_P(t) \\ I_{PL}(t) \end{bmatrix} = -\begin{bmatrix} k_{on}^{'} + R_{1,P} & -k_{off} \\ -k_{on}^{'} & k_{off} + R_{1,PL} \end{bmatrix}\begin{bmatrix} I_P(t) \\ I_{PL}(t) \end{bmatrix} \tag{2.21}$$

where $I_P(t)$ and $I_{PL}(t)$ are the instantaneous signal intensities of the free and bound states at time t, and $R_{1,P}$ and $R_{1,PL}$ are the ^{15}N longitudinal relaxation rates. Integration of Equation 2.2.21 gives the following expression for the intensities of the auto-peaks (I_{P-P} and I_{PL-PL}) and cross-peaks (I_{P-PL} and I_{PL-P}) after the T_{mix} period:

$$\begin{bmatrix} I_{P-P}\left(T_{mix}\right) & I_{PL-P}\left(T_{mix}\right) \\ I_{P-PL}\left(T_{mix}\right) & I_{PL-PL}\left(T_{mix}\right) \end{bmatrix} = \exp\left\{-T_{mix}\begin{bmatrix} k_{on}^{'} + R_{1,P} & -k_{off} \\ -k_{on}^{'} & k_{off} + R_{1,PL} \end{bmatrix}\right\}\begin{bmatrix} I_P(0) & 0 \\ 0 & I_{PL}(0) \end{bmatrix} \quad (2.22)$$

where $I_P(0)$ and $I_{PL}(0)$ are the amounts of magnetization for the free and bound forms immediately preceding the T_{mix} delay. Solving the matrix exponential gives (94):

$$I_{P-P} = I_P^0 \frac{\left(a_{11} - \lambda_2\right)e^{-\lambda_1 T_{mix}} + \left(\lambda_1 - a_{11}\right)e^{-\lambda_2 T_{mix}}}{\lambda_1 - \lambda_2}$$

$$I_{PL-PL} = I_{PL}^0 \frac{\left(a_{22} - \lambda_2\right)e^{-\lambda_1 T_{mix}} + \left(\lambda_1 - a_{22}\right)e^{-\lambda_2 T_{mix}}}{\lambda_1 - \lambda_2}$$

$$I_{P-PL} = I_P^0 \frac{\left(a_{21}\, e^{-\lambda_1 T_{mix}} - a_{21}\, e^{-\lambda_2 T_{mix}}\right)}{\lambda_1 - \lambda_2}$$

$$I_{PL-P} = I_{PL}^0 \frac{\left(a_{12}\, e^{-\lambda_1 T_{mix}} - a_{12}\, e^{-\lambda_2 T_{mix}}\right)}{\lambda_1 - \lambda_2} \quad (2.23)$$

where

$$\lambda_{1,2} = \frac{1}{2}\left(a_{11} + a_{22}\right) \pm \sqrt{\left(a_{11} + a_{22}\right)^2 + 4k_{on}^{'}k_{off}}$$

$$a_{11} = R_{1,P} + k_{on}^{'},\ a_{12} = -k_{off},\ a_{21} = -k_{on}^{'},\ a_{22} = R_{1,PL} + k_{off}$$

A typical EXSY dataset consists of roughly ten to twenty 2D correlation spectra obtained with T_{mix} varying between zero and the maximum value at which reasonably strong signals are still observable. ^{15}N longitudinal relaxation sets the upper limit for Tmix at about one second. Peak intensities are then fitted using Equation 2.2.23 to yield k'_{on}, k_{off}, $R_{1,P}$, $R_{1,PL}$, $I_P(0)$, and $I_{PL}(0)$. As for CPMG data, more accurate values can be obtained by analyzing data for all residues simultaneously to give global values of k'_{on}, k_{off}, together with $R_{1,P}$, $R_{1,PL}$, $I_P(0)$, and $I_{PL}(0)$ on a per-residue basis. It is assumed in Equation 2.2.22 and Equation 2.2.23 that exchange during the transfer of magnetization from ^{15}N back to ^1H following T_{mix} can be neglected. When exchange is sufficiently rapid, non-negligible exchange occurs during the transfer steps, and cross-peaks are observed even with $T_{mix} = 0$. In this case, Equation 2.2.22 can be modified to account for the observed back-transfer according to (66):

$$\begin{bmatrix} I_{P-P}(obs) & I_{PL-P}(obs) \\ I_{P-PL}(obs) & I_{PL-PL}(obs) \end{bmatrix} = \begin{bmatrix} 1 & y_{PL-P} \\ y_{P-PL} & y_{PL} \end{bmatrix} \begin{bmatrix} I_{P-P}(T_{mix}) & I_{PL-P}(T_{mix}) \\ I_{P-PL}(T_{mix}) & I_{PL-PL}(T_{mix}) \end{bmatrix} \tag{2.24}$$

where y_{PL} accounts for differential relaxation of the auto peaks, y_{PL-P} and y_{P-PL} account for dissociation and association during the back-transfer of magnetization, respectively, and all three parameters are optimized on a per-residue basis in global fits of EXSY data.

Additional experiments can be used to analyze dynamics in the low region of the ms-μs time scale motions. These are NMR spin relaxation in the rotating frame ($R_{1\rho}$) and chemical exchange saturation transfer (CEST). The last experiment enables to detect and characterize excited-states with lifetimes ranging from ~5 to 50 ms. However, these experiments are out of the scope of the present document.

2.5. Notes

2.5.1. NMR Titrations

1. An important consideration when performing NMR titration experiments is the selection of ligand concentrations. If an approximate affinity constant is already known, the appropriate ligand concentrations can be chosen using Equation 2.6 so as to adequately define the saturated baseline and the curvature of the binding isotherm. The situation is more complicated if no prior information on the affinity is available. This is particularly true in the case of fast exchange, since peak displacements can only be quantitatively related to f_{PL} once the saturated baseline is obtained, i.e. once the titration is complete. In this case, it is advisable to collect several ($\geq$5) spectra over ligand:protein ratios (r_L) from 0 to about 1.5. If the interaction is of high affinity ($[P]_T > K_D$) saturation will be reached over this interval. If peak displacements vary linearly with $[L]_T$ past the stoichiometric equivalence point (r_L=1), then $K_D > [P]_T$ and larger increments of $[L]_T$ can be used for additional titration points.

2. When performing titrations it is critical that the ligand and protein solutions are mixed thoroughly and that sample loss during the mixing procedure is minimized.

We recommend withdrawing the sample from the NMR tube completely, using a Hamilton syringe or an NMR long-tip pipette, and transferring it to small (≈1.5 mL) sample tube. Ligand can then be added using a standard pipettor, the sample can be thoroughly mixed, spun down, and returned to the NMR tube using the syringe. It is preferable to use the same NMR tube, sample tube, and syringe for every titration step (without rinsing) in order to minimize loss of the sample.

2.5.2. CPMG experiments

3. Temperature control is a major concern in studies of relaxation, particularly when performing CPMG studies as data from more than one spectrometer are analyzed assuming that protein dynamics (and hence temperatures) are identical in all instruments. Calibration curves can be constructed for each NMR probe using perdeutarated methanol to measure the true sample temperature (117). In this case, $T(K) = -16.7467\ (\Delta\delta)^2 - 52.5130\ \Delta\delta + 419.1381$, ($\Delta\delta = \delta_{OH} - \delta_{CHD2}$) (118), where δ is expressed in ppm. Alternatively, a non-magnetic digital thermometer may be inserted directly into the NMR probe. Another issue is heating caused by RF pulses, particularly when proton decoupling is applied during the relaxation delay (108). This effect can be assayed by measuring the water resonance frequency (unlocked) before and after several minutes of

irradiation with the pulse sequence, as the water resonance shifts by approximately -.01 ppm K^{-1} (119). The temperature setting of the spectrometer can then be adjusted by a compensatory amount (usually by about 0.1 to 0.2 °C)

4. A critical parameter when performing CPMG relaxation dispersion experiments is the length of the constant relaxation delay, T_{relax}. Longer values of T_{relax} allow more time for exchange broadening to occur, whereas shorter values lead to less signal loss overall and more intense peaks. Therefore a compromise must be reached between maximizing the sensitivity to R_{ex} and optimizing signal strength. We find that a good balance is achieved when the spectrum obtained with the maximum ν_{CPMG} is about half as intense as that obtained with T_{relax}=0. This corresponds to an optimal value of $T_{relax} \approx \ln\{2\}/\boldsymbol{R_2^0}$ (e.g., 40 ms for $\boldsymbol{R_2^0}$ = 17 s^{-1}). One caveat to this rule is that T_{relax} periods longer than 40ms are generally not used, in order to limit amplifier loads, even when $\boldsymbol{R_2^0}$ values are small.

5. Alternatively, R_2 values can be measured separately for the ligand-free and ligand-saturated forms of the protein and then held fixed in analyses of CPMG data.

6. Some NMR cold-probes exhibit RF pulse-dependent artifacts, such that the sensitivity decreases (and apparent R_2 increases) with increasing ν_{CPMG}. In the case of Varian cold probes, it has been found that this can be suppressed by applying CW irradiation to ^{15}N nuclei prior to each transient for a variable time period, T_{CW}, given by

$$(T_{CW})_i = \frac{(\upsilon_{CPMG})_{\max} - (\upsilon_{CPMG})_i}{(\upsilon_{CPMG})_{\max}} T_{relax}$$

where $(\nu_{CPMG})_{max}$ is the largest value of ν_{CPMG} employed in a dispersion series, typically 1000 Hz (66). A compensation power level 8 dB below that of the CPMG pulse train typically provides excellent artifact suppression at all fields and temperatures.

7. In the case of two-state exchange, $\Delta\omega^2$ values obtained from titration experiments (i.e. squared maximum peak displacements) should equal $\Delta\omega^2$ parameters extracted from CPMG data using Equation 2.2.18, and should correlate linearly Φ_{ex} values obtained using Equation 2.2.19 (66). If Φ_{ex} values for all residues are plotted as function of titration-derived $\Delta\omega^2$ values, the slope is equal to $f_P f_{PL} = (1-f_{PL})f_{PL}$. If these correlations are not observed experimentally, it may be taken as evidence for the existence of additional millisecond-timescale exchange phenomena, i.e. dynamics involving more than two states. In this case,

multi-state binding parameters can be extracted by simultaneously fitting CPMG data obtained with different levels of ligand saturation (59).

2.5.3. EXSY experiments

8. EXSY experiments provide a convenient means for transferring spectral assignments from the free to the bound protein NMR spectrum, for systems that are in slow exchange. When association/dissociation kinetics are rapid, transferring assignments is a trivial process, since each peak gradually moves from the ligand-free frequencies to the ligand-saturated frequencies over the course of the titration. In contrast, for a slowly-exchanging system, it can be challenging to associate each gradually appearing peak with its corresponding disappearing peak in the titration data. The locations of exchange cross-peaks in EXSY spectra for a partially-saturated protein sample, thus, identify pairs of self peaks that are produced by the same amide group in the free and bound states (3).

3. Electrostatic interactions in the binding pathway of a transient protein complex studied by NMR and isothermal titration calorimetry

I have coauthored this article with:

Anthony Mittermaier

This article was published in:

Meneses, E., and Mittermaier, A. Electrostatic interactions in the binding pathway of a transient protein complex studied by NMR and isothermal titration calorimetry. J. Biol. Chem. 2014 289: 27911-27923. First Published on August 13, 2014.

Keywords: Protein dynamics; Src Homology 3 (SH3) domain; Nuclear Magnetic Resonance (NMR); Isothermal Titration Calorimetry (ITC); Carr–Purcell–Meiboom–Gill (CPMG) relaxation dispersion

Background: Electrostatic interactions are known accelerate binding in protein complexes with long lifetimes (min-hr).
Results: NMR and calorimetry were used to characterize binding kinetics in short-lived (≈ms) protein-peptide complexes.
Conclusion: Electrostatic enhancement is much less and basal (electrostatic-free) association rates are greater than previously observed.
Significance: Electrostatics may play different roles in short-lived and long-lived protein complexes.

3.1. Abstract

Much of our knowledge of protein binding pathways is derived from extremely stable complexes that interact very tightly, with lifetimes of hours to days. Much less is known about weaker interactions and transient complexes, since these are challenging to characterize experimentally. Nevertheless, these types of interactions are ubiquitous in living systems. The combination of NMR relaxation dispersion CPMG experiments and isothermal titration calorimetry allows the quantification of rapid binding kinetics for complexes with sub-millisecond lifetimes that are difficult to study using conventional techniques. We have used this approach to investigate the binding pathway of the Src Homology 3 (SH3)

domain from the Fyn tyrosine kinase, which forms complexes with peptide targets whose lifetimes are on the order of about a millisecond. Long-range electrostatic interactions have been shown to play a critical role in the binding pathways of tightly-binding complexes. The role of electrostatics in the binding pathways of transient complexes is less well understood. Similarly to previously-studied tight complexes, we find that SH3 domain association rates are enhanced by long-range electrostatics, while short-range interactions are formed late in the docking process. However, the extent of electrostatic association rate enhancement is several orders of magnitudes less, while the electrostatic-free basal association rate is significantly greater. Thus the SH3 domain is far less reliant on electrostatic enhancement to achieve rapid association kinetics than are previously studied systems. This suggests there may be overall differences in the role played by electrostatics in the binding pathways of extremely stable versus transient complexes.

3.2. Introduction

Many biological processes rely on the rapid formation of protein-ligand complexes (120-124). Consequently there has been great interest in elucidating the mechanisms through which binding partners are able to efficiently recognize each other in solution and adopt the correct conformations, relative positions and orientations to form native stereo-specific complexes. This has been addressed theoretically (16,125), by computer simulation (126,127), and experimentally (120,124,128,129). The association process is typically broken down into at least two steps. In the first step, the binding partners encounter each other through a random collision. For the small fraction of collisions in which the binding surfaces are correctly aligned (as few as 1 in 10^5), the molecules proceed to the second step and dock to form the native stereo-specific complex (20). If the docking step occurs much more rapidly than the timescale of productive intermolecular collisions, the reaction is said to be “diffusion-controlled” and the association rate is viscosity-dependent (16). When binding is diffusion-controlled, the protein and ligand pass through a free energy maximum en route to the bound state in which translational-rotational entropy is reduced with little compensation from favorable interactions (20,130). The ensemble of conformations at this free energy maximum has been referred to as an "encounter complex" (16), "transient complex" (131), or "transition state" (132). We shall use the term “transition state” throughout. For these systems, binding is essentially two-state, such that significant populations are observed only for the free and/or bound states, and a negligible fraction of molecules populate the high-energy transition state at any one time. Note that the two-state diffusion-controlled binding mechanism is compatible with conformational changes occurring after the transition state, provided that they proceed sufficiently rapidly (133). Additionally, transient conformational reorganization can occur prior to the intermolecular collision, leading to a “gated” diffusion-controlled binding mechanism (134). In either case, the structure of the transition state is key to understanding the binding pathway, as it represents a kinetic bottleneck. Interactions that stabilize the transition state accelerate molecular association rates (16,131,132).

A variety of interactions have been proposed to contribute to the stability of transition states, including non-specific hydrogen bonding, van der Waals interactions, non-polar desolvation (desolvation of non-polar residues), long-range electrostatic interactions, (16,135-137) or subsets of native bound-like interactions (138). The role of electrostatics in binding pathways has been particularly well studied. For a number of systems including barnase/barstar (124), E9/Im9 (128), IL4/IL4BP (129), and Fas/AchE (120), it has been found that electrostatic stabilization of weakly-specific transition states can accelerate association by up to 4 or more orders of magnitude, compared to the basal rate (132). A combination of experimental and computational studies has led to a picture of the transition state in which the binding partners remain solvent separated and interact almost exclusively by long-range electrostatics (132,139).

However, these investigations have focused on extremely tight protein/ligand interactions, as listed in Table 3.1.

Table 3.1. Electrostatic enhancement of protein association rates

	MW (Da)	Net charge	K_A (M^{-1})	k_{off} (s^{-1})	Basal k_{on} M^{-1} S^{-1}	Enhancement
Fyn SH3 domain	6979	-8				
RR peptide	1444	+2	51.7×10^{5} [a]	235 [a]	6.57×10^{7}	23.1
SR peptide	1375	+1	6.31×10^{5} [a]	378 [a]	5.94×10^{7}	4.42
SS peptide	1306	0	2.71×10^{3} [a]	1829 [a]	5.71×10^{7}	-
Barnase (140)	12382	+2				
Barstar	10342	-6	7.5×10^{13} [b]	8×10^{-6} [b]	3.98×10^{6}	1.92×10^{3}
Shaker K+ channel (141)	74193	-13				
Peptide toxin Lq2	4360	+5	3.0×10^{9} [b]	0.19 [b]	3.66×10^{5}	6.40×10^{4}
E9 DNase (142)	61587	+4				
Immunity protein Im9	9582	-9	1.4×10^{16} [b]	0.41×10^{-6} [b]	1.25×10^{6}	4.50×10^{5}
Heterodimeric leucine zipper (143)						
Acidic chain	1864	-4	1.9×10^{11} [c]	0.38×10^{-3} [c]	5.88×10^{5}	4.50×10^{3}
Basic chain	3402	+9				
Acetylcholinesterase (120)	68168	-9				
Fasciculin	6757	+4	1.3×10^{13} [b]	1.0×10^{-4} [b]	1.97×10^{5}	8.81×10^{3}

Measurements obtained at the I(mM) values: [a] 2, [b] 25, [c]74

Equilibrium association constants have ranged from 10^{9} to 10^{13} M^{-1} (K_D = nM to pM), with dissociation rates of 10^{-1} to 10^{-6} s^{-1} (lifetimes of seconds to days) Much less is known about the binding pathways of weaker complexes with lifetimes on the order of milliseconds. These types of short-lived protein interactions are abundant in nature, raising the important question: to what extent do long-lived and short-lived complexes follow similar binding pathways? In what follows, we will use “long-lived” to refer to complexes that bind with <nM K_D and have lifetimes on the order of minutes or longer. We will use “short-lived” to refer to complexes with ≥μM K_D and lifetimes on the order of milliseconds. Several studies of short-lived complexes have derived structural models of transient complexes that precede formation of the fully-bound state (59,144,145). However these investigations did not extract kinetic parameters nor identify the interactions governing association rates, which is key to understanding binding pathways.

The binding kinetics of short-lived complexes are challenging to measure experimentally. In typical stop-flow binding measurements, the protein and ligand are rapidly mixed and the extent of the reaction is monitored as a function of time using techniques including spectroscopic absorbance (138), fluorescence (128,140,146), enzymatic activity (120,147,148) and surface plasmon resonance (149,150). These techniques are limited by the requirement that the lifetimes of the free and bound states must be several-fold longer than the time required to completely mix the protein and ligand solutions, otherwise the reaction proceeds nearly to completion before the start of the measurement period.

The combination of Nuclear Magnetic Resonance (NMR) spectroscopy and Isothermal Titration Calorimetry (151) can characterize binding kinetics that are too rapid for standard stop-flow techniques, on the order of 10^4 s^{-1} (152). In this approach, a sub-stoichiometric amount of ligand is added to a protein sample whose signals are monitored by NMR spectroscopy. The resulting dynamical exchange between the free and bound states modulates the chemical shifts of nuclei in the protein on the ms to μs timescale, leading to signal broadening. The broadening is quantified by NMR relaxation dispersion experiments (153-155) which yield the dissociation rate constant, k_{off}. The equilibrium association constant of the interaction, K_A, is determined by ITC or NMR titration experiments. The second-order association rate constant is then given by $k_{on} = K_A \cdot k_{off}$. These two parameters report on the binding pathway as K_A is related to the free energy difference between the free and bound states while kon is related to the free energy difference between the free state and the transition state.

SH3 domains are typical of weakly-binding proteins that form short-lived complexes. These ~60 amino acid modules are found in the context of larger multi-domain proteins and mediate protein/protein interactions in signal transduction pathways (156,157). The type I ligand recognized by many SH3 domains comprises a short peptide sequence: +xΦPxΦP where P is proline, Φ is a hydrophobic amino acid, x is any amino acid, and + is a positively-charged residue, typically arginine or lysine (157). The positions in the motif are numbered -3 to 3 such that the conserved + occupies site –3. Dissociation constants for SH3 domains are usually on the order of μM and the lifetimes of their complexes are on the order of ms (152,158). We previously used NMR and ITC to study the binding kinetics of the SH3 domain from the Fyn tyrosine kinase. We showed that this protein binds a type I target peptide in a two-state manner with ms-timescale kinetics and a temperature dependence of kon that is consistent with diffusion-limited association (152). In the current study, we have focused on how positively charged residues within the SH3 binding motif and negatively-charged residues in the binding site on the SH3 domain interact to influence association kinetics. Three different dodecapeptides were employed: one with a typical type I consensus motif with the conserved R_{-3} preceded by S_{-4} (SR, net charge +1), a second containing $R_{-4}R_{-3}$ (RR, net charge +2), and a third containing $S_{-4}S_{-3}$ (SS, net charge 0). We analyzed the contributions of the conserved R_{-3} and “extra” R_{-4} residues to the stabilities of the fully-bound and transition states by comparing the binding affinities and association rates of the RR, SR, and SS peptides. Data were extrapolated to both zero ionic strength, where long-range electrostatic interactions are maximal, and to infinite ionic strength, where long-range electrostatics are fully attenuated. We find that the conserved R_{-3} and the “extra” R_{-4} residues stabilize both the encounter and fully-bound complexes via similar long-range electrostatic interactions, which implies that the Fyn SH3 domain and peptide are fairly close in the transition state. Notably, R_{-3} additionally stabilizes the bound state via short-range interactions that are not screened by adding salt. Likely candidates include a network of salt-bridges and hydrogen bonds previously observed for this residue in the bound complex by NMR (159) and X-ray crystallography (PDB 4EIK). These short range interactions involving R_{-3} are not present in the transition state and are only made after the molecules have crossed the free energy barrier, near the end of the binding pathway. Thus the SH3/peptide transition state is fairly compact and stabilized primarily by long-range electrostatic interactions, as seen for other protein/ligand systems (124,131,132,139). However, there are surprising differences between the system studied here and the high-affinity long-lived complexes investigated previously. We find that the electrostatic-free basal association rate for this system is significantly greater while the electrostatic association rate enhancement is several orders of magnitude less. This result suggests that short-lived complexes may rely less on electrostatic enhancement to achieve rapid binding than do high affinity long-lived complexes.

3.3. Materials and methods

Protein and peptide preparation - Wild-type chicken Fyn SH3 domain (residues 81 to 148) was expressed and purified as described previously (160). RR (Ac-WSLA$R_{-4}R_{-3}P_{-2}L_{-1}P_0P_1L_2P_3$-NH2), SR (Ac-WSLA$S_{-4}R_{-3}P_{-2}L_{-1}P_0P_1L_2P_3$-NH2)) and SS (Ac-WSLA$S_{-4}S_{-3}P_{-2}L_{-1}P_0P_1L_2P_3$-NH2) peptides were purchased from the Sheldon Biotechnology Centre (McGill, Montreal), and purified to homogeneity by reverse-phase HPLC. Protein and peptide samples were dialyzed against 5 mM MES pH 6.0 at the desired NaCl concentration. For ionic strength calculations, it was assumed that the buffer contributed 2.57 mM charged ions. Most experiments were performed at 40°C. This temperature was chosen to optimize the NMR CPMG relaxation dispersion profiles obtained with the RR and SR peptides, and lies within the physiological temperature range of 40-42 °C (161).

3.3.1. ITC

Titrations were performed at 40ºC using a VP-ITC instrument (MicroCal LLC, Northampton, MA). Measurements were taken in triplicate for each NaCl concentration and consisted of 56 injections of 5 µL. RR peptide data were collected at 0.00, 0.01 0.03, 0.05, 0.10, 0.20, 0.30, 0.40, 0.50, 1.00, 1.50, and 2.00 M NaCl. For the SR and the SS peptide measurements were taken at 0.00, 0.03, 0.20 and 0.30 M NaCl.Titrations were repeated for the SS peptide at 20 °C.

Data were fitted using the one-set-of-independent-sites model in the Origin Software package (OriginLab, Northampton, MA) and in-house MATLAB scripts (MATLAB R2013a, The MathWorks, Natick, MA).

3.3.2. NMR

^{1}H-^{15}N HSQC titration spectra, referenced to an internal DSS standard (162), were collected at 40 °C and 800 MHz for samples containing approximately 0.3 mM protein and 16 different peptide concentrations. In the case of the SS peptide titration, chemical shift peak trajectories were fit globally according to (10):

$$\delta = \delta_{free} + \tfrac{1}{2}\left(\delta_{bound} - \delta_{free}\right)\left(b - \sqrt{b^2 - 4R}\right) \tag{3.1}$$

where $\delta_{free,bound}$ are the chemical shifts of the free and bound protein, $R=[\text{peptide}]_{total}/[\text{protein}]_{total}$, and $b=1+R+(K_A \times [\text{protein}]_{total})^{-1}$.

^{1}H-decoupled ^{15}N CPMG experiments (155) with power compensation schemes (152) were performed at 40°C and 500 and 800 MHz on 1 mM samples of the Fyn SH3 domain, free in solution (0M NaCl), in the presence of 0.1 mM SS, SR, and RR peptides (0, 0.2, 0.3 M NaCl) and with saturating amounts of the RR peptide (0 M NaCl). Measurements were repeated at 20 °C for the SH3 domain alone (0 M NaCl) and in the presence of 0.1 mM SS peptide (0, 0.2, 0.3 M NaCl). Experiments employed a constant relaxation delay, T_{relax}, of 40 ms and twenty-three values of $\nu_{CPMG} = 1/(2\tau_{CP})$ ranging from 25 to 1000 Hz, where τ_{CP} is the delay between consecutive pulses. Transverse relaxation rates, R_2, were calculated for each cross-peak signal at each ν_{CPMG} value according to:

$$R_2^{\exp}\left(\nu_{CPMG}\right) = -\frac{1}{T_{relax}} \ln\left\{\frac{I\left(\nu_{CPMG}\right)}{I_0}\right\} \tag{3.2}$$

where $I(\nu_{CPMG})$ is the peak intensity at a given value of ν_{CPMG} and I_0 is the signal intensity with T_{relax}=0. The experimental uncertainties in peak intensities (σ_I) were considered to be the same for all values of ν_{CPMG} for a given residue at a given ionic strength and static magnetic field. CPMG experiments were repeated for a subset of ν_{CPMG} values (N_{dup} different values) with n_j replicates obtained at the jth repeated ν_{CPMG} value. The n_j replicates obtained at $(\nu_{CPMG})_j$ for a given residue, ionic strength, and static magnetic field yield a standard deviation s_j. The uncertainty in σ_I was calculated as:

$$\sigma_I^2 = \frac{\sum_{j=1}^{N_{dup}} s_j^2\left(n_j - 1\right)}{\sum_{j=1}^{N_{dup}}\left(n_j - 1\right)} \tag{3.3}$$

and the associated errors in transverse relaxation rates, σ_{R2}, are given by:

$$\sigma_{R2}\left(\nu_{CPMG}\right) = \frac{\sigma_I I_0}{T_{relax} I\left(\nu_{CPMG}\right)} \tag{3.4}$$

CPMG data were fitted using a two-state model of conformational exchange:

$$P + L \underset{k_{off}}{\overset{k_{on}[L]}{\rightleftarrows}} PL \tag{3.5}$$

where P is the protein, L is the ligand, PL is the complex, k_{off} is the dissociation rate constant, k_{on} is the association rate constant, [L] is the concentration of free peptide, and the difference between the precession frequencies of an ^{15}N nucleus of the protein in the free and bound states is given by $\Delta\omega$. Dispersion profiles were fit to equations valid for the fast timescale regime (163) ($\Delta\omega$ << (koff + kon[L])) or all timescale regimes (164) based on the parameter $\alpha = \frac{dLn\{R_{ex}\}}{dLn\{B_0\}}$, where R_{ex} is the total exchange contribution to R_2 and B_0 is the static magnetic field (115). Profiles with α>1.5 were considered to be in the fast exchange regime and were analyzed according to (163):

$$R_2\left(\nu_{CPMG}\right) = R_2^0 + \frac{\Phi_{ex}}{k_{ex}}\left(1 - \frac{4\nu_{CPMG}}{k_{ex}}\tanh\left(\frac{k_{ex}}{4\nu_{CPMG}}\right)\right) \tag{3.6}$$

where pfree and pbound are the relative populations of free and bound protein (p_{free} + p_{bound} = 1) , k_{ex}= k_{off} + k_{on}[L], Φ_{ex}=$p_{free}p_{bound}\Delta\omega^2$, and R_2^0 is the population-weighted average (broadening-free) transverse relaxation rate, R_2^0=$p_{free}R_{2free}{}^0$ + $p_{bound}R_{2bound}{}^0$. All other dispersion profiles were analyzed according to (164):

$$R_2\left(\nu_{CPMG}\right) = \tfrac{1}{2}\left(R_{2free}^0 + R_{2bound}^0 + k_{ex} - 2\nu_{CPMG}\cosh^{-1}\left(D_+\cosh\left(\eta_+\right) - D_-\cosh\left(\eta_-\right)\right)\right)$$

$$D_\pm = \tfrac{1}{2}\left(\pm 1 + \frac{\psi + 2\Delta\omega^2}{\sqrt{\psi^2 + \xi^2}}\right) \tag{3.7}$$

$$\eta_{\pm} = \frac{\sqrt{2}}{4\nu_{CPMG}}\sqrt{\pm\psi + \sqrt{\psi^2 + \xi^2}}$$

$$\psi = \left(R^0_{2free} - R^0_{2bound} + p_{free}k_{ex} - p_{bound}k_{ex}\right)^2 - \Delta\omega^2 + 4p_{free}p_{bound}k^2_{ex}$$

$$\xi = 2\Delta\omega\left(R^0_{2free} - R^0_{2bound} + p_{bound}k_{ex} - p_{free}k_{ex}\right)$$

We performed the analysis assuming that $R_{2free}{}^0 = R_{2bound}{}^0$. This is typically done in analyses of CPMG data, since it is not possible to reliably extract separate values for $R_{2free}{}^0$ and $R_{2bound}{}^0$ (165). In this case, the approximation is likely valid, as binding of the peptide is unlikely to substantially alter ^{15}N transverse relaxation rates in the protein.

In the case of the RR and SR peptides at 40°C with 0, 0.2, and 0.3 M NaCl, the datasets contained mixtures of dispersion profiles in the fast and intermediate time regimes, and data for all residues of a given sample were fitted simultaneously to extract global values of pbound and kex, while $\Delta\omega^2$ or Φ_{ex}, R_2^0 (800 MHz), and R_2^0 (500 MHz) were obtained on a per-residue basis (12). For the SS peptide at 20°C with 0 and 0.2 M NaCl all but one of the dispersion profiles were in the fast time regime. In these cases, the value of pbound was calculated based on the total concentrations of protein and peptide and the ITC-derived binding constants and was held fixed in the CPMG fits. Global values of k_{ex} were extracted while $\Delta\omega^2$, R_2^0 (800 MHz), and R_2^0 (500 MHz) were obtained on a per-residue basis. Values of k_{off} were subsequently calculated as $(1-p_{bound})k_{ex}$. Errors in the extracted parameters were estimated using a Monte Carlo approach in which group fitting was performed on random subsets of the residues selected using a bootstrap procedure (166). Analyses were performed using scripts written in MATLAB (MALAB R2011b, The MathWorks, Natick, MA).

3.3.3. Electrostatic Enhancements

$Log_{10}(K_A)$ values for the SS peptide were fitted as a linear function of ionic strength. Interpolated values were used to calculate the affinity enhancements of the SR and RR peptides. The corresponding linear interpolation was also used to calculate kon enhancements. The ionic strength enhancements were plotted as a function of fion, Equation (3.8), setting r=4Å, which roughly corresponds to the size scale of a single Arg residue. The plot was not highly sensitive to the choice of r.

3.3.4. Stopped-flow binding kinetics

The kinetics of binding were characterized by rapidly mixing the SH3 domain and peptide and monitoring the progress of the reaction via intrinsic tryptophan fluorescence of the protein, which increases upon interacting with proline-rich peptides (167). We used a version of the RR peptide free of Trp and Tyr fluorophores (VSLARRPLPPLP), thus the signal derives entirely from protein residues. We fit the binding data according to the following equations:

$$I(t) = \frac{[P](t)}{[P]_{total}} I_P + \frac{[PL](t)}{[P]_{total}} I_{PL} \quad , \tag{3.8}$$

where I(t) is the fluorescence signal at time t, [P](t) and [PL](t) are the concentrations of free protein and bound complex at time t, $[P]_{total}$=[P]+[PL] is the total concentration of protein, and I_P and I_{PL} are the fluorescence intensities of the free and bound states. The time dependence of [P](t) is given by (168):

$$[P](t) = \frac{K_D\left(\alpha\left(1+e^{C+\alpha k_{off} t}\right) - e^{C+\alpha k_{off} t} + 1\right)}{2\left(e^{C+\alpha k_{off} t} - 1\right)} \tag{3.9}$$

where

$\alpha = \sqrt{1+4[P]_{total} K_D^{-1}}$, $C = \ln\left\{\frac{2[P]_0 + K_D(1+\alpha)}{2[P]_0 + K_D(1-\alpha)}\right\}$, k_{off} is the dissociation rate constant, K_D is the equilibrium dissociation constant, and $[P]_0$ is the initial concentration of free protein at t=0, which is assumed to be equal to the initial concentration of free ligand, $[L]_0$=$[P]_0$. Data were analyzed by non-linear least-squares fitting with the values of $[P]_{total}$ and K_D held constant, while the values of I_P, I_{PL}, k_{off} and $[P]_0$ were varied to minimize the function:

$$SS = \sum\left(I(t)_{calculated} - I(t)_{measured}\right)^2 \tag{3.10}$$

where $I(t)_{calculated}$ is given by Equation (3.1) and the sum runs over all data points. The value of $[P]_{total}$ was obtained from the absorbance of the protein sample at 280 nm (169), the concentration of the peptide was determined by amino acid analysis (170), and the value of K_D was extrapolated from temperature-dependent ITC data for the Fyn SH3/RR peptide interaction (see below). Adjusting the value of $[P]_0$ accounts for binding that occurs during the dead time of the instrument (approximately 4 ms). The uncertainty in koff was obtained by fitting random sets of the 100 individual stop-flow traces selected according to the bootstrap method (166) and averaged. The error was taken as the standard deviation obtained after of 100 iterations.

Experiments were performed using a Bio-Logic SFM 400 instrument coupled to a MOS-250 spectrometer using Biokine 2.5 software for data acquisition. Intrinsic tryptophan fluorescence of the Fyn SH3 domain was measured with an excitation wavelength of 276 nm and a bandwidth of 20 nm. Emission at a wavelength of 320 nm and a bandwidth of 10 nm was recorded for 150 milliseconds (ms) with measurements taken every 0.02 ms. The detector photomultiplier was operated at 860 Volts. For each trace, 201 uL of protein (1 uM) and 201 uL of RR peptide (1uM) were mixed for a total injection volume of 402 uL at a flow of 13.5 mL s^{-1}, at 5°C.

3.3.5. NMR-derived binding kinetics

We previously characterized the binding kinetics of the RR peptide using NMR and ITC over a temperature range of 10 to 50°C (152). In this prior work, we employed both CPMG and ZZ magnetization exchange NMR experiments (EXSY) at 20°C, obtaining very similar values for koff: 11.2 s^{-1} and 12.8 s^{-1}, respectively. At 10°C, only ZZ exchange experiments were used, yielding koff=4.5 s^{-1}. CPMG experiments were not performed as spectral broadening is minimal at this temperature. We extrapolated the expected kinetic and thermodynamic behaviour to 5°C according to:

$$K_D = \exp\left\{\frac{-\Delta H + T\Delta S}{RT}\right\}, \qquad (3.11)$$

$$\Delta H = \Delta H_0 + \Delta C_p\left(T - T_0\right),$$

$$\Delta S = \Delta S_0 + \Delta C_p \ln\left\{\frac{T}{T_0}\right\},$$

where T_0 = 303.15 K, ΔH_0 = 15.4 kcal mol^{-1}, ΔS_0 = 20 cal mol^{-1} K^{-1}, ΔCp = 352 cal mol^{-1} K^{-1} (152), T = 278.15 K, R is the universal gas constant and,

$$\mathrm{k_{off}}(5°\mathrm{C}) = \left(\left(\frac{278.15\mathrm{K}}{283.15\mathrm{K}}\right)\exp\left\{\frac{\mathrm{E_a}}{\mathrm{R}}\left(\frac{1}{283.15\mathrm{K}} - \frac{1}{278.15\mathrm{K}}\right)\right\}\mathrm{k_{on}}(10°\mathrm{C})\right)\mathrm{K_D}(5°\mathrm{C}) \qquad (3.12)$$

where k_{on}(10°C) = 1.03 ± 0.05 x 10^8 M^{-1} s^{-1} (152) and E_a = 3.4 ± 0.5 kcal mol^{-1}. This yielded K_D(5°C) = 36.7 nM and k_{off}^{NMR}(5°C) = 3.3 ± 0.2 s^{-1}. For the sake of comparison, K_D(10°C) = 46.1 nM.

3.4 Results and discussion

3.4.1. NMR titration experiments

Series of protein ^{1}H-^{15}N correlation HSQC NMR spectra were collected for the Fyn SH3 domain titrated with RR, SR, and SS peptides (Figure 3.1) at 40°C.

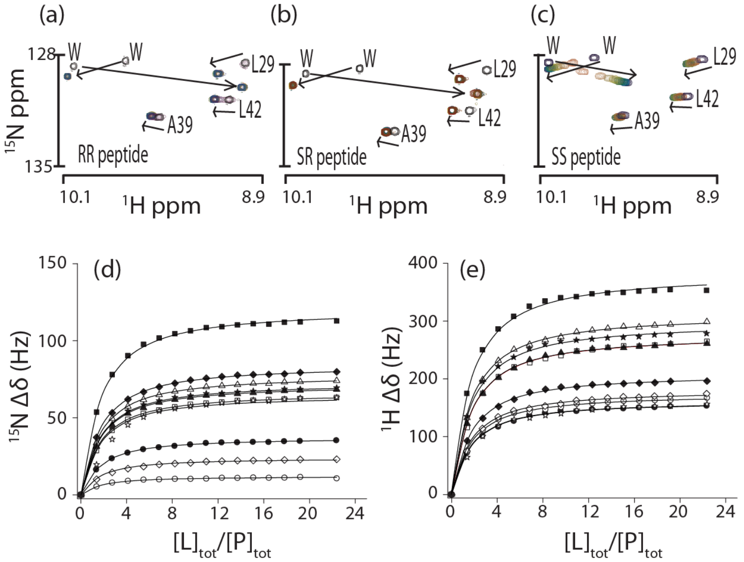

Figure 3.1. Regions of ^{15}N/^{1}H HSQC spectra of the Fyn SH3 domain titrated with (a) RR (b) SR and (c) SS peptides. Chemical shift displacements of SH3 domain signals in the ^{15}N (d) and ^{1}H (e) dimensions upon titration with the SS peptide. Curves represent the global fit to a two-state binding equation. Different curves correspond to different NMR peaks.

Exchange between the free and bound states was intermediate on the NMR chemical time scale (115) for the RR and SR peptides and fast for the SS peptide. The signals for many of the same protein residues were displaced by the addition of each peptide (Figure 3.1a-c). This suggests that all three peptides occupy the same binding site, consistent with the idea that the ΦPxΦP motif is the minimal recognition sequence of the SH3 domain (156). The chemical shift displacements are colour-coded on a structure of an SH3/peptide complex in Figure 3.2.

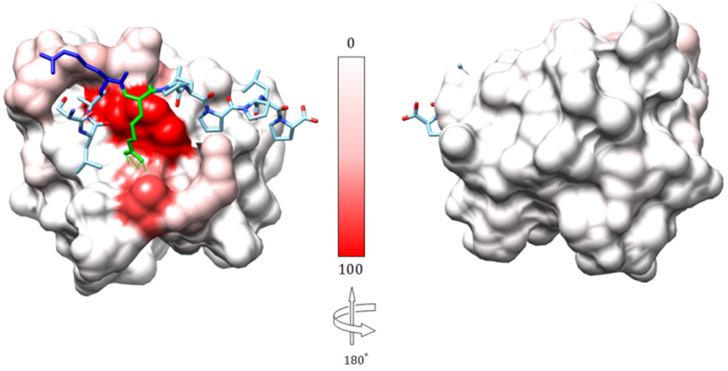

Figure 3.2. Structure of the Fyn SH3 domain in complex with a ligand identical to the RR peptide but containing Val rather than Trp at position -8, PDB 4EIK. Relative $^{15}N/^{1}H$ chemical shift perturbations ($\Delta\delta^2= (10\Delta\delta_{1H})^2 + (\Delta\delta_{15N})^2$), normalized to the largest perturbation, ($\Delta\delta$=12.98 ppm) colour-coded on the protein surface, from 0% (white) to 100% (red). Peptide residues R_{-3} (green) and R_{-4} (blue) are illustrated in ball and stick format. Hydrogen bonds between R_{-3} in the peptide and D17 in the Fyn SH3 domain are indicated by green lines.

SS peptide titrations were repeated in the presence of 0, 0.2, and 0.3 M NaCl at 40°C. Peak displacements (Figure 3.1d,e) were analyzed to extract the equilibrium association constants, K_A, yielding values in good agreement with the ITC-derived measurements (Table 3.2).

Table 3.2. Thermodynamic and kinetic binding parameters for the Fyn SH3 domain

RR peptide					
[NaCl] (M)	**K_A ($\times 10^5$ M^{-1})**	**k_{off} (s^{-1})**	**k_{on} ($\times 10^8$ M^{-1} s^{-1})**	**P_b ($\times$ 10^{-2}) *(CPMG)*[a]**	**P_b($\times$10^{-2}) (K_A)[b]**
0.0000	51.7 ± 2.7	235 ± 12.1	12.2 ± 0.9	7.3 ± 0.3	7.1
0.0080	25.6 ± 1.5				
0.0330	14.6 ± 0.3	267 ± 83.5	3.89 ± 0.01	7.4 ± 0.3	7.1
0.0500	10.3 ± 1.0				
0.1000	7.47 ± 0.2				
0.2000	5.21 ± 0.2	357 ± 13.0	1.86 ± 0.1	7.1 ± 0.2	7.2
0.3000	5.11 ± 0.2	354 ± 1.34	1.81 ± 0.1	7.3 ± 0.4	7.2
0.4000	4.50 ± 0.1				
0.5000	4.56 ± 0.2				
1.0000	5.19 ± 0.2				
1.5000	5.72 ± 0.5				
2.0000	8.68 ± 0.2				
RR peptide (15% Glycerol)					
0.0000	20.5 ± 0.5	280 ± 10 .3	5.74 ± 0.5	6.58 ± 0.3	7.1
SR peptide					
0.0000	6.31 ± 0.2	378 ± 0.3	2.39 ± 0.01	8.04 ± 0.01	7.2
0.0330	3.54 + 0.1	387 ± 0.6	1.37 ± 0.01	8.96 ± 0.1	7.2
0.2000	2.28 ± 0.23	500 ± 0.8	1.14 ± 0.1	8.21 ± 0.2	7.2
0.3000	2.33 ± 0.1	428 ± 0.6	0.99 ±0.01	7.72 ± 0.1	7.2
0.5000	2.39 ± 0.15				
1.0000	3.38± 0.1				
2.0000	6.91± 0.1				
SS peptide					
[NaCl] (M)	**K_A ($\times$ 10^3 M^{-1})**	**k_{off} (s^{-1})**	**k_{on} ($\times 10^6$ M^{-1} s^{-1})**		
0.0000	2.71 ± 0.2	1829 ± 127	5.09 ± 0.3		
0.2000	4.84 ± 0.1	2440 ± 239	11.8 ± 1.2		
0.3000	6.79 ± 0.1	2050 ± 239	10.9 ± 1.5		
0.5000	5.21 ± 0.1				
1.0000	9.72 ± 5.2				
2.0000	23.2 ± 4.5				
SS peptide (20°C)					
0.0000	7.87 ± 0.5	3505 ± 180	2.75 ± 0.2		
0.2000	12.10 ± 0.04	2376 ± 287	2.88 ± 0.3		
0.3000	13.13 ± 0.04	2848 ± 250	3.74 ± 0.4		

population of the bound state [a] extracted from CPMG data and [b] calculated based on the ITC-derived affinity and concentrations of protein and peptide used.

A further SS peptide titration was performed at 20°C in the presence of 0 M NaCl. Under these conditions, exchange was on the intermediate timescale, however peak shifts were essentially identical to those obtained at 40°C.

3.4.2. Isothermal Titration Calorimetry

The affinities of the Fyn SH3 domain for the RR, SR, and SS peptides were characterized by ITC at 40 °C with NaCl concentrations ranging from 0 to 2M (Figure 3.3, Table 3.2), yielding equilibrium association constants, K_A, plotted in Figure 3.4.

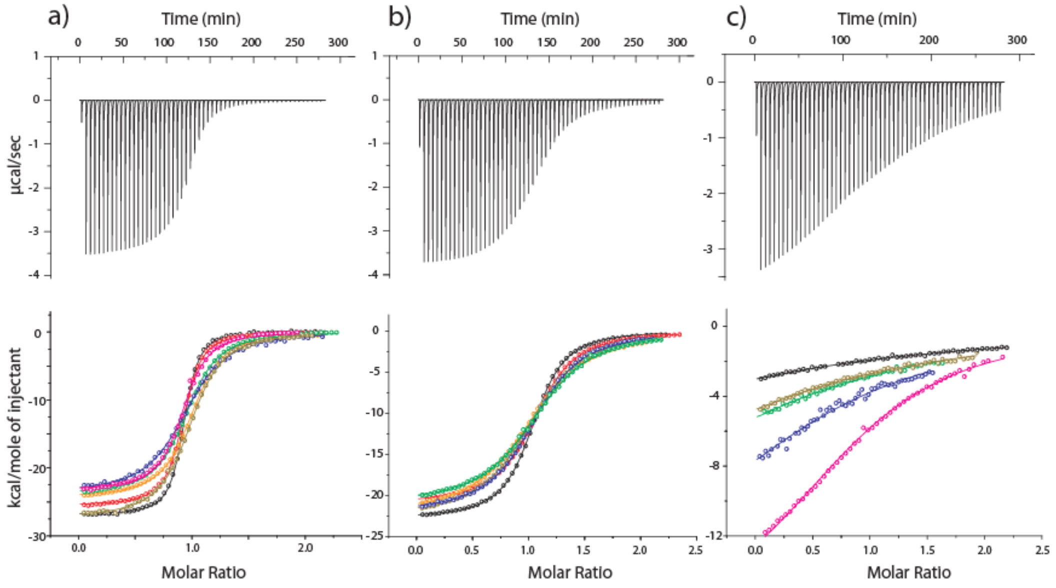

Figure 3.3. Isothermal Titration Calorimetry raw thermograms (upper) and integrated heats (lower) for RR (a), SR (b) and SS (c) peptides binding to the Fyn SH3 domain at 40°C and different ionic strength. Black (0 mM NaCl added), Red (33 mM), Orange (200 mM), Dark yellow (300 mM), Green (500 mM), Blue (1000 mM), Magenta (2000 mM). Raw thermograms were obtained with 0M added salt.

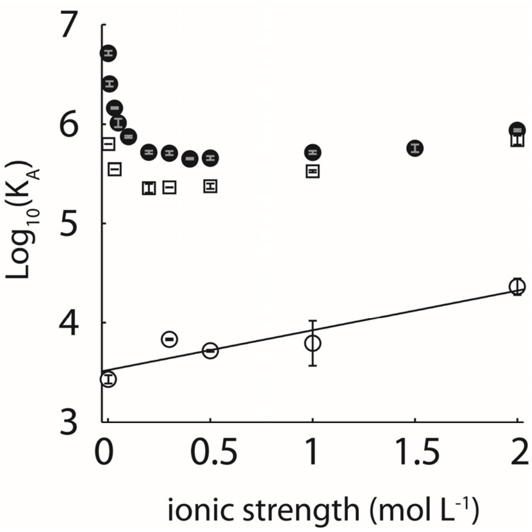

Figure 3.4. Base 10 logarithms of affinity constants, K_A, of the Fyn SH3 domain for RR (filled circles), SR (open squares), and SS peptides (open circles) plotted as a function of ionic strength. In some cases the error bars are within the symbols used.

The affinity of the RR peptide shows a sharp decrease with increasing salt concentration up to about 0.25 M NaCl, followed by a gradual increase. The affinity of the SR peptide also decreases sharply up to 0.25 M NaCl. This is similar to the salt dependence of protein solubility, which typically shows an initial increase or “salting in” as electrostatic interactions are screened, followed by a decrease or “salting out” as hydrophobic interactions are enhanced by increasing salt concentration (171). The hydrophobic association of pairs of methane molecules in water and the chemical potential of methane dissolved in water both increase linearly with NaCl concentration (172,173). The affinity of the SS peptide is roughly three orders of magnitude weaker than those of the SR and RR peptides (at 0 M NaCl) and increases linearly with increasing salt concentration. This molecule is uncharged and its binding to the SH3 domain is driven by non-polar interactions involving the ΦPxΦP motif which are presumably enhanced by increasing salt concentrations. Thus the initial downward slope of the RR affinity profile is due to the screening of electrostatics, while the slight upward slope at high NaCl concentrations is caused by the enhancement of hydrophobic interactions involving the ΦPxΦP binding motif. As discussed below, an additional set of ITC experiments was performed for the SS peptide at 20ºC with 0, 0.2 and 0.3 M NaCl.

3.4.3. NMR kinetics experiments

The kinetics of peptide binding were characterized using NMR CPMG relaxation dispersion experiments performed on ^{15}N-enriched samples of the Fyn SH3 domain partially saturated with RR and SR peptides at 40ºC with NaCl concentrations of 0.00, 0.03, 0.20 and 0.30 M. Association/dissociation dynamics produce chemical shift fluctuations that contribute to ^{15}N transverse relaxation rates, R_2. CPMG experiments quench these contributions with variable trains of 180º refocusing radio-frequency pulses applied during a constant relaxation delay (153,154). Plots of R_2 versus ν_{CPMG} are shown in Figure 3.5, where $\nu_{CPMG}=1/(2\tau)$ and τ is the delay between successive refocusing pulses.

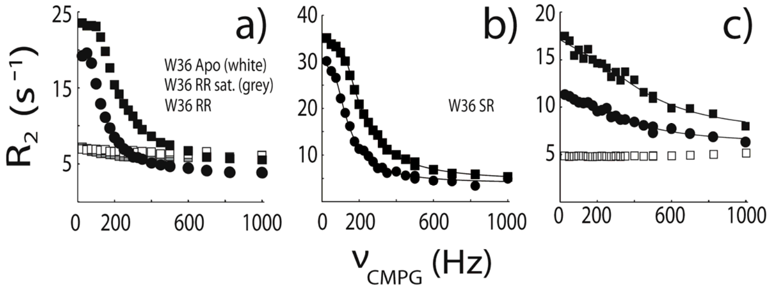

Figure 3.5. NMR ^{15}N CPMG relaxation dispersion data for the backbone amide signal of W36 collected at 500 (circles) and 800 (squares) MHz and 0M NaCl. In (a), white, grey and black symbols correspond to protein samples with RR-peptide:protein ratios of 0%, 300%, and ≈10% at 40°C. In (b), data were obtained with an SR-peptide:protein ratio of ≈10% at 40ºC. In (c), white and black symbols correspond to SS-peptide:protein ratios of 0% and ≈10% at 20°C. Lines indicate the global best fits as described in the Experimental section.

This spectral broadening reflects entirely exchange between the free and bound forms of the protein. Essentially flat dispersions are obtained for the protein in the absence of peptide, although the profiles of some residues in the free protein are very slightly sloped by 5×10^{-4} s^{-1} Hz^{-1}. This indicates that the large dispersions we observe are not due to internal dynamics of the protein itself, as these would be evident when peptide is absent. Flat dispersions are also obtained with saturating amounts of the RR peptide. The populations of all protein and peptide species are at thermodynamic equilibrium throughout the CPMG experiment.

Thus any partly-bound intermediate forms in the partially-saturated sample would be present in the fully-saturated sample as well. If the large dispersions were due to exchange between the bound state and an intermediate, they would also be observed for the fully saturated sample, which is not the case. Furthermore, chemical shift parameters extracted from the CPMG fits, $\Delta\omega^2$, provide a fingerprint of the exchanging species. In this case, we obtain quantitative agreement between $\Delta\omega^2$ and the peak displacements extracted from peptide titrations, $\Delta\delta^2$, as observed previously (152) (Figure 3.6).

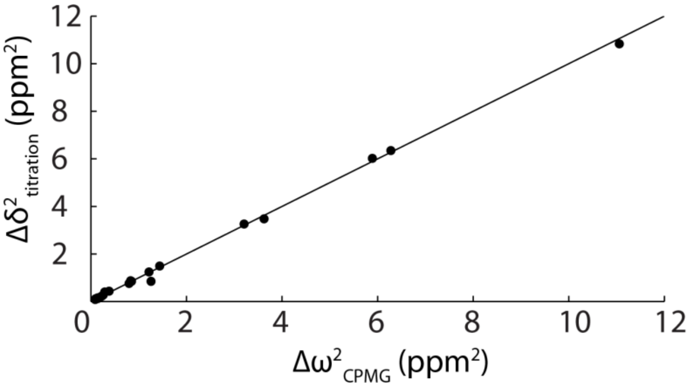

Figure 3.6. Comparison of $\Delta\omega^2$ ^{15}N chemical shift parameters extracted from CPMG relaxation dispersion NMR experiments performed on the Fyn SH3 domain partially-saturated with the RR peptide (0M NaCl) and $\Delta\delta^2$ peak displacements from a comparison of the Fyn SH3 domain spectra free and saturated with the RR peptide (0 M NaCl). The line goes through the origin with a slope of 1.

If the large dispersions were due to exchange between the free protein and a binding intermediate, such good agreement would not be expected, unless the intermediate had identical chemical shifts to the bound state, which is unlikely. Thus the relaxation dispersion analysis reports on the kinetics of exchange between the free and fully-bound states. Dissociation rate constants, k_{off}, were extracted from the data as described in the Experimental Section and used to calculate k_{on}, according to $k_{on} = K_A \cdot k_{off}$

Experiments with the RR peptide with 0.0 M NaCl were repeated in the presence of 15% glycerol, which translates into a 1.45-fold increase in solution viscosity, η (174). If binding rates are limited by diffusion in solution then k_{on} should be inversely proportional to η (16), although in practice the slope of a k_{on}/k_{on}^0 versus η^0/η plot can diverge somewhat from the theoretical value of 1 (175). We find that the peptide binds 2.13-fold more slowly in the presence of 15% glycerol, which lies well within the range of viscosity dependences reported for diffusion-limited protein association rates (175). We also find that the association rate constant is significantly (approx. 4-fold) more sensitive to ionic strength than the dissociation rate constant, which is a signature of diffusion-limited binding (130). In addition, we reported previously that the apparent activation enthalpy (E_a) for k_{on} is 3.4 kcal mol^{-1} (152). This matches the expected E_a=4.5 kcal mol^{-1} for diffusion limited reactions reflecting the temperature dependence of water viscosity (133). Taken together, the NMR kinetics data strongly indicate that peptide binding to the SH3 domain is a diffusion-limited, two-state process.

In the case of the SS peptide at 40 °C, exchange kinetics are extremely rapid, leading to very small and essentially linear dispersion profiles. Due to their very small magnitudes, they are partially obscured by the slightly sloped profiles obtained for the free protein (which likely reflect some degree of internal motions unrelated to peptide binding). Therefore in order to determine binding kinetics for the SS peptide, CPMG experiments were performed at 20ºC with 0, 0.2, and 0.3 M NaCl, conditions which produce large dispersions for the partially SS peptide-saturated protein sample, and completely horizontal dispersion profiles for the free protein, as shown in Figure 5. Values of k_{off} determined at 20ºC were combined with affinities, K_A, measured by ITC at 20ºC to yield association rate constants, k_{on}. We used the previously determined value of E_a=3.4 kcal mol^{-1} to extrapolate k_{on} for the SS peptide from 20 to 40°C according to: $k_{on}(T_2) \approx (T_2/T_1) \times k_{on}(T_1) \times \exp\{E_a/R\times(1/T_1 - 1/T_2)\}$ (176), where R is the gas constant. This leads to scaling of k_{on} by a factor of only 1.6, which is small compared to the up to 30-fold differences in k_{on} observed between the different peptides. Thus the results are not sensitive to the exact choice of E_a.

3.4.4. Comparison of NMR and stopped-flow binding kinetics

In order to cross-validate the NMR characterization of Fyn SH3 domain/peptide binding kinetics we performed a stopped-flow spectroscopic analysis of the same system. However the rates determined in the current study far exceed the limits of standard stopped-flow instruments (this is one of the advantages of the NMR-based approach). We therefore collected stopped-flow data at 5°C, in order to slow the kinetics sufficiently for them to be amenable to this type of analysis. Fluorescence traces for the SH3 domain injected with buffer (green) and a peptide solution (blue) are shown in Figure 3.7, with t=0 aligned to the end of the injection.

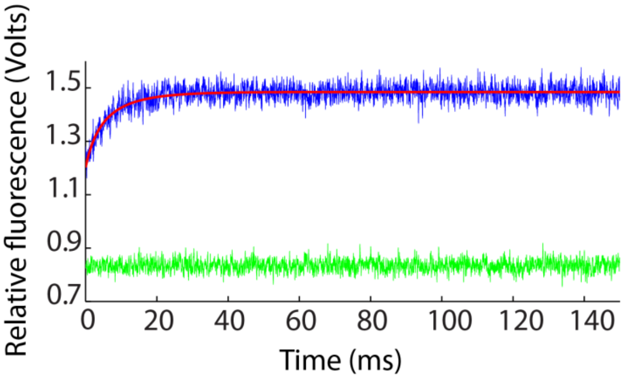

Figure 3.7. Stopped-flow fluorescence data for the Fyn SH3 domain rapidly mixed with buffer (green) and with a solution of the RR peptide (blue). Data shown are the averages of 100 individual stopped-flow traces. The best fit using Equation (8) is indicated with a red line.

As expected, the fluorescence signal for the protein/peptide pair shows a time-dependent increase after the injection due to evolution of the binding reaction. This signal is above that of the free protein at t=0 due to binding that occurs during the dead-time of the instrument, which is about 4 ms. Analysis of the stopped-flow data yields $k_{off}^{SF}(5°C)=8.9±0.6\ s^{-1}$ while the NMR kinetics method yields $k_{off}^{NMR}(5°C) = 3.3±0.2\ s^{-1}$, as described in the Methods section. These two values differ by about a factor of 3, which we believe is excellent agreement for such different experimental modalities. This gives us further confidence in the NMR-based kinetics method.

3.4.5. Electrostatic enhancement of association rates

We investigated the influence of electrostatics on SH3 domain ligand binding kinetics by varying the ionic strength of the samples, in order to attenuate long-range Coulombic interactions, and by comparing results for the RR, SR, and SS peptides, which carry formal charges of +2, +1, and 0. The screening of Coulombic interactions by electrolyte solutions was analyzed in terms of the electrostatic attraction of two oppositely-charged spheres with radii r, a centre-centre separation of $2r$, and charges $\pm Z$. Relative to infinite separation, the potential energy, V, is given by the expression (177,178):

$$V = -\frac{Z^2 e^2}{2r\varepsilon} \times f_{ion}, \qquad f_{ion} = \frac{\exp\{-\kappa r\}}{1+\kappa r}, \tag{3.13}$$

e is the elemental charge, ε is the dielectric constant of the medium, and κ is the inverse Debye length, $\kappa = \sqrt{\frac{4\pi e^2}{k_B T}}\sqrt{I}$, k_B is the Boltzmann constant and I is the ionic strength. The parameter f_{ion} describes the ionic strength dependence of the potential energy, with limiting values of 1 (full interaction strength) in the absence of salt, and 0 (zero interaction strength) at infinite salt concentration.

The logarithms of k_{on} are plotted as a function of f_{ion} for the RR, SR, and SS peptides in Figure 3.8a, together with linear regression lines.

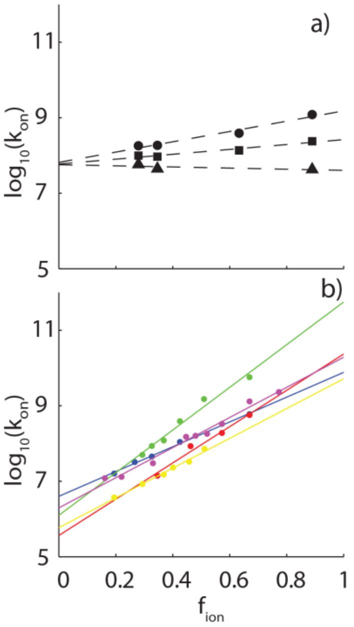

Figure 3.8. Ionic strength dependence of association rates. (a) NMR and ITC-derived association rate constants, k_{on}, for the RR (circles), SR (squares), SS (triangles) peptides binding to the Fyn SH3 domain, plotted as a function of f_{ion} (Equation (3.13)), which takes values between 1 at zero ionic strength and 0 at infinite ionic strength. Dashed lines are the linear regression fits of the data. (**b**) Association constants for barnase/barstar (blue), shaker K^+ channel/peptide toxin Lq2 (red), E9 DNase/immunity protein Im9 (green), heterodimeric leucine zipper (yellow), and acetylcholinesterase/fasciculin 2 (magenta) plotted as a function of f_{ion}.

Data for the RR and SR peptides have positive slopes, as expected, since larger values of f_{ion} correspond to lower salt concentrations, greater electrostatic stabilization of the transition state, and faster association. The data for the SS peptide are close to horizontal, as expected for an uncharged ligand. The slightly negative slope may be due to weak hydrophobic stabilization of the transition state that is enhanced at high salt concentrations. Notably, the lines for the three peptides nearly intersect at f_{ion}=0, and a k_{on} value of about 6×10^{7} M^{-1} s^{-1}. This corresponds to the basal, or electrostatic-free association rate. The close agreement of basal association rates obtained for the three different peptides gives us confidence in the reliability of the extrapolation along f_{ion}. The slopes of the lines correspond to the logarithms of the maximum electrostatic enhancement of binding with zero ionic strength, $\log(k_{on}^{enhanced}/k_{on}^{basal})$. We find that long-range Coulombic interactions accelerate binding of the RR and SR peptides by 23.1 and 4.42 fold, respectively, as listed in Table 3.1.

The basal association rate for the SH3 domain is significantly greater, and the extent of electrostatic enhancement is much less, than observed previously for long-lived complexes. Association rates for a dataset of five different systems (130) are plotted as a function of f_{ion} in 3.6b and the basal association rates and electrostatic enhancements extracted from the linear fits are listed in Table 3.1. These proteins bind roughly 10^{3} to 10^{10} fold more tightly and dissociate 10^{3} to 10^{9}

fold more slowly than the SH3 domain studied here. Notably, all of these basal, electrostatic association rates are 10 to 100 fold slower than those obtained for the SH3 domain, while the electrostatic rate enhancements are 10^2 to 10^4 fold greater.

It is likely that these differences are due to differences in the nature of the binding surfaces for the SH3 domain compared to the proteins in long-lived complex database. The barnase/barstar interface is fairly typical of those in the database in terms of size and complexity. It buries 1590 Å^2 of accessible surface area and involves the formation of 14 specific hydrogen bonds (179). In this case, only about 1 molecular collision in 1700 aligns the binding surfaces sufficiently accurately to proceed to the fully bound state in the absence of electrostatic enhancement, assuming no charged interactions and a molecular collision frequency of 6.6×10^9 M^{-1} s^{-1} (20). In contrast, the complex formed by the SH3 domain and ΦPxΦP motif buries only 600 Å^2 and is stabilized entirely by hydrophobic interactions (159). In this case about 1 in every 160 SH3/peptide collisions is sufficiently well aligned to progress to the bound state. Docking of the SS peptide onto the SH3 binding surface involves a significantly smaller contact area with fewer specific pair-wise interactions. This likely results in less stringent geometric requirements for molecular collisions to lead to successful docking of the SS peptide and a more rapid basal association rate.

A less geometrically restricted transition state could explain our observation of lower electrostatic enhancement of SH3/peptide association rates compared to that of barnase/barstar and other long-lived complexes. For barnase/barstar it was found that the transition state is stabilized by specific charged residues that are in close proximity in the stereospecific complex. This implies that these residues are correctly oriented with respect to one another at the rate-limiting step of binding (124). The SH3 domain exhibits a greater basal association rate, suggesting that the transition state is less geometrically constrained. Thus fewer specific interactions may be formed between charged residues in this state, leading to a smaller degree of electrostatic stabilization.

Thus the SH3 domain and target peptide do not rely as heavily upon electrostatic enhancement to achieve rapid association kinetics as do many previously-studied long-lived complexes. It has been previously noted that the interfaces of high-affinity complexes tend to contain more charged residues than those of low-affinity ones, and that these Coulombic interactions are sometimes, but not always, thermodynamically stabilizing (180). This is consistent with higher affinity complexes relying more heavily on electrostatic enhancement to achieve rapid binding kinetics than weaker complexes, however the question is far from resolved.

3.4.6. Arginine interactions in the transition state and bound state

In order to clarify the role played by the peptide arginine residues in the SH3 domain binding pathway, we compared K_A and k_{on} values for the RR and SR peptides to those of the SS peptide. The SS peptide carries no formal charges and binds in the same location as the SR and RR peptides, as evinced by similar patterns of peak movements in protein NMR titration experiments. The ratios of K_A and k_{on} obtained for the RR and SR peptides relative to those of the SS peptide describe the contributions of the conserved (R_{-3}) and "extra" (R_{-4}) Arg residues to the stabilities of the fully-bound and transition states. The logarithms of the RR/SS and SR/SS ratios are plotted as a function of f_{ion} in Figure 3.9, and exhibit excellent linear correlations over their full ranges of roughly two orders of magnitude.

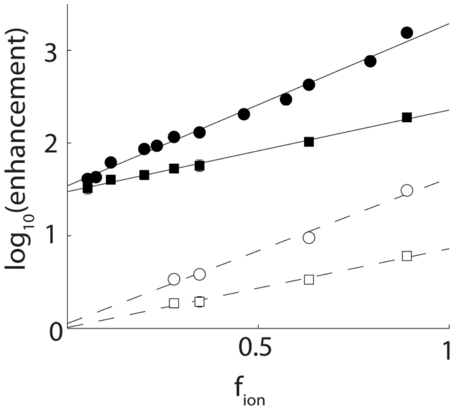

Figure 3.9. Enhancements in affinities ($K_A^{SR,RR}/K_A^{SS}$, solid lines, filled symbols) and association rates ($k_{on}^{SR,RR}/k_{on}^{SS}$, dashed lines, open symbols) for the RR (circles) and SR (squares) peptides relative to the SS peptide, plotted as a function of f_{ion}.

When extrapolated to infinite salt concentration at the *y*-intercept, the affinity of the SR peptide is still enhanced by a factor of 26, relative to the SS peptide, which translates into a stabilization of the bound state by 2.0 kcal mol^{-1}. This enhancement is due to interactions formed by R_{-3} that are not screened by salt and therefore almost certainly involve short-range forces. The slope for the RR peptide is greater than that of the SR peptide by about a factor of 2 in Figure 3.9, consistent with the two-fold difference in formal charge. However, when extrapolated to infinite salt concentration, the affinities of the two peptides are virtually identical, as evinced by the intersection of the two lines at the *y*-axis (solid lines Figure 3.7). Thus the "extra" R_{-4} forms long-range electrostatic interactions in the bound state but no energetically significant short-range (i.e. unscreened) interactions.

This is consistent with the X-ray crystal structure of the Fyn SH3 domain bound to a ligand very similar to the RR peptide used in this study ($W_{-8} \rightarrow V_{-8}$), shown in Figure 3.2 (159). The conserved R_{-3} forms a salt bridge (i.e. hydrogen bonds) with D17, while the aliphatic portion of the residue packs against W36. In contrast, the "extra" Arg, R_{-4}, points away from D17 and makes no additional hydrogen bonds. However, negatively-charged E33 and E34 are within about 6.5 Å, well-positioned to interact with R_{-4} electrostatically. Guanidinium ions, equivalent to the guanidino moiety of the Arg side-chain, interact with the Fyn

SH3 domain specifically at the peptide binding site and compete with the RR peptide (63). Together, these data strongly suggest that the guanidino moiety of R_{-3} interacts with Fyn SH3 domain via a network of hydrogen bonds while R_{-4} forms looser, long-range electrostatic interactions in the fully-bound complex. The pattern of enhancements seen for k_{on} is similar, but differs in an important respect. At 0 M NaCl, the RR peptide binds 5-fold more rapidly than the SR peptide, which binds 6-fold more rapidly than the SS peptide. This is consistent with both R_{-3} and R_{-4} forming long-range electrostatic interactions in the transition state. However, in the extrapolation to infinite salt concentration, both RR and SR peptides bind with rates that are nearly identical to the value determined for the SS peptide. All of the interactions formed by the peptide Arg residues in the transition state are thus electrostatic and long-range (i.e. are screened by salt). The short-range interactions involving R_{-3} that are present in the fully-bound complex are only formed after the protein/peptide pair have passed through the high-energy transition state, i.e. near the end of the binding process. The transition states of far more tightly-binding partners are believed to be similarly dominated by long-range electrostatic interactions and lacking in short-range contacts.(124,131,132,139)

3.4.7. Ionic strength dependence of dissociation rates

For diffusion-limited binding reactions, values of k_{on} are typically far more sensitive to ionic strength than are values of k_{off}.(120,128,140) In the case of the RR peptide, k_{on} is about 4 times more sensitive to ionic strength than k_{off}. This has been explained in terms of the structure of the transition state (130). Long-range electrostatic interactions are fairly insensitive to small changes in charge separation. Thus if the two binding partners remain close in the transition state, then long-range electrostatics contribute similarly to the stabilities of the fully-bound and transition states. Increasing the ionic strength screens the long-range charge interactions present in both states to equal extents. Thus the barrier to dissociation is not greatly affected and k_{off} is essentially unchanged. In contrast, destabilization of the transition state by added salt increases the barrier to association and slows binding rates.

However this explanation appears inconsistent with mutational analyses of charge interactions in the fully-bound and transition states. In the case of barnase/barstar, mutagenesis-derived coupling energies between charged residues in the fully bound state range from 1-7 kcal mol^{-1} (159) whereas coupling energies in the transition state are less than 0.5 kcal mol^{-1} (124). Similarly, the SS peptide binds 250-fold more weakly than the SR peptide but only 6-fold more slowly. The SS peptide binds 1900-fold more weakly and only

29-fold more slowly than the RR peptide in the absence of salt. These results indicate that the interactions of charged residues are much weaker in the transition state than in the fully-bound state. Adding salt should significantly destabilize the bound state without significantly affecting the transition state and thus should increase dissociation rates. Our results provide a simple explanation for this apparent contradiction. We directly measured electrostatic-free basal affinities and association rates for the SS peptide, which allowed us to separate the interaction energies of R_{-3} and R_{-4} into long-range “screenable” electrostatic and short-range “unscreenable” components. Notably, the long-range components are comparable for the fully-bound and transition states. For the SR compared to the SS peptide, long-range interactions enhance the affinity and association rate by factors of 9 and 6, respectively at 0 M NaCl, compared to 250- and 6-fold total enhancements. For the RR peptide, these long-range enhancement factors are 73 and 29, compared to 1900- and 29-fold total enhancements. Thus for the Fyn SH3 domain, long-range electrostatic interactions are similar in the fully-bound and transition states leading to k_{off} values that are relatively insensitive to ionic strength. This has the implication that the peptide and SH3 domain are separated by a relatively short distance in the transition state, as seen previously for long-lived protein complexes (130).

3.5. Conclusions

Most of our knowledge of protein binding kinetics derives from studies of extremely stable long-lived complexes. The binding kinetics of short-lived protein complexes are less well understood as these systems are challenging to characterize experimentally. We have applied a recently-developed combination of NMR and ITC to study complexes of the Fyn SH3 domain and several peptides whose bound lifetimes are as short as 0.3 ms. This is beyond the range of standard stopped-flow techniques used to measure binding kinetics. We find that while the binding pathways of these transient SH3 complexes are similar those of high-affinity long-lived complexes, they differ in some important respects.

For the SH3 domain, as well as for high-affinity binding partners, the transition state is stabilized by long-range electrostatic interactions, while short-range stereo-specific contacts are formed late in the binding pathway. We find that the contributions of long-range electrostatic interactions to both the fully-bound and transition states are quite similar, implying that the separation between the SH3 domain and peptide is not large in the transition state. A similar situation is believed to hold true for the transition states of high-affinity systems. Thus structural compactness and the dominance of long-range electrostatic interactions appear to be universal features of diffusion-limited binding pathways involving affinities and lifetimes spanning up to 7 orders of magnitude. However, the electrostatic acceleration of SH3 domain association rates is several orders of magnitude less than has been previously observed for stable long-lived protein complexes. In contrast, the electrostatic-free basal association rate is much greater, possibly because of looser geometrical restrictions for molecular collisions to proceed to the bound state. This raises the interesting question of whether or not this is a general phenomenon. Do weakly-bound, transient complexes intrinsically have more rapid basal association rates and less reliance on electrostatic enhancement than do tightly-bound, long-lived complexes? If so, how does this relate to the compositions and geometries of the binding interfaces? The combined NMR and calorimetric approach used here is uniquely suited for studying transient complexes to gain a better understanding of the relationships among binding affinities, basal association kinetics, and electrostatic rate enhancements and to shed light on the fundamental principles of molecular recognition.

3.6. Acknowledgements.

This work was funded by a grant from the Natural Sciences and Engineering Research Council (NSERC) of Canada. A.M is a member of Groupe de Recherche Axé sur la Structure des Protéines (GRASP). NMR experiments were recorded at the Québec/Eastern Canada High Field NMR Facility, supported by McGill University and GRASP.

4. Mapping volume changes in the binding pathway of an SH3 domain and a proline rich peptide

Research work was done in collaboration with:

Sacha Larda, Pr. Scott Prosser, Department of Chemistry, University of Toronto, UTM. Pressure NMR experiments.
Mariano Dellarole, Pr. Catherine A Royer, INSERM U554, Centre de Biochimie Structurale, Montpellier, France. Pressure Fluorescence experiments.

4.1. Summary.

Many biological processes involve stereo specific binding of a ligand to a protein. For this reason, protein-ligand binding pathways is a subject of intense research in molecular biology. The pathway gives a map that shows how a given thermodynamic or structural variable influences the stabilities, populations and formation rates of species during the association process. Numerous theoretical, computational and experimental studies have been done in order to understand how temperature, ionic strength, and mutations modulate protein-ligand association pathways. However, very few studies have characterized changes in volume occurring during protein-ligand association.

Pressure is perhaps the most convenient tool that can be used to measure changes in molar volumes in biomolecular processes. Via pressure we can quantify changes in molar volume for protein-ligand binding (181-187), protein folding (182,186,188-194) or enzymatic reactions (195,196). In the case of protein-ligand binding, measuring the association equilibrium constant as a function of pressure can give the association volume, ΔV. This is the difference in molar volume between the bound state and the unligated free state. Determining protein association rate constants at different pressures can also be used to measure the activation volume, $\Delta V^{\ddagger}$. This is the difference in volume between the transition state and the free state. These two parameters provide information on the solvation state and the mutual packing of the binding partners through the association process including the transition state.

We used protein-ligand binding equilibrium experiments that monitored tryptophan intrinsic fluorescence, together with Nuclear Magnetic Resonance (NMR) kinetics experiments, to measure the association volume and the activation volume of binding between chicken tyrosine kinase Fyn SH3 domain and a proline rich peptide. To our knowledge this is the first measurement of the activation volume for a protein/ligand binding reaction. We found that the stability of both the transition state and the final bound complex increased with pressure compared to the free state. This shows that the molar volume of the transition state as well as the molar volume of the bound state are lower than the total volume of the unbound state. These results agree with a protein-ligand binding pathway that involves significant desolvation of the binding surfaces. Interestingly, we find that the volume of transition state is very close to that of the fully bound state. This suggests that the rearrangement of solvating water molecules and any protein and ligand and conformational changes occur before the transition state, i.e. before the binding partners cross the energy barrier for association.

4.2. Introduction.

Protein-ligand interactions are essential to living systems. Protein binding affinities and kinetics are therefore important subjects of study in molecular biology. Many biologically relevant protein-ligand binding events occur through fast association processes. However, complexes with very fast association rates are hard to characterize due to the technical difficulty of measuring fast binding phenomena. In a typical non-equilibrium binding experiment, binding partners are quickly mixed and the progress of binding is followed measuring fluorescence(142,146,197), absorbance(138), suface plasmon resonance(198) or enzyme activity(120,147,148). In these cases the mixing time must be several orders of magnitude faster that the association process, otherwise the association process will be close to the end by the time of the start of the measurements. NMR dynamics experiments(199) can be effectively used to address this difficulty. The experiments are usually performed with an isotopically labeled protein sample containing a substoichiometric amount of the ligand. Due to the dynamic nature of the binding equilibrium, the NMR signal will lose intensity and will be broadened. The CPMG experiment applies a series of refocusing radiofrequency pulses in order to quench the loss of the signal. Broadening of the NMR signal is then plotted as a function of the frequency of the refocusing pulses applied. This resulting curve encodes information about the kinetics of binding(200). More precisely, we can extract the dissociation rate constant, k_{off}, the relative population of the bound state (p_{bound}) and the difference in the frequencies of the ^{15}N NMR backbone's amide signals for the apo and holo states of the protein ($\Delta\omega$). Contrary to stopped flow kinetic experiments(183), the sample remains at thermodynamic equilibrium avoiding additional "dead" times required to add or to mix the binding partners. This makes the maximum association rate limits detectable by NMR much higher than those that can be measured by other techniques.

In diffusion-limited protein-ligand binding, the association rate is largely determined by the energy of the transition state, the highest energy point on the lowest-energy pathway connecting the free and bound states. Many experimental and theoretical studies have been done in order to describe the transition states of protein-ligand binding. Many of these studies are based on measuring the stability of the transition state as a function of temperature(152), ionic strength(124), directed mutagenesis(140) or through chemical modifications of the ligand's structure(196). However, to our knowledge, volumetric properties of protein binding transition states have not been determined. These are of interest as they are related to conformational changes and rearrangement of solvation shell. NMR dynamics experiments are ideally suited for this type of analysis since commercially available high-pressure NMR systems can accurately vary the pressure in the NMR tube with a range of several kilobar.

Pressure is related to volumetric changes occurring during the binding pathway according to the pressure derivative of the free energy: $\frac{d(\Delta G_{bind})}{dp} = \Delta V$. From this, it can be derived that $K_D(p) = K_D(p_0)e^{\frac{p\Delta V}{RT}}$. A plot of $RTLn(K_d(p))$ vs p should yield a straight line with a slope equal to the molar association volume, ΔV, provided that the compressibility of the system is constant within the experimental pressure range. Similarly, according to the transition state theory, we can write: $\frac{d(\Delta G^{\ddagger})}{dp} = \Delta V^{\ddagger}$ where $\Delta G^{\ddagger}$ and $\Delta V^{\ddagger}$ are the differences in free energy and volume between the free state and the transition state, respectively. We will consider the simple two state binding scheme: $P + L \underset{k_{off}}{\overset{k_{on}}{\leftrightarrow}} PL$, where the protein exchanges between the free state, P, and the final bound conformation PL. From this model it can be inferred that a plot of $-\mathrm{RT}\,\mathrm{Ln}(k_{off})$ vs p will have as slope the change in volume between the bound state and the transition state $\Delta V_{PL\to PL^{\ddagger}}$. Using this value and the association volume ΔV, we can calculate $\Delta V^{\ddagger} = \Delta V - \Delta V_{PL\to PL^{\ddagger}}$, the activation volume for binding.

Volumetric changes can be related to changes in the molecular structure and solvation state occurring during binding according to a simple model(201) in which the association volume is: $\Delta V = \Delta V_M + \Delta V_I + \Delta V_T$; Where ΔV_M is the change in the molecular volume. This quantity can be calculated by subtracting the molecular volumes measured from crystal structures for the free ($\mathrm{V_{Mf}}$) and bound states ($\mathrm{V_{Mb}}$), to obtain: $\Delta V_M = (\mathrm{V_{Mb}} - \mathrm{V_{Mf}})$; ΔV_I measures the change in volume due to changes in solvation. This term accounts for changes in solvent volume due to electrostriction or hydrogen binding, i.e., confinement of solvent molecules on the solvent exposed surface of the protein or the ligand due to interactions with polar or charged groups. Finally, ΔV_T describes changes in thermal volume. V_T is a temperature dependent volume due to the empty layer generated by the thermal collision between the molecules of the solvent with protein and ligand residues that are solvent accessible. This term can be equivalently expressed as $\Delta V_T = \delta\ \Delta S_A$, where δ is the thickness of the empty layer and ΔS_A is the change in the surface accessible to solvent upon binding.

We have used intrinsic fluorescence titration experiments and NMR relaxation dispersion dynamics experiments performed over pressures ranging from 1 to 2000 bar to map the changes in volume occurring along the binding pathway of the Fyn SH3 domain and a proline rich peptide Ac-FSLARRPLPPLP-NH_2. The peptide used in our studies is a class I proline rich peptide(202) that adopts a polyproline II helix conformation(36) upon binding. Its sequence contains two positively charged consecutive R5 R6 residues preceding a proline rich P7 L8 P9 P10 L11 P12 motif that interacts via electrostatics with three negatively charged acidic residues on protein's binding pocket (PDB 4EIK: E99 D100 D101). Using tryptophan fluorescence titration experiments, we measured a molar association volume of ~ 44 ml mol^{-1} (this value is the slope of the curve shown in figure 4.3). Analysis of changes in molecular volumes using X-ray crystal structures, together with the measurement of the change in exposed solvent surfaces for the free and bound states yielded $\Delta V_M \approx$ 114 ml mol^{-1} (explained in section 4.5.2.) and $\Delta V_T \approx$ -394 ml mol^{-1} (see section 4.5.2), giving $\Delta V_I \approx$ 236 ml mol^{-1} (section 4.5.2). This agrees with an increase of the interaction volume due to desolvation caused by the release of densely packed water around polar and charged groups on the free protein and the free peptide upon the formation of the final bound complex. CPMG NMR kinetics experiments showed that the difference in volume between the transition state and the bound complex is just ~ 4 ml mol^{-1}. This value is in agreement with typical volume changes for hydrogen bond formation(203). The similar molar volumes obtained for the fully bound and transition states indicate that conformational changes and solvent rearrangements responsible for the molar volume of binding are largely complete before the energy barrier to binding. This contrasts strongly with previous models of the protein binding transition states in which the protein ligand are separated by several layers of solvent. Implications for binding pathways are discussed.

4.3. Experimental

4.3.1. Protein and peptide purification

Residues 81 to 148 from wild-type chicken Fyn SH3 domain was purified as described previously (204). Proline rich peptide Ac-FSLARRPLPPLP-NH_2 was purchased from Sheldon Biotechnology Centre (McGill University, Montreal) and purified to homogeneity using reverse-phase HPLC. Protein and peptide were dialyzed against 5 mM MES pH 6.0 and used to perform intrinsic tryptophan fluorescence experiments and CPMG NMR experiments. All the data were collected at 40°C. This temperature was chosen to be close to physiological conditions.

4.3.2. Intrinsic tryptophan fluorescence experiments

Samples containing $r = \frac{[peptide]_{Total}}{[Protein]_{Total}}$ values of 0, 0.5, 1.25, 1.75, 2.5 and 5.0 were used to measure intrinsic tryptophan fluorescence. Where $[peptide]_{Total}$ and $[Protein]_{Total}$ are respectively the total peptide and protein concentrations in the sample. Emission spectra were obtained with excitation at 276 nm and emission scanned from 300 to 400 nm. Experiments were performed at barometric pressures of 1, 50, 250, 500, 750, 1000, and 1250 bar as illustrated elsewhere(205). For every pressure datum, the center of spectral mass $\langle \nu_r \rangle$ at each r value was calculated as $\langle \nu_r \rangle = \frac{\sum \nu_i F_i}{\sum F_i}$; where F_i stands for the fluorescence intensity at the wavelength ν_i and the summation is carried out over a range of significant values of F_i.

The change in the center of spectral mass $\langle\nu_r\rangle$, was then individually fitted according to a binding process involving two conformational states of the protein:

$$\langle\nu_r\rangle = \langle\nu_{free}\rangle + \frac{1}{2}\left(\langle\nu_{sat}\rangle - \langle\nu_{free}\rangle\right)\left(b^2 - \sqrt{b^2 - 4r}\right)$$

Where $\mathrm{b} = 1 + \mathrm{r} + \frac{\mathrm{K_D(p)}}{[\mathrm{protein}]_{\mathrm{total}}}$, and $\langle\nu_{free}\rangle$ and $\langle\nu_{sat}\rangle$ are the respective centers of spectral mass for the free unbound protein and the fully saturated protein. After fitting, pressure dependent dissociation equilibrium constants $K_D(p)$ are obtained. $K_D(p)$ values are subsequently fitted to $K_D(p) = K_D(p_0)e^{\frac{p\Delta V}{RT}}$ in order to extract the association volume ΔV.

4.3.3. Changes upon binding in molecular volume $\Delta \boldsymbol{V_M}$, thermal volume $\Delta \boldsymbol{V_T}$, and measurement of accessible solvent surfaces for the free and bound states

We used the rolling probe method(206-208) in order to calculate molecular volumes and solvent accessible surfaces for the protein and the peptide. We rolled a spherical virtual probe of radius 1.4 Å (assumed radius for a water molecule) over the Van-der-Waals surface of both the protein and peptide at the free and bound states. Van-der-Waals surfaces for these two states were calculated from available X-ray crystal structures. A discrete 3D grid with a voxel of 0.5 Å was used in all the calculations as described elsewhere(209). PDB entry 3UA6 X-ray crystal structure of the chicken fyn SH3 domain was used to measure the molecular volume for the free protein $\mathrm{V_{Mfp}}$, and also to obtain the solvent accessible surface of the protein at the free state $\mathrm{S_{fp}}$. PDB: 4EIK X-ray crystal structure of the chicken fyn SH3 domain bound to the proline rich peptide was used to calculate the molecular volume for the final bound state $\mathrm{V_{Mb}}$, and the solvent accessible surface of the bound complex $\mathrm{S_b}$. Conformation of the peptide in the free and bound states were considered to be the same. Upon binding, proline rich peptide shows a characteristic poly-proline II conformation. It has been shown that proline rich peptides similar to the one used in our studies can adopt a poly-proline II conformation in solution at the free state(210). This particular conformation is also confirmed in the X-ray structure of the bound state for several types of different proline rich peptides(211). For this reason the Van der-Waals volume of the peptide at the bound state was used to calculate both the solvent accessible surface of the free peptide $\mathrm{S_{fL}}$, and the molecular volume of the unbound peptide $\mathrm{V_{MfL}}$. Under these conditions we obtain: $\mathrm{V_{Mf}} = \mathrm{V_{Mfp}} + \mathrm{V_{MfL}}$ and $\Delta S = \mathrm{S_b} - (\mathrm{S_{fL}} + \mathrm{S_{fp}})$.

4.3.4. CPMG experiments

^{1}H-decoupled ^{15}N CPMG experiments(155) with power compensation schemes(152) were performed at 40°C. Samples were inserted into an standard NMR ceramic tube (Daedalus Innovations LLC, Aston, Philadelphia) with a 3.0 mm inner diameter and pressurized using mineral oil. Pressure points at 1, 500, 1000, 1500 and 2000 bar were obtained. Experiments were done at 600 MHz on 1 mM samples of the Fyn SH3 domain in the presence of 0.1 mM peptide. We used a constant relaxation delay, T_{relax}, of 40 ms and twenty-three values of $\nu_{CPMG} = 1/(2\tau_{CP})$ ranging from 25 to 1000 Hz, where τ_{CP} is the delay between consecutive pulses. Transverse relaxation rates, R_2, were calculated for each cross-peak signal at each ν_{CPMG} value according to:

$$R_2^{\exp}(\nu_{CPMG}) = -\frac{1}{T_{relax}} \ln\left\{\frac{I(\nu_{CPMG})}{I_0}\right\}, \tag{4.1}$$

where $I(\nu_{CPMG})$ is the peak intensity at a given value of ν_{CPMG} and I_0 is the signal intensity with $T_{relax}=0$. The experimental uncertainties in peak intensities (σ_I) were considered to be the same for all values of ν_{CPMG} for a given residue at a given pressure. CPMG experiments were repeated for a subset of ν_{CPMG} values (N_{dup} different values) with n_j replicates obtained at the jth repeated ν_{CPMG} value. The n_j replicates obtained at $(\nu_{CPMG})_j$ for a given residue, pressure, and static magnetic field yield a standard deviation s_j. The uncertainty in σ_I was calculated as:

$$\sigma_I^2 = \frac{\sum_{j=1}^{N_{dup}} s_j^2 (n_j - 1)}{\sum_{j=1}^{N_{dup}} (n_j - 1)} , \qquad (4.2)$$

and the associated errors in transverse relaxation rates, σ_{R2}, are given by:

$$\sigma_{R2}(\nu_{CPMG}) = \frac{\sigma_I I_0}{T_{relax} I(\nu_{CPMG})} . \qquad (4.3)$$

CPMG data were fitted using a two-state model of conformational exchange:

$$P + L \underset{k_{off}}{\overset{k_{on}[L]}{\rightleftarrows}} PL , \qquad (4.4)$$

where P is the protein, L is the ligand, PL is the complex, *k_{off}* is the dissociation rate constant, *k_{on}* is the association rate constant, [L] is the concentration of free peptide, and the difference between the precession frequencies of an ^{15}N nucleus of the protein in the free and bound states is given by $\Delta\omega$.

Dispersion profiles were analyzed according to(164)

$$R_2(\nu_{CPMG}) = \tfrac{1}{2}\left(R_{2free}^0 + R_{2bound}^0 + k_{ex} - 2\nu_{CPMG}\cosh^{-1}\left(D_+\cosh(\eta_+) - D_-\cosh(\eta_-)\right)\right)$$

$$D_\pm = \tfrac{1}{2}\left(\pm 1 + \frac{\psi + 2\Delta\omega^2}{\sqrt{\psi^2 + \xi^2}}\right) \qquad (4.5)$$

$$\eta_\pm = \frac{\sqrt{2}}{4\nu_{CPMG}}\sqrt{\pm\psi + \sqrt{\psi^2 + \xi^2}}$$

$$\psi = \left(R_{2free}^0 - R_{2bound}^0 + p_{free}k_{ex} - p_{bound}k_{ex}\right)^2 - \Delta\omega^2 + 4p_{free}p_{bound}k_{ex}^2$$

$$\xi = 2\Delta\omega\left(R_{2free}^0 - R_{2bound}^0 + p_{bound}k_{ex} - p_{free}k_{ex}\right).$$

We performed the analysis assuming that $R_{2free}{}^0 = R_{2bound}{}^0$. This is typically done in analyses of CPMG data, since it is not possible to reliably extract separate values for $R_{2free}{}^0$ and $R_{2bound}{}^0$.(165) In this case, the approximation is likely valid, as binding of the peptide is unlikely to substantially alter ^{15}N transverse relaxation rates in the protein.

Dispersion profiles data for all residues of a given sample were fitted simultaneously to extract global values of p_{bound} and k_{ex}, while $\Delta\omega^2$ or Φ_{ex}, $R_2{}^0$(600 MHz), were obtained on a per-residue basis.(12) Values of k_{off} were subsequently calculated as $(1-p_{bound})k_{ex}$. Errors in the extracted parameters were estimated using a Monte Carlo approach in which group fitting was performed on random subsets of the residues selected using a bootstrap procedure.(166) Analyses were performed using in-house scripts written in MATLAB (MALAB R2011b, The MathWorks, Natick, MA).

4.5. Results

4.5.1. Intrinsic tryptophan fluorescence experiments

Figure 4.1 shows protein's intrinsic tryptophan fluorescence emission spectra for chicken fyn SH3 domain containing different concentrations of peptide, $r = \frac{[peptide]_{Total}}{[Protein]_{Total}}$.

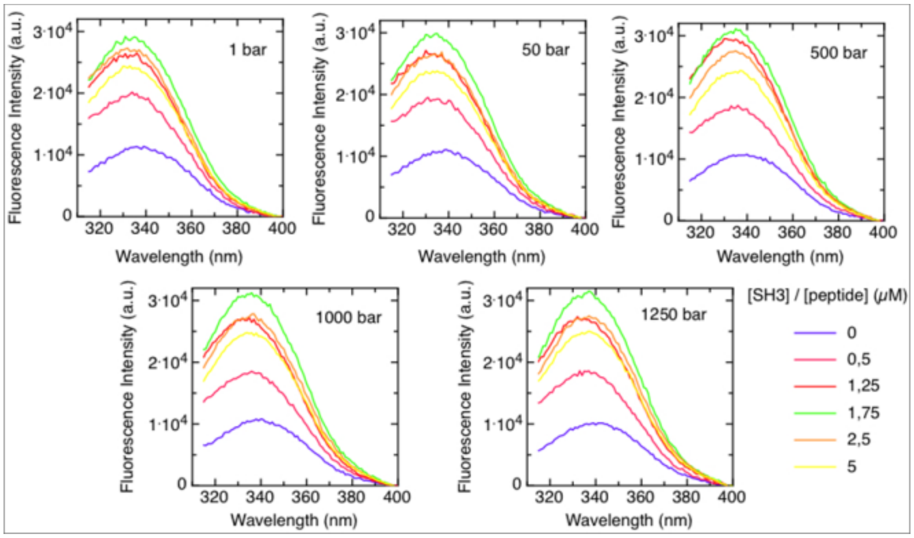

Figure 4.1. Chicken Fyn SH3 domain intrinsic Trytophan fluoresence spectra for samples containing $r = \frac{[peptide]_{Total}}{[Protein]_{Total}}$ values of 0, 0.5, 1.25, 1.75, 2.5 and 5.0. Where $[peptide]_{Total}$ and $[Protein]_{Total}$ are respectively the total peptide and protein concentrations in the sample.

For all the pressures studied, the emission spectra showed an increase in the center of spectral mass of the fluorescence signal with the increase of r. Center of spectral mass is a better indicator and is used instead of maximum signal intensity. This can be evidenced by the decrease of maximum signal fluorescence intensity at r values of 2,5 and 5 for all the pressures (Figure 4.1.). It is convenient to recall that the ligand peptide does not contain tryptophan residues. Protein concentration was kept at the same value of 1 uM throughout the fluorescence experiments. Under these conditions, an increase in intrinsic tryptophan fluorescence emission signal is only due to ligand binding induced modifications of the local micro-environment of tryptophan and their rotational motions.

Values of r were plotted against center of spectral mass $\langle \nu_r \rangle$, for every pressure as shown in Figure 4.2.

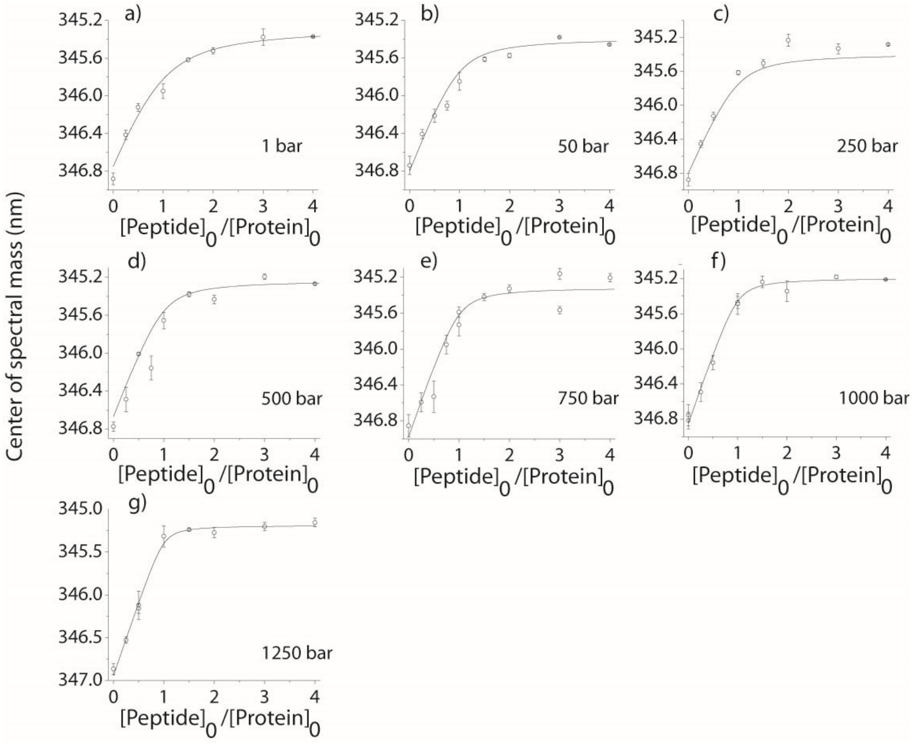

Figure 4.2. $r = \frac{[peptide]_{Total}}{[Protein]_{Total}}$ vs center of spectral mass for binding between chicken fyn SH3 domain and Ac-FSLARRPLPPLP-NH$_2$ peptide.

Values of dissociation binding constant as a function of pressure, $K_D(p)$, were extracted as explained in section 4.5.1. These results are summarized in Table 1.

Table 4.1. Pressure effect on the binding between chicken fyn SH3 domain and Ac-FSLARRPLPPLP-NH_2 peptide.

Pressure (bar)	K_D (nM)	ΔG (kcal mol^{-1})
1	222.7 ± 29.9	-9.53 ± 0.08
50	90.6 ± 17.8	-10.09 ± 0.12
250	77.7 ± 15.1	-10.19 ± 0.12
500	65.9 ± 21.7	-10.29 ± 0.20
750	42.2 ± 18.7	-10.57 ± 0.28
1000	28.0 ± 12.7	-10.82 ± 0.28
1250	16.8 ± 14.4	-11.14 ± 0.53

Experiments were performed in 5 mM MES pH 6.4 at 40°C.
Change in free energy of binding was calculated using $\Delta G = RTLn(K_D)$
Errors were propagated from K_D

The association binding constant obtained at 1 bar is in agreement with previous results measured by Isothermal Titration Calorimetry(152). Figure 4.3 shows a plot of the change in the free energy of binding, $\Delta G_{binding} = RTln(K_D)$ vs pressure. Data can be fitted to a straight line with a slope equivalent to molar association volume, ΔV = -43.93 $\pm$ 6.1 ml mol^{-1}.

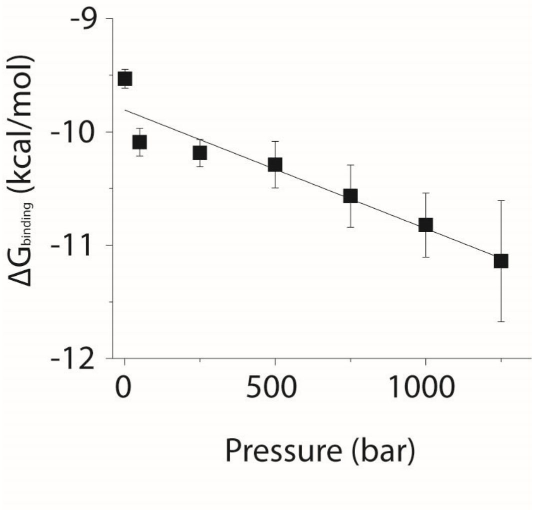

Figure 4.3. Change in free energy of binding as a function of pressure for the system chicken fyn SH3 domain/Ac-FSLARRPLPPLP-NH_2 peptide. Experiments were performed in 5 mM MES pH 6.4 at 40°C. Linear fit has a slope equivalent to a $\Delta V = (-43.93 \pm 6.1)\ ml\ mol^{-1}$.

This value reflects the stabilizing effect that pressure has in the formation of the final bound complex. Results agree with the Le Chatellier's principle, i.e., since $\left[\frac{\partial(\Delta G_{binding})}{\partial p}\right]_T = \Delta V$, for an spontaneous binding process, the increase in the barometric pressure will displace the binding equilibrium towards the state that has the lower molar volume, for this particular case, the most stable state is the bound state. However, protein-ligand binding can show negative or positive association volumes, for this reason we used a semi-quantitative model to explain our results.

4.5.2. Measurement of $\Delta\mathbf{V_M}$, $\Delta\mathbf{V_T}$ and analysis of $\Delta\mathbf{V_I}$

Changes in molecular volume for binding can be calculated as $\Delta V_M = (\mathrm{V_{Mb}} - \mathrm{V_{Mf}})$. Molecular volume in the free state $\mathrm{V_{Mf}}$ was calculated as the sum of the molecular volumes of the free unbound protein $\mathrm{V_{MfP}}$ and the molecular volume of the free ligand $\mathrm{V_{MfL.}}$ Where: $\mathrm{V_{Mf}} = \mathrm{V_{MfP}} + \mathrm{V_{MfL.}}$

Molecular volume for the bound state, $\mathrm{V_{Mb}}$, was calculated using 4EIK PDB entry. A value of 9854 Å^3 per molecule was obtained as described in the experimental section, this values are typically not reported with errors. This molecular volume is equivalent to $\mathrm{V_{Mb}} =$ 5934 ml mol^{-1}.

Values of $\mathrm{V_{MfP}} =$ 8123 Å^3 per protein and $\mathrm{V_{MfL}} =$ 1542 Å^3 per peptide were measured. These values provided the molecular volume for the free state, $\mathrm{V_{Mf}} = \mathrm{V_{MfP}} + \mathrm{V_{MfL}}$ = 9665 Å^3 per protein-ligand pair, equivalent to $\mathrm{V_{Mf}} =$ 5820 ml mol^{-1}. We finally obtained a change in molecular volume for binding of $\Delta V_M = (\mathrm{V_{Mb}} - \mathrm{V_{Mf}}) =$ 114 ml mol^{-1}. This difference in molecular volume can be explained by conformational changes in the protein upon binding, together with changes in cavity volumes in the protein during the formation of the bound complex. We used castP analysis(212) in order to determine changes in cavity volumes for both free and bound states of the protein. In crystals obtained at 1 bar we identified a cavity (packing defect), or internal void volume. This cavity fluctuates among different asymmetric units or crystals as shown in Figure 4.4.

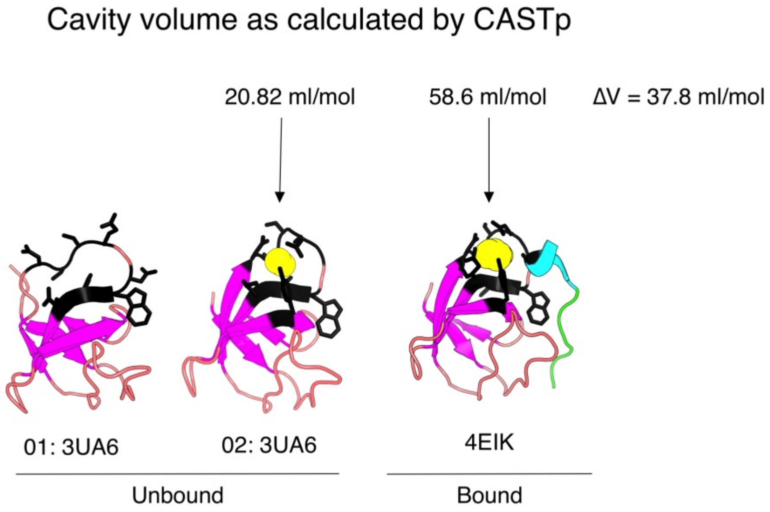

Figure 4.4. Cavity volume calculations for the free and bound states using castP.

The estimated change in volume for that cavity between the free and bound states is $\Delta V_c = \sim$ 38 ml mol^{-1}.This lead us into an scenario where the changes in molecular volume observed upon binding can be expressed as $\Delta V_M = \Delta V_c + \Delta V_{VW}$, where $\Delta V_{VW} = \sim 76 \text{ ml mol}^{-1}$ accounts for the estimated Van der Waals volume change upon binding(213).

Change in thermal volume was obtained using the expression $\Delta V_T = \delta\, \Delta S$. A value of 1 Å for δ is a good approximation for the effective thickness of the thermal volume around a globular protein(214). A value for the solvent accessible surface of the bound state $\mathrm{S_b}$= 3461 Å^2 per molecule was obtained. For the free unbound state we measured the following solvent accessible surfaces: $\mathrm{S_{fL}}$= 1092 Å^2 per peptide molecule, and $\mathrm{S_{fp}}$= 3023 Å^2 per molecule of protein. This lead us to a change in the solvent accessible surface of $\Delta S = \mathrm{S_b} - (\mathrm{S_{fL}} + \mathrm{S_{fp}})$ = -654 Å^2 per final bound complex formed. This value was used to calculate the change in thermal volume for the binding process, $\Delta V_T = \delta\,\Delta S = -394$ ml mol^{-1}.

We can use now the expression: $\Delta V_I = \Delta V - \Delta V_M - \Delta V_T$, to estimate the change in the interaction volume upon binding.We obtained a value of ΔV_I =236 ml mol^{-1}. This number is in agreement with similar association process found for several globular proteins(214). Changes in interaction volumes can also help to estimate the amount of solvation water molecules surrounding the solvent accessible surface of the protein in the free unligated state. The value of ΔV_I can also be expressed as the product: $\Delta V_I = -\Delta n_{\hbar}(V_{\hbar} - V_0)$, where $V_{\hbar}$ and V_0 are average molar volumes for hydration shell water and bulk water, and $\Delta n_{\hbar}$ is the number of hydration water molecules that are released into the bulk solvent upon binding. An average value for $(V_{\hbar} - V_0)$ = -1.8 cm^3 mol^{-1} has been already estimated for globular proteins(214). This reveals a value of $\Delta n_{\hbar} = \frac{-\Delta V_I}{(V_{\hbar} - V_0)} = 131$ molecules of water released per bound complex formed. This value is almost 2 times the number of the water molecules expected for this protein in the first coordination water layer. A value of 73 water molecules in the first coordination layer can be estimated by the division of the change in the solvent accessible surface ΔS by the effective cross-section of a water molecule 9 Å^2. This drastic difference between $\Delta n_{\hbar}$ and the expected amount of water in the first coordination layer can be explained by the fact that certain regions on the protein surface can be hydrated by more than one layer of water molecules in the free state. This result agrees with previously studied systems.

4.5.3. CPMG NMR kinetic experiments

Table 4.2 shows the rate exchange, $k_{ex} = k_{on} + k_{off}$, the dissociation constant, k_{off}, and the population of the bound state p_b for CPMG NMR samples used to measure binding kinetics as a function of pressure. Results shows a decrease in the dissociation rate constant with the increase in barometric pressure.

Table 4.2. Kinetic parameters of binding between Fyn SH3 domain and a proline rich peptide at different pressures.

Pressure (bar)	k_{ex} (s^{-1})	$(\boldsymbol{p_b})_{CPMG}$	$(\boldsymbol{p_b})_{calc}$	k_{off} (s^{-1})	$\Delta G_{\mathrm{PL}\rightarrow\mathrm{PL}^{\ddagger}}$ (kcal mol^{-1})
1	250 ± 0.4	0.0696 ± 9.40 x 10^{-5}	0.1	232.6 ± 0.051	3.391 ± 0.015
500	232 ± 0.6	0.074 ± 1.60 x 10^{-4}	0.1	217.1 ± 0.082	3.348 ± 0.024
1000	198 ± 0.2	0.0718 ± 6.92 x 10^{-5}	0.1	188.9 ± 0.028	3.261 ± 0.007
1500	197 ± 0.4	0.0641 ± 1.03 x 10^{-4}	N/A	193.8 ± 0.046	3.278 ± 0.014
2000	175 ± 0.5	0.0701 ± 1.59 x 10^{-4}	N/A	175.8 ± 0.063	3.217 ± 0.020

Experiments were performed in 5 mM MES pH 6.4 at 40°C.

Change in free energy of binding was calculated using $\Delta G_{\mathrm{PL}\rightarrow\mathrm{PL}^{\ddagger}} = RTLn\left(k_{off}\right)$

Errors were propagated from k_{off}

Figure 4.5 shows a plot of $RT\ Ln(k_{off})$ vs p. Data can be fitted to a straight line with slope -3.5 $\pm$ 0.7 ml mol^{-1} equivalent to the change in molar volume between the final bound complex and the transition state, $\Delta V_{PL \to PL^{\ddagger}}$.

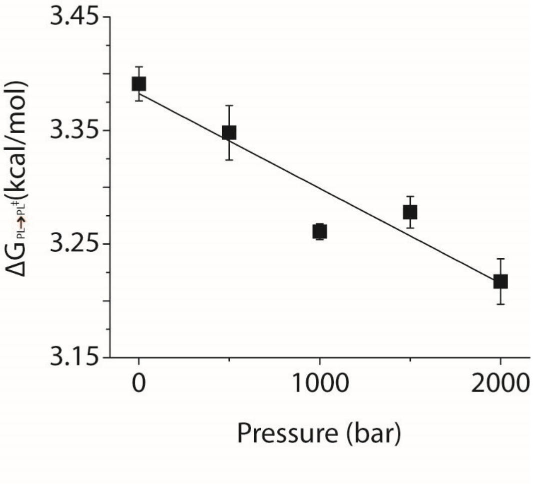

Figure 4.5. Change in free energy between the bound state and the transition state as a function of pressure for the system chicken fyn SH3 domain / Ac-FSLARRPLPPLP-NH$_2$ peptide. Experiments were performed in 5 mM MES pH 6.4 at 40°C. Linear fit gives $\Delta V_{PL \to PL^{\ddagger}} = (3.51 \pm 0.68)$ ml mol^{-1}.

From this value we can calculate the activation volume for our system: $\Delta V^{\ddagger} = \Delta V - \Delta V_{PL \to PL^{\ddagger}}$ = -40.5 $\pm$ 6.7 ml mol^{-1}. The small change in volume between the transition state and the final bound state shows that, volume wise, the final bound state is virtually formed at the transition state. Binding kinetic parameters were obtained after running CPMG at just one magnetic field of 14 T. Analysis of

CPMG experiments usually require to run this experiment at two different magnetic fields. In our case we confirmed the accuracy of the kinetic parameters obtained through CPMG using a double control.

Firstly, we measured the HSQC NMR ^{15}N frequency change for the amide bond signals of the backbone of the protein between the fully saturated state and the free unbound state of the protein $(\Delta\omega_i)_{HSQC}$. Then we compared each $\left|(\Delta\delta_i)_{HSQC}\right|$ previously measured with the equivalent predicted value obtained through CPMG experiments $|(\Delta\omega_i)_{CPMG}|$. Figure 4.6 shows a plot of $\left|(\Delta\delta_i)_{HSQC}\right|$ vs $|(\Delta\omega_i)_{CPMG}|$, i.e., the maximum experimental chemical shift displacements measured and those predicted after CPMG, for every pressure, results are compared to a linear fit of slope 1 and intercept zero.

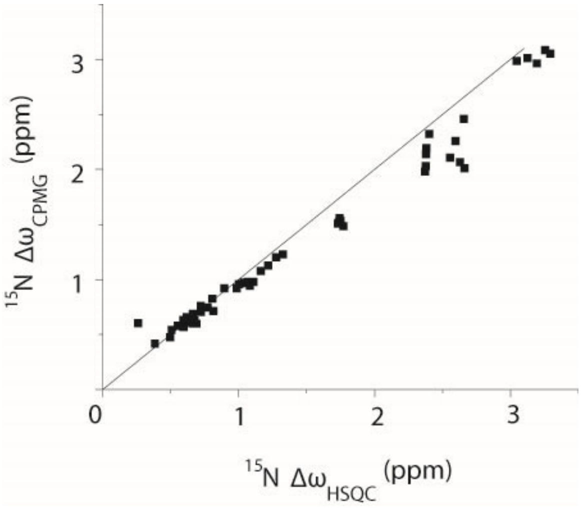

Figure 4.6. Plot of $\left|(\Delta\delta_i)_{HSQC}\right|$ vs $|(\Delta\omega_i)_{CPMG}|$ for every residue used to calculate kinetic parameters at every the pressures.

Secondly, in Table 4.22 we compared the population of the bound state p_b for every pressure after analysis results of CPMG experiments, $(p_b)_{CPMG}$, with the values expected after calculation of p_b using the measured association equilibrium constants and peptide and protein concentrations of the CPMG NMR sample, $(p_b)_{calc}$. Both internal controls confirm, within experimental error that the binding kinetic parameters obtained after analyzing one field CPMG results are reliable. A full map of volume changes on binding is shown in figure 4.7.

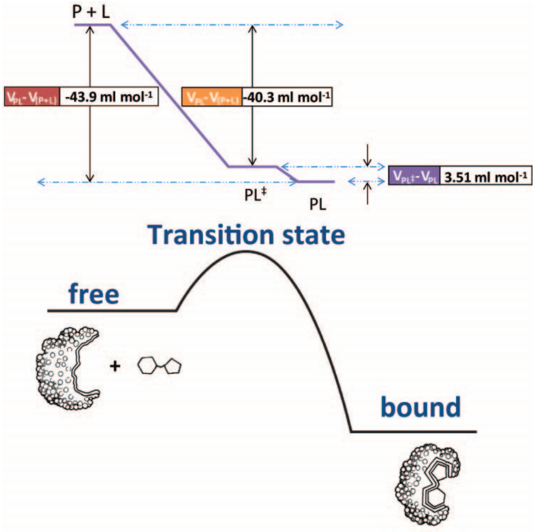

Figure 4.7. Volume change map for binding between a chicken fyn SH3 domain and Ac-FSLARRPLPPLP-NH$_2$ peptide. Values were measured in a buffer containing 5 mM MES at pH 6.4 and 40°C.

4.6 Conclusion

Kinetic NMR methods can be effectively used to measure activation volumes in fast binding systems. CPMG NMR experiment have proven to be the only technique available nowadays that can unveil the slight change in volume between the transition state and the final bound state for binding between chicken fyn SH3 domain and the peptide Ac-FSLARRPLPPLP-NH_2. It was only through kinetic NMR experiments that we were able to measure the fast, diffusion limited kinetics of binding of our system.

Results likely show that the binding pathway between the Fyn SH3 domain and the proline rich peptide goes through a water desolvation step, this desolvation steps involves more than one coordination water layer for the protein in the free unbound state. Kinetics NMR experiments also show that the desolvation step is mostly achieved at the transition state. Results agree with previously studied systems where the binding stability and the speed of binding is mainly driven by electrostatics.

5. NMR experimental approaches to study binding of bisphophonates to human Farnesyl Pyrophosphate Synthase (hFPPS)

Research work was done in collaboration with:

Profesor Youla Tsantrizos, Department of Chemistry, McGill University.

5.1. Overview.

Farnesyl pyrophosphate synthase (FPPS) is a 1'-4 prenyl transferase, chain elongation enzyme, that catalyzes two consecutive condensations steps of isopentenyl diphosphate (IPP) with allylic diphosphates. The first condensation step is done with dimethylallyl diphosphate (DMAPP) and the second with the resultant geranyl diphosphate (GPP). The final product of these consecutive enzymatic reactions is farnesyl pyrophosphate (FPP). FPP is further used in the synthesis of sterols, dichols, carotenoids, withanolides, ubiquinones, mitochondrial electron transfer chain components, prenylated proteins and various sesquiterpenoids including fytoalexins. Isoprenoid biosynthetic pathway has gained more importance in the last years. This is since key enzymes of this pathway, including FPPS have been characterized and the their functional roles in metabolism have been explored using molecular biology.

Human FPPS (hFPPS) is an enzyme with a relevant pharmacological importance. This synthase is composed of 375 residues and has a molecular weight over 43 kDa. It plays an important role in the first branching point of the mevalonate pathway (Figure 5.1).

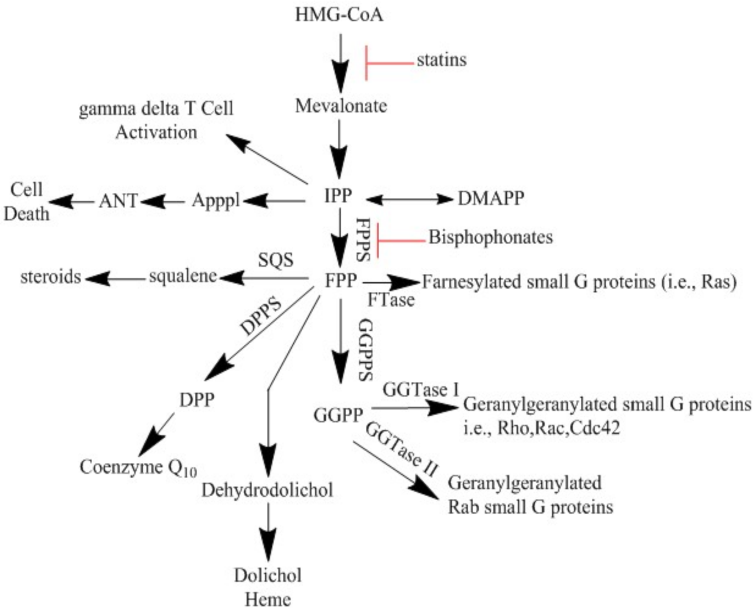

Figure 5.1. Schematic representation of the mevalonate pathway.

This metabolic pathway is implicated in the synthesis of sterol isoprenoids including cholesterol and non-sterol isoprenoids such as dolichol, isopentenyl tRNA, heme-A and ubiquinone. Mevalonate pathway have been extensively studied in regard with cholesterol synthesis and its relationship with cardio vascular diseases. However, in recent years this metabolic pathway have also called the attention since a large number of clinical and experimental studies have suggested that inhibition of non-sterol isoprenoids may have importance in the treatment of human diseases. These non-sterol molecules that control cell growth and differentiation seem to be important in fields such as oncology, autoimmune disorders, atherosclerosis, and Alzheimer disease. For these reasons, this metabolic pathway has been successfully targeted in the pharmacological treatment of different diseases(215,216).

Bisphophonates (Figure 5.2) are characterized pharmacologically by their ability to inhibit bone resorption. These compounds characterized by P−C−P bonds, bind strongly to the bone mineral at sites of active bone metabolism, where they achieve therapeutic concentrations.

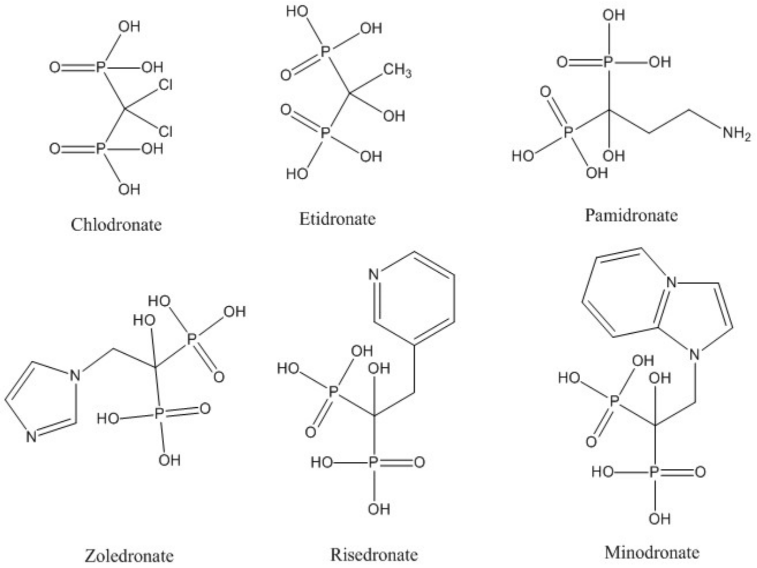

Chlodronate Etidronate Pamidronate

Zoledronate Risedronate Minodronate

Figure 5.2. The structure of some simple bisphophonates.

Bisphophonates have been clinically used as inhibitors of hFPPS to treat bone loss mediated by increased osteoclast activity(217-219). For more than 30 years bisphophonates have been clinically prescribed to treat Paget disease of bone, osteoporosis, malignant metastasis in bone and multiple myeloma(220). Despite the clinical importance of this enzyme, very few solution NMR studies have been done to unveil the molecular underpinnings of the interaction between hFPPS and bisphophonate inhibitors(221-223). To date (2014), these studies have been exclusively ligand-based NMR experiments(221). To our knowledge, no successful protein NMR studies have been done on binding between hFPPS and bisphophonates.

We explored the use of solution NMR to gain insight into the interaction between hFPPS and bisphophonate inhibitors. NMR is so far the only technique that can be used to gain atom detailed, protein structural information in solution state. Also, protein NMR experiments can provide structural information relatively faster than crystal X-ray diffraction techniques. NMR not only gives protein structural information but also can provide underpinning molecular insights about dynamics, binding kinetics, folding and different biological processes including enzymatic activity.

The initial step consisted in the expression and purification of ^{15}N isotopically labeled protein. This protein is further used to perform HSQC NMR experiments. In order to improve spectral resolution, different isotopically labeled versions of hFPPS were tried. These include lysine labeling, protein deuteration and perdeuration and finally specific labeling (^{1}H,^{13}C) of methyl groups on isoleucine, valine and leucine. Expression was optimized to improve yield and was done as follows.

5.2. hFPPS expression and purification

Wild-type human FPPS was initially expressed and purified following a protocol described elsewhere(50,224). This protocol was further adapted to produce ^{15}N isotopically labeled protein. hFPPS was expressed in E. coli BL21 DE3 cells. They were grown in 4L of LB broth at 37ºC until the culture reached an optical density of 0.6-0.8 at 590 nm. The cells were then transferred into 1L of M9 modified medium(225) at 18ºC containing ~100% labeled ^{15}N ammonium chloride. Protein expression was allowed to proceed overnight after induction with 1 mM IPTG. After following the previous purification protocol (50,224), two additional further steps are needed to obtain an NMR sample. The first consisted in dialysis followed by size exclusion chromatography (Fast Protein Liquid Chromatography FPLC, using a Superdex 75 10/300 GL column). Dialysis buffer and FPLC running buffer contained 25 mM TRIS, 150 mM NaCl, 2 mM beta-mercaptoethanol, pH 7.5. The second and final step consisted in dialysis in NMR buffer containing 25 mM TRIS, 25 mM NaCl, 2 mM beta-mercaptoethanol, pH 7.5. Protein samples where further concentrated to the desired value using centrifugal filters (Millipore AMICON ultra 10,000 MWCO).

5.3. HSQC NMR experiments on hFPPS.

^{1}H-^{15}N Heteronuclear Single Quantum Coherence experiments where performed at 40ºC on a ^{15}N isotopically labeled hFPPS sample at ~250 uM protein concentration. Figure 5.3 shows the HSQC spectrum obtained after overnight data acquisition (18.8 Tesla). This is an unusually long acquisition time for this type of NMR experiment given the relatively high concentration of the sample and the molecular weight of hFPPS. Regardless these conditions, the spectrum shown in figure 5.3 lacks of enough spectral resolution. i.e., it is virtually impossible to identify particular cross-peaks (signals) corresponding to pairs of N-H atoms present in the ^{15}N isotopically labeled protein.

Under optimal conditions, a regular ^{1}H-^{15}N HSQC spectrum provides a well-resolved signals for each N-H pair present in the protein. These can derive either from the amide bonds in the backbone of the protein or N-H bonds present in the side chains of certain amino acids such as Tryptophan, Lysine, Arginine, Histidine, Asparagine and Glutamine. ^{1}H-^{15}N HSQC spectrum show cross-peaks of hFPPS with excessive broadening that hampers the identification of the expected signals.

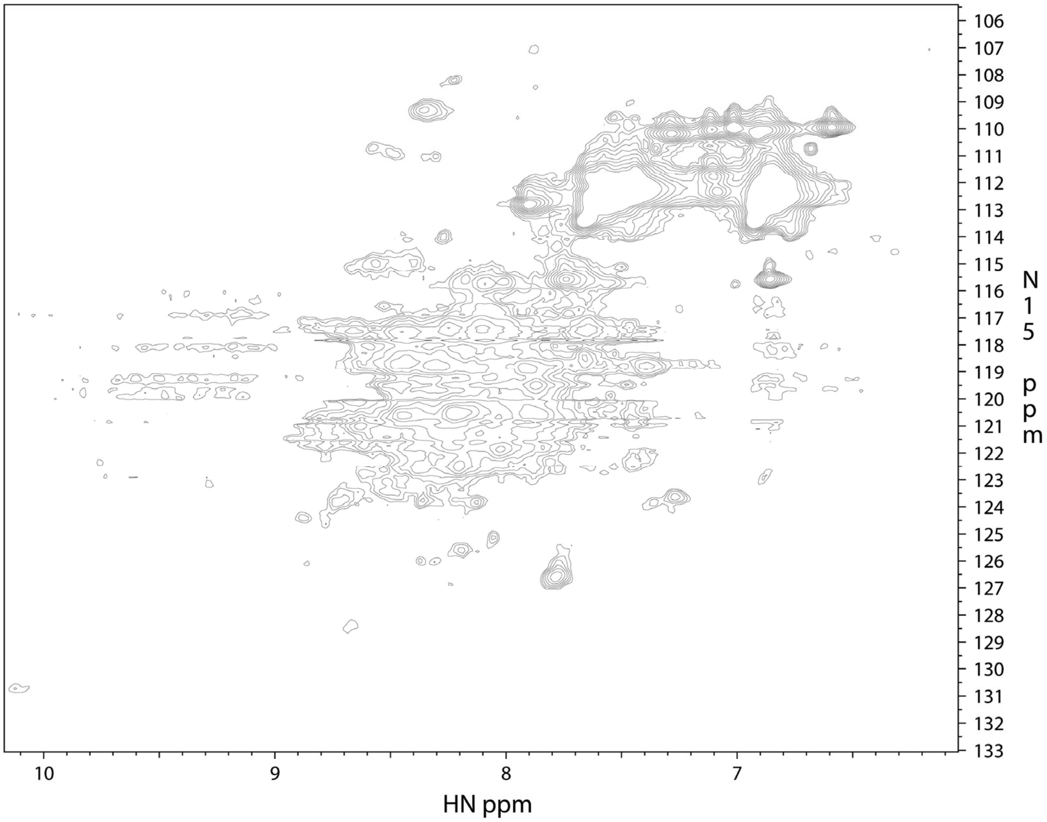

Figure 5.3. ^{1}H-^{15}N HSQC spectrum for the Apo form of hFPPS.

Peak broadening in NMR spectra is caused by two different reasons. Firstly it can be due to Homogeneous broadening. This phenomena is the consequence to small fluctuations of microscopic magnetic fields around the spin system. This broadening is quantified by the transverse relaxation time constant T_2. Secondly, NMR signals can also be broadened by inhomogeneous broadening. This is due to spatial imhomogeneity of the macroscopic magnetic field that surrounds the NMR sample. It is normally caused by imperfections in the NMR instrumentation or to susceptibility effects in the sample. In order to diminish inhomogeneous broadening we used Shigemi tubes designed for Varian spectrometers. The next logical step was to improve NMR spectral resolution by diminishing cross-peak broadening caused by homogeneous broadening.

Signal broadening observed in the spectrum shown in figure 5.3 may be due to protein conformational exchange occurring in the millisecond to microsecond time scale. A protein that can exchange among conformational states in the μs to ms time scale typically shows NMR signals with broadening or "disappearance" of certain N-H cross-peaks due to conformational exchange. In order to reduce exchange, the protein can be locked into a "rigid conformation". i.e., a state characterized by a relatively slower conformational exchange rate. In this case it was decided to lock the protein conformation by populating a well characterized bound state of the enzyme (226,227). According to previous work(50) this can be achieved by adding to the protein NMR sample a stoichiometric excess of magnesium, the bisphophonate inhibitor Zoledronate and pyrophosphate. The final effect of these compounds is to populate a highly stable inhibited state of the protein. This state reduces the conformational space that hFPPS can populate and also may decrease the conformational exchange rate of the protein. Figure 5.4 shows the spectrum (18.8 Tesla) of hFPPS (~400 uM) saturated with

Magnesium, Zoledronate (~400 uM) and pyrophosphate (~400 uM). Spectral resolution was improved. However the results obtained are still far from the quality desired. Under these conditions the system is not suitable to perform any further binding studies via protein NMR.

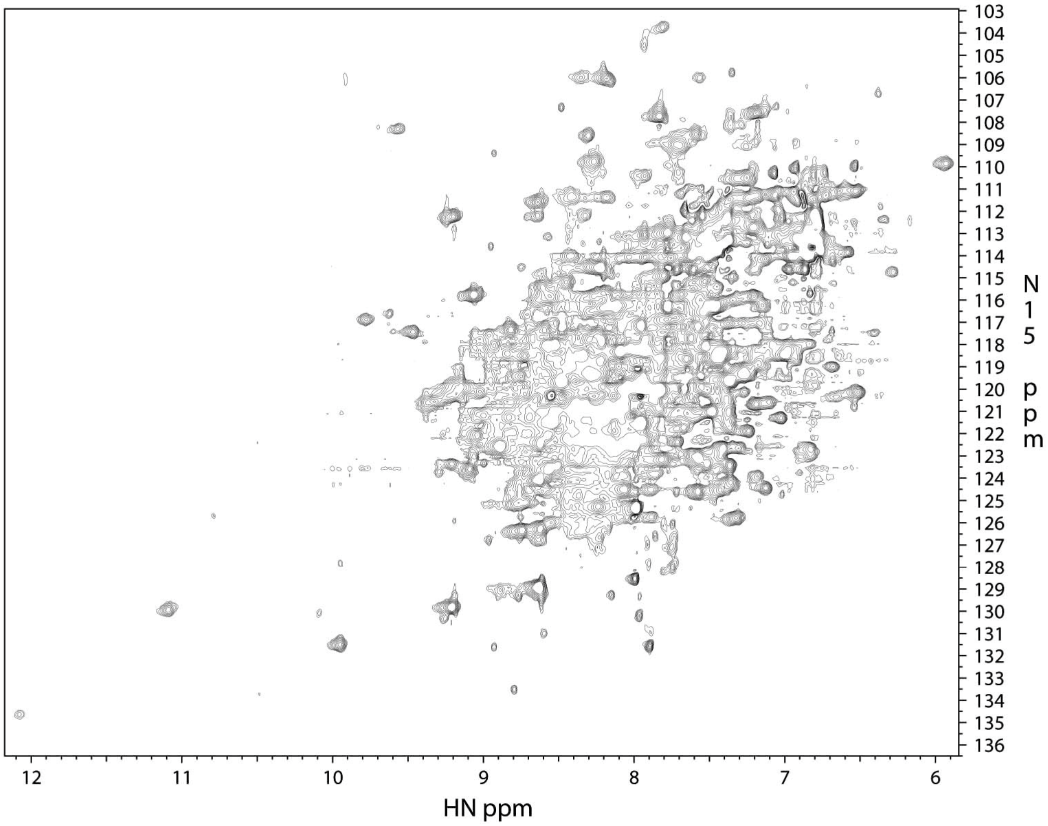

Figure 5.4. ^{1}H-^{15}N HSQC for ^{15}N labeled hFPPS saturated with magnesium, the bisphophonate Zoledronate and pyrophosphate.

5.4. Further experiments on hFPPS.

The next objective in this project consisted in increasing signal resolution of NMR spectra on hFPPS. This was attempted through the implementation of different pulse sequences and also taking advantage of different isotopic labeling schemes. In either case, the goal was to decrease NMR signal broadening in order to improve spectral quality.

When a NMR sample is left in a magnetic field for a long time it achieves "thermal equilibrium". In this state the population of spin systems is governed by the Bolztmann distribution. Also, at thermal equilibrium, all the components of the nuclear magnetic moments located in a plane normal (or transverse) to the applied magnetic field are pointing in random directions. This random distribution of the magnetic moments implies an absence of nuclear spin coherences. The concept of coherence can be intuitively grasped by thinking on the idea of several stopwatches that are started simultaneously at an initial time t_0. At a short period of time after the start, all the clocks will keep registering essentially the same time, they will maintain synchrony and the stopwatch ensemble will virtually keep its initial coherence. At a very long time $t_0+\tau$ there will be differences in the time registered by different stopwatches. This asynchrony is usually due to stochastic processes and the ensemble of stopwatches have lost its initial coherence. Something similar happens to the precessing frequencies of nuclear spins in a sample when certain NMR experiments are performed.

These NMR experiments apply radio frequency pulses that manipulate the spin dynamics of the nuclear magnetic moments in the sample. These pulses usually redistribute populations of spin systems taking them out of the thermal equilibrium. In some cases, these pulses can also create coherences. Coherence is evidenced by a partial alignment of nuclear magnetic moments transverse to the direction of the external magnetic field applied by the spectrometer.

When the pulse sequence for a particular experiment stops, the nuclear spins are usually only under the influence of the external magnetic field generated by the spectrometer's magnet. This makes that the spin system evolves towards a specific thermal equilibrium via their interaction with the molecular environment. The process by which this thermal equilibrium is regained is called relaxation. Relaxation is an important phenomenon in NMR that ultimately defines the intensity and broadening of the signal measured by most of the NMR experiments.

In a group of isolated spin 1/2 particles there are two basic time constants to describe relaxation. The Spin-lattice relaxation time constant, also called longitudinal relaxation time constant, T_1, that measures how fast spin populations move towards thermal equilibrium, and spin-spin relaxation time constant T_2, also known as transverse relaxation time constant, that measures the decay of transverse magnetization.

In the case of spins 1/2, relaxation is caused by small fluctuations in the magnetic fields present at the nuclear spins locations. Thermal motion of the surrounding atoms are the cause of these fluctuations. There are two main causes of these fluctuations in spins 1/2. One cause is dipole-dipole interactions (dipole-dipole coupling) between two nuclear spins in the same molecule. In this case the magnitude and direction of the magnetic field that one spin exerts on the other constantly changes as the molecule tumbles. Another cause of fluctuations in the local magnetic fields is chemical shift anisotropy (CSA). These fluctuating fields are caused by induced molecular electron currents due to the applied external magnetic field. Tumbling of the molecule changes the magnitude and direction of the local magnetic fields causing relaxation. There are also effects in the local fields due to spin-rotation. However, this has a minor effect in the relaxation mechanisms for spins 1/2. For spins 1/2 the dominant relaxation mechanism is dipole-dipole interactions, and at higher applied external magnetic fields, CSA starts to be a competitive cause of relaxation. As the protein tumbles, the induced fields at certain nucleus are modulated leading to relaxation. This is the main mechanism of relaxation via CSA. These induced fields are proportional to the spectrometer external applied magnetic field and the relaxation constants are proportional to the square of the local magnetic fields. As a consequence of this, The CSA relaxation mechanism is proportional to the square of the external magnetic field and becomes competitive with the dipole-dipole relaxation mechanism at the highest comercially available magnetic field (22.3 T). When a system present several correlated mechanisms of relaxation, there are possibilities of cross-relaxation effects. Cross-relaxation effects can be successfully used in some pulse sequences to improve spectral resolution as in the case of Transverse Relaxation Optimized Spectroscopy experiments (TROSY)(228).

With the previous information in mind it was decided to keep studying the interaction between hFPPS and bisphophonates applying different pulse sequences and using certain isotopic labeling schemes. Both scenarios involved strategies that were intended to enhance spectral resolution by improving NMR relaxation properties in the sample.

5.4.1. Lysine methylation of hFPPS.

Fast rotation of methyl groups provide them with long transverse relaxation time constants. This provides them with favorable NMR relaxation properties. These chemical groups usually display well resolved chemical shift dispersions and also show high sensitivity to changes in the surrounding electronic environment. For these reasons, methyls can be an excellent probe to characterize protein binding, folding and kinetics through NMR spectroscopy(229). However, labeling of certain side chain methyl groups using isotopically labeled metabolic precursors is an expensive and time consuming task. There are some alternative labeling techniques that can be used that are relatively faster and inexpensive to implement. One of these techniques is ^{13}C-methyl tagging of lysine residues.

There are 22 lysines in hFPPS that account for around 6% of the enzyme's amino acid composition. They are roughly evenly distributed throughout the protein sequence. This makes them potentially good probes to study protein binding. Lysine methylation of hFPPS was done using a typical methylation reaction described elsewhere(230) (Figure 5.5). Unlabeled hFPPS (300 uM) is dissolved in 0.05 M phosphate, pH 7.5. ^{13}C formalin (aqueous formaldehyde) is added in a proportion equal to the number of reactive amines (N terminal residue and lysines). The solution is briefly mixed and left at room temperature for around 1 hour without stirring. Solid sodium cianoborohydride is then added in fivefold excess and the sample is mixed through several inversions. The sample is left at room temperature for 6 hours and the buffer is exchanged through dialysis.

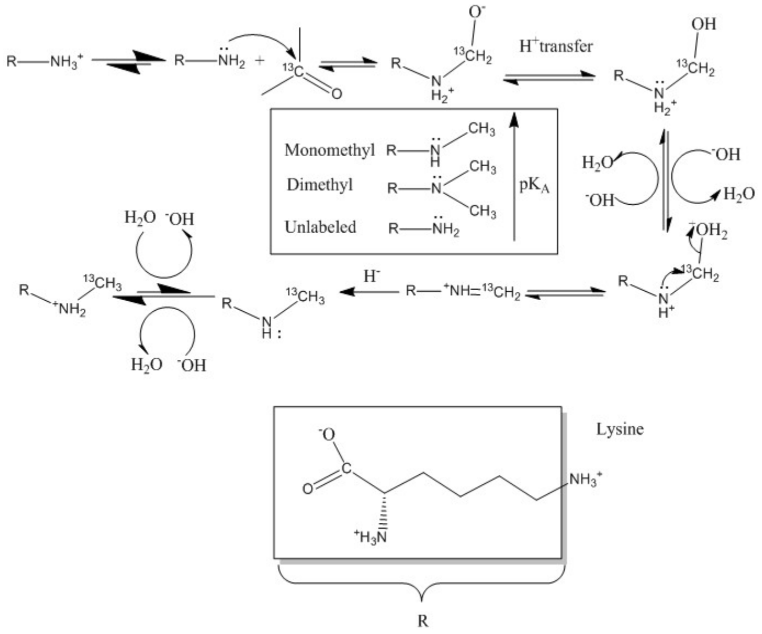

Figure 5.5. Reaction for ^{13}C reductive methylation of lysines. H^- is any hydride donor suitable to reduce the iminium ion to the corresponding secondary (monomethyl) or tertiary amine (dimethyl).

Under these conditions the reaction provides a protein with a ratio close to 1:1 of monomethyl vs dimethyl lysines. Figure 5.6 shows the ^{1}H-^{13}C HSQC spectrum (18.8 Tesla) of ~250 µM lysine ^{13}C methylated hFPPS. There are two regions where mono (signals around 30 p.p.m. in ^{13}C dimension) and dimethyl lysine cross-peaks (signals around 40 p.p.m. in ^{13}C dimension) can be identified. However, signal broadening and cross-peak crowding result in our being unable to resolve the 22 individual lysine signals we expected to see in this experiment.

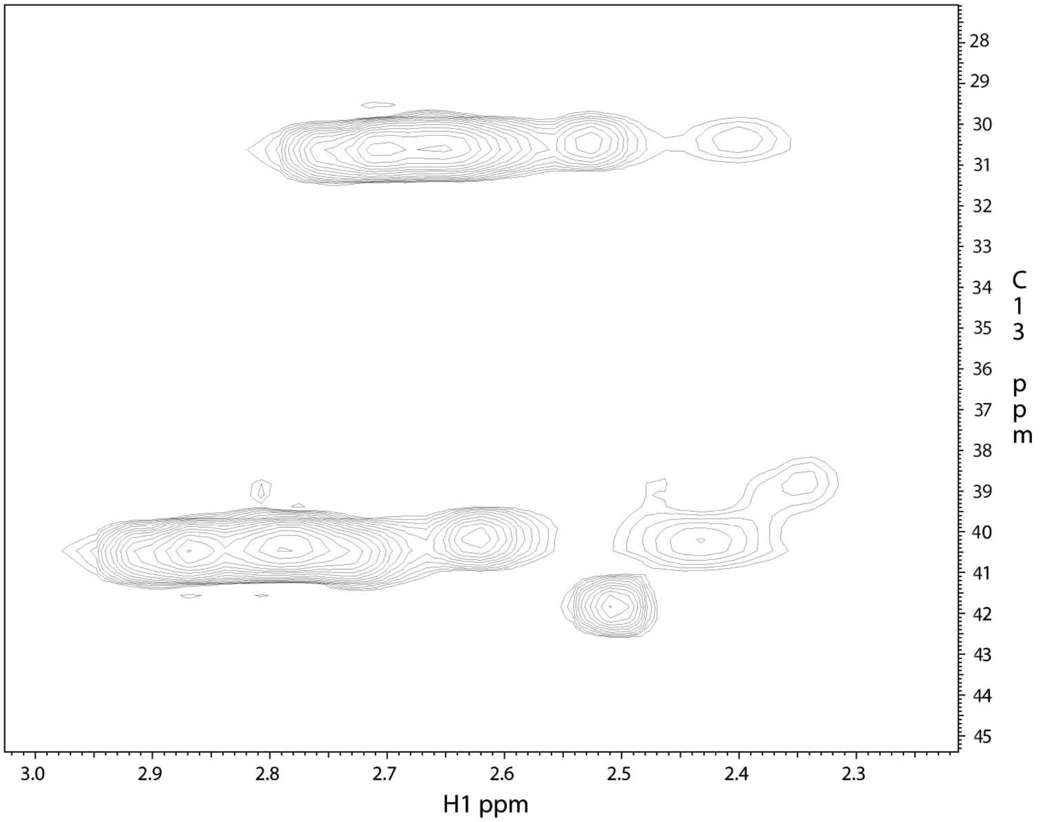

Figure 5.6. ^{1}H-^{13}C HSQC spectrum of hFPPS ^{13}C lysine methylated in the apo state. Mono (cross-peaks around 30 p.p.m. in ^{13}C dimension) and dimethylated regions (cross-peaks around 40 p.p.m. in ^{13}C dimension) are shown.

NMR sample was then saturated with magnesium, Zoledronate and pyrophosphate. However, HSQC spectrum for the saturated sample did not show peaks displacements or any further spectral changes upon addition of the ligands. These can be explained if lysines in hFPPS are not involved in any binding region of the protein with Zoledronate or either they do not suffer substantial conformational change upon binding. This experimental system is therefore not suitable to perform protein binding studies. However, binding of wild-type hFPPS to Zoledronate was confirmed by Isothermal titration calorimetry. Enzymatic activity of the protein was also confirmed by further assays made by an independent lab partner as illustrated in the literature(223).

5.4.2. hFPPS deuteration.

In addition to CSA, dipole-dipole interactions are the most important cause of NMR signal relaxation in spin 1/2 systems. A straightforward way to reduce this specific relaxation is by removing intramolecular dipole-dipole interactions. In our particular case the protein contains ^{1}H,^{15}N,and ^{13}C, nuclei, which are all spin 1/2 particles. Dipole-dipole interactions, transverse relaxation, and thus sensitivity can be increased by reducing the number of these spins in our sample. ^{15}N and ^{13}C atoms do not cause much relaxation given their very small gyromagnetic ratio. However ^{1}H are the most abundand source of relaxation and they can be sometimes replaced with ^{2}H without disrupting protein function or structure(231). However not all ^{1}H nuclei are desired to be removed, some few of them can be kept as NMR reporters in the protein to track protein binding, folding, or any conformational change of interest. ^{1}H atoms are the main source of spins 1/2 in proteins. By selectively replacing some ^{1}H atoms with ^{2}H atoms we can drastically reduce relaxation due to dipole-dipole interactions.

Deuterated hFPPS was expressed in a 90% D_2O M9 medium and purified using the standard procedure. The NMR sample was also labeled with ^{13}C and ^{15}N looking forward to performing possible NMR assignments experiments (experiments that will assign NMR signals to specific atoms in the molecule). The labeling method used generates a randomly deuterated protein sample. During the purification process some deuterons atoms may exchange with hydrogen from the sample buffer. This is the case of the amide bonds. For these reasons ^{1}H-^{15}N HSQC experiments can still be performed on this type of samples.

Figure 5.7 shows a ^{1}H-^{15}N HSQC spectrum (18.8 Tesla) for a partially deuterated sample of hFPPS at 250 uM protein concentration. Compared to the fully ^{1}H-^{15}N isotopically labeled sample of hFPPS, the deuterated hFPPS spectrum shows some improvements. Cross-peak overlap is somewhat reduced and signal resolution is improved. However the intensity of the NMR signal is not high enough to perform any further NMR experiments on binding. The same poor spectral quality was observed on the NMR sample saturated with magnesium, Zoledronate and pyrophosphate (Figure 5.8).

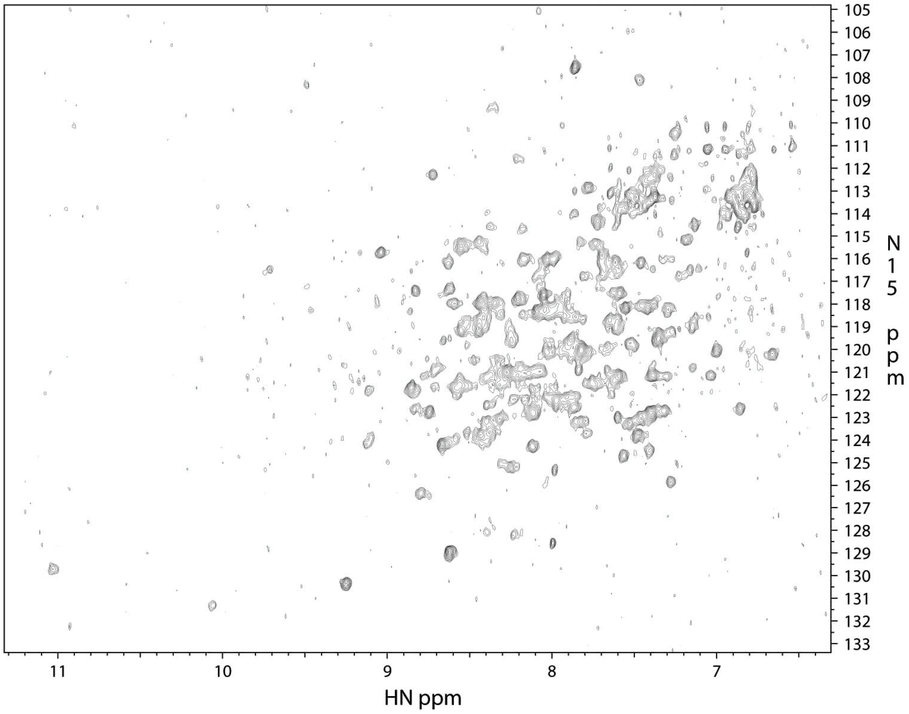

Figure 5.7. ^{1}H-^{15}N HSQC spectrum for a partially deuterated sample of hFPPS.

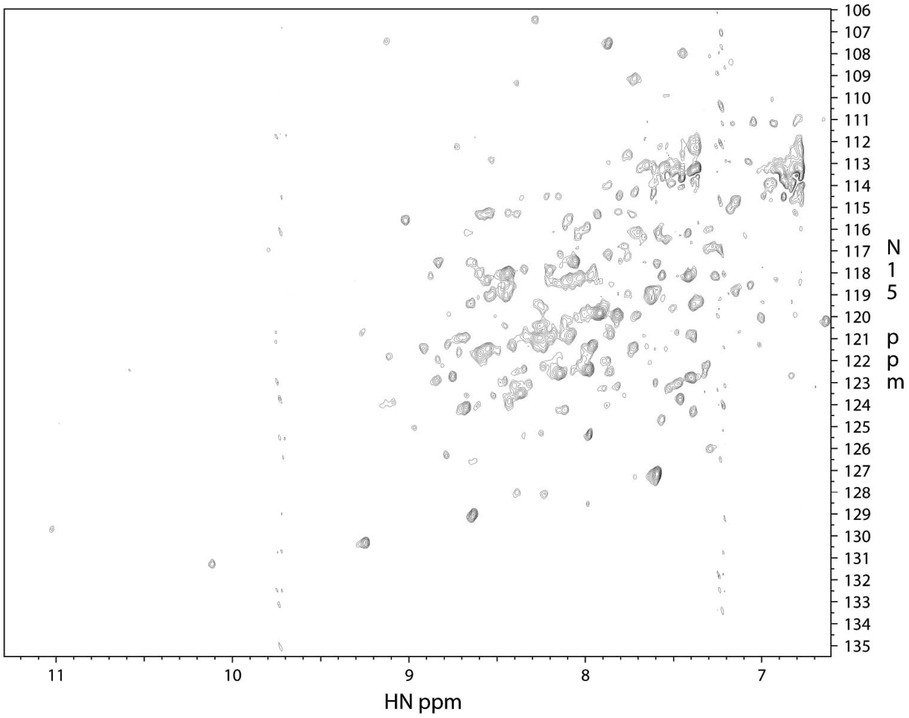

Figure 5.8. ^{1}H-^{15}N HSQC spectrum for a partially deuterated sample of hFPPS saturated with magnesium, Zoledronate and pyrophosphate

5.4.3. hFPPS perdeuteration and ^{1}H-^{13}C labeling of methyl groups on isoleucines, leucines and valines using metabolic precursors

A final step was taken to study the binding of hFPPS to bisphonates using NMR. This final approach included perdeuteration of the protein, selective ^{1}H-^{13}C labeling of methyl groups on Isoleucine, leucine and valine using metabolic precursors and use of NMR experiments that include TROSY pulse sequences.

Perdeuteration implies that every ^{1}H in the protein is replaced by ^{2}H. In order to do this, every nutrient supplied to the E.coli used to express the protein is fully deuterated. Protein perdeuteration strategies are extensively used to study large proteins. Perdeuteration is usually performed concurrently with selective labeling schemes. In this case, selective methylation of hFPPS was achieved using specific isotopic labeled precursors (^{1}H,^{2}H,^{13}C) alpha-ketobutyrate and alpha-ketoisovalarate. The perdeuteration-methyl labeling protocol used here is described elsewhere(232).

A sample of hFPPS containing protons only on the methyl groups of isoleucine (only δ1), leucine ($^{13}CH_3$,$^{12}C^2H_3$) and valine (^{13}CH3,$^{12}C^2H_3$) was expressed, the enzyme was ^{15}N,^{13}C,^{2}H labeled elsewhere. The protein was further purified using and the standard protocol and many or all amide positions were reprotonated to obtain a 300 uM protein concentration sample. Figure 5.5 shows an ^{1}H-^{15}N spectrum TROSY-HSQC experiment (18.8 Tesla) for perdeuterated, methyl labeled hFPPS in the apo state. A TROSY sequence was run in order to increase signal resolution. TROSY pulse sequences take advantage of cross relaxation interplay between spin-spin interactions, and chemical shift anisotropy effects (preferably at high magnetic fields) The experiment then selects NMR signals with desirable slower relaxation rates. TROSY-HSQC pulse sequence used in this experiment is explained elsewhere(228). However, amide cross-peak signals obtained in the spectrum shown in figure 5.9 lack sufficient spectral resolution for further NMR assignment experiments.

Figure 5.10 shows a ^{1}H-^{13}C methyl HMQC experiment (18.8 Tesla) for a 300uM sample of hFPPS in the apo state. This experiment uses TROSY pulse sequences to detect signals from ^{1}H-^{13}C methyl labeled isoleucines, valines and isoleucines present in hFPPS. Spectral resolution and cross-peak intensities are very poor. Ultimately, we were unable to identify individual crosspeaks from labeled methyls on hFPPS.

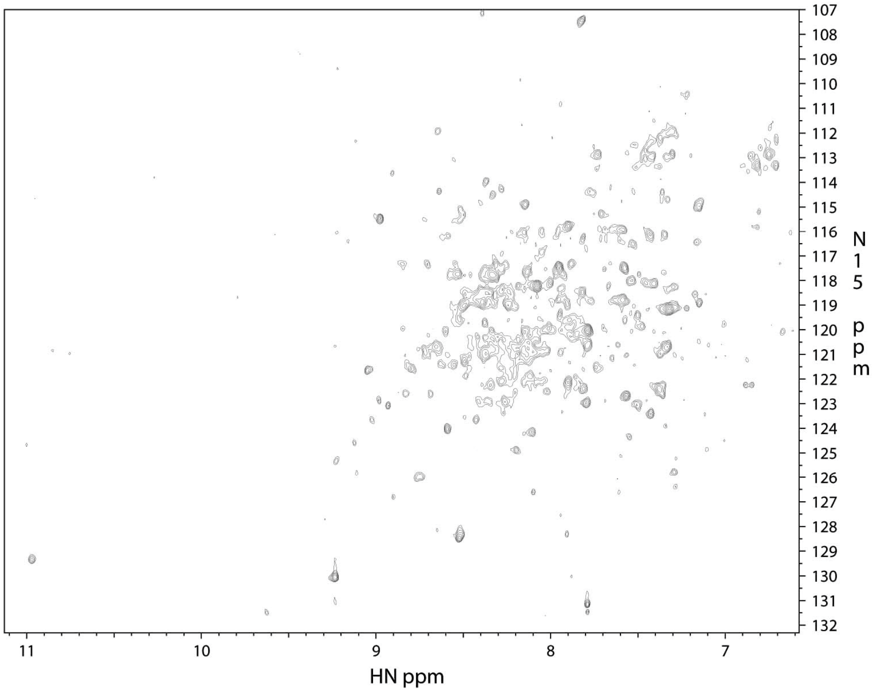

Figure 5.9. ^{1}H-^{15}N spectrum TROSY-HSQC experiment for perdeuterated, methyl labeled hFPPS in the apo state.

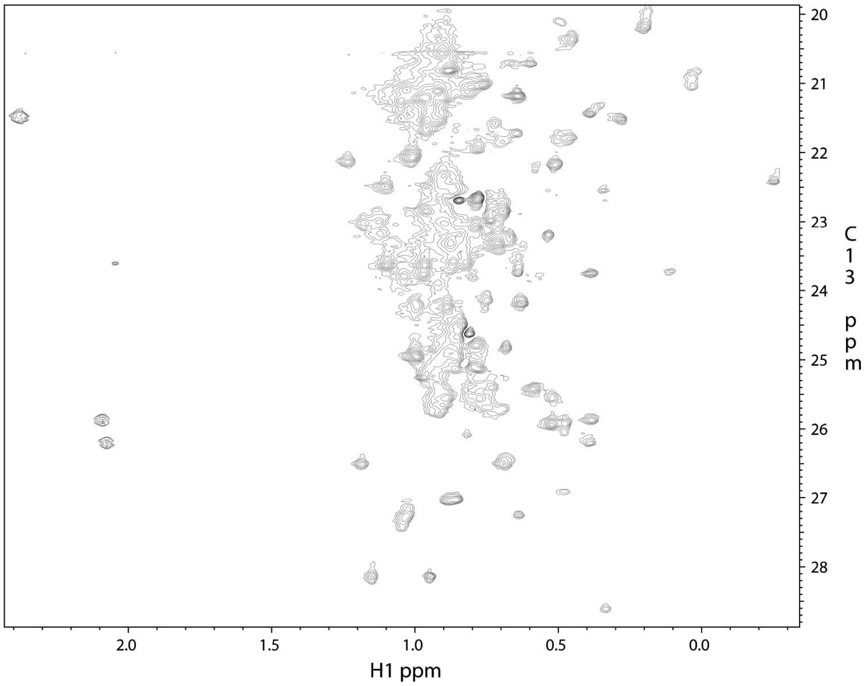

Figure 5.10 shows a ^{1}H-^{13}C methyl HMQC experiment for a 300uM hFPPS in the apo state.

The next step was to determine if labeled methyls in isoleucine (21 a.a.), valine (23 a.a.) and leucines (41 a.a) on hFPPS could be used as probes to measure protein binding dynamics. We performed ^{13}C methyl CPMG transverse relaxation experiments as described elsewhere(233). NMR CPMG experiments were set up to run overnight at 30ºC. However, the sample spectrometer showed extensive aggregation by the end of the experiment that resulted in the loss of more than a half of protein sample. A plot of transverse relaxation vs frequency of refocusing pulses for the labeled methyl signals did not show any indication of protein conformational exchange in the ms-µs time scale.

Perdeuterated hFPPS seems to be unstable under the conditions of the NMR experiment. However a final ^{1}H-^{13}C methyl HMQC experiment (18.8 Tesla) run on a recovered sample of this protein (140 uM protein concentration), saturated with magnesium, Zoledronate an pyrophospate shows well resolved and relatively intense signals to be identified in the spectrum that can be seen on figure 5.11.

All the approaches used so far to hFPPS via NMR have been unsatisfactory. This may lead to conclude that relaxation of the NMR signal for isotopically labeled versions of this protein is high. It is not clear the main source for the signal relaxation. However, this can be due to fast conformational changes for most of the residues of hFPPS even in well known inhibited bound states. Additional directions and suggestions that could be done to study hFPPS via NMR will be given in the final chapter 6 on "further research directions".

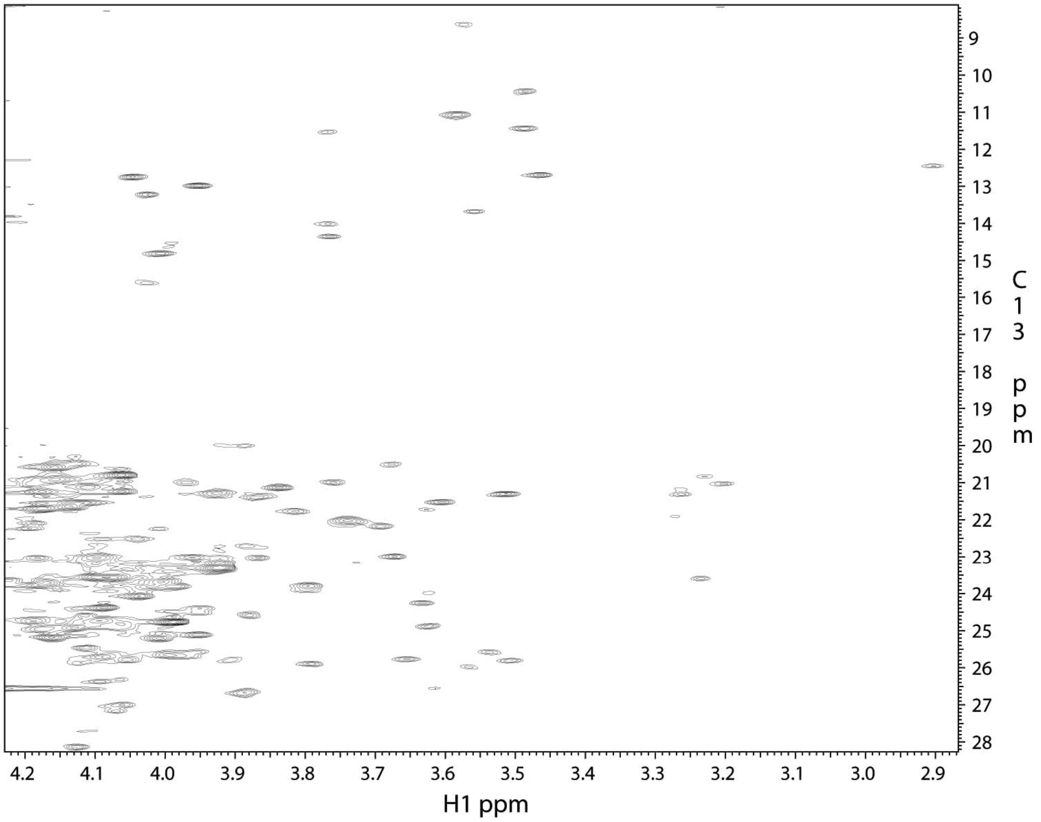

Figure 5.11. ^1H-^{13}C **methyl HMQC experiment of hFPPS perdeuterated and methyl labeled on ILV, saturated with magnesium, Zoledronate and pyrophospate.**

6. Further research directions

6.1. Overview.

The three projects described in this thesis would benefit from further attention. The first is explained in chapter 3. It involves the electrostatic-driven interaction between several proline rich peptides and the chicken isoform of the SH3 domain from the tyrosine kinase Fyn. The second project is described in chapter 4. This section involved mapping the volume changes that occur as the chicken Fyn SH3 domain binds a proline rich peptide. The final project is explained in chapter 5. It describes different approaches that were used to study binding between bisphophonates and human farnesyl pyrophosphate synthase via solution state protein NMR experiments.

6.2. Electrostatic interactions in the binding pathway of a transient protein complex studied by NMR and isothermal titration calorimetry.

It is interesting to understand what controls binding kinetics in protein-protein association. For these reason is important to develop methods to describe quantitatively binding. Electrostatic driven binding between proteins have been usually studied using models where binding partners form tight and stable complexes with lifetimes of hours or days. However many biological processes rely on transiently-formed complexes with lifetimes in the range of milliseconds. For these systems, binding processes driven by electrostatics have not been fully studied. We have shown here that this type of binding process may rely less on electrostatics compared to tight binders. This opens a new area of research in the study of the association processes of weak, transiently-formed complexes. It would be interesting explore which non-electrostatic driving forces (hydrophobic interactions or dipole-dipole interactions) help to accelerate and stabilize the bound complex in weak, transiently-formed systems and the effect on biological systems that depend on these interactions.

In this chapter we studied the interaction between the chicken fyn SH3 domain and a series of proline-rich dodecapeptides. For future studies in this project it would be interesting to study the effects of mutations within the SH3 domain itself on the thermodynamics and kinetics of binding to SS, SR and RR peptide. This would include four protein mutants where residues E98 D99 D100 will be individually replaced by Q98, N99, N100 and a final fourth protein mutant where any charged residue outside the binding pocket (D92, E94, E107, E116, D118, E121 or E129) is replaced by electrostaticaly neutral analog amino acid. This series of experiments will give a broad picture of how the binding process between SH3 domains and proline rich peptides is mediated by electrostatics. More specifically it will show how the specificity binding pocket in the SH3 domain modulates electrostatic binding with proline rich peptides. It would also enable us to dissect specific electrostatic contributions to binding (formation of ion pairs) from non specific electrostatic interactions (long-range interactions between charged residues in the peptide and charged residues on the protein outside the binding pocket).

6.3. Mapping volume changes in the binding pathway of an SH3 domain and a proline rich peptide

In this chapter we were able to measure for the first time the activation volume of a protein-ligand binding process. In addition to the novelty of the measurement, this information can be used to understand changes in the solvent that may drive the association process. In future work, computational models of hydration waters could be of particular interest to understand our experimental results. More specifically, there is an interesting aspect of this project that deserves further experimental work. According to the results shown in chapter 4, the change in volume between the transition state and the bound state is around 4 ml mol^{-1}. It will be interesting to confirm if that change in volume is due to the formation of the hydrogen bond between R_{-4} in the peptide and D99 in the protein. A series of binding and kinetic experiments at different pressures between fyn SH3 domain and SS peptide would easily help to confirm or reject this hypothesis. According to NMR titrations it is highly probable that SS peptide and SR peptide bind in the same orientation on the SH3 domain. SR peptide makes a unique hydrogen-bonded ion pair in the binding pocket with the SH3 domain, while the SS peptide, which lacks charged residues, is not able to do so. Thus the difference in volume between the bound state of the SH3-SS peptide system and the SH3-SR peptide system should lead to a value close to the volume for the formation of the hydrogen bond formed between R_{-4} in the peptide and D100 in the protein (around 4 mL/mol). This approach is complicated by the fact that that SS and SR peptides likely have different solvation properties in the free state.

6.4. NMR experimental approaches to study binding of bisphophonates to human Farnesyl Pyrophosphate Synthase (hFPPS).

Unfortunately, this project did not provide publishable results. However it would be valuable to screen different solution conditions to improve the protein stability of perdeuterated hFPPS. The composition of the NMR buffer would be varied by adjusting the ionic strength, pH and viscosity. This screening can be done using techniques such as differential scanning fluorimetry(234). This technique helps to identify small molecule ligands that stabilize purified proteins. The melting temperature of the protein is measured following the change in fluorescence of a dye that has affinity for exposed hydrophobic regions of the protein. Screening of buffers with different pHs, viscosities (i.e., adding glycerol) or salts may help to improve protein stability. Another option would be to try chemical screening methods to identify ligands other than bisphophonates that promote hFPPS stability(235). After finding a suitable range of buffer conditions for the protein, the binding of a series of different ligands to hFPPS can be characterized. These include the recently discovered allosteric non-bisphophonate inhibitors of hFPPS(236). Using differential scanning calorimetry together with intrinsic binding fluorescence experiments may help to identify ligand that stabilize the bound complex.

References

1. Newton, A. C. (1995) Protein kinase C: structure, function, and regulation. *J Biol Chem* **270**, 28495-28498
2. Kristiansen, K. (2004) Molecular mechanisms of ligand binding, signaling, and regulation within the superfamily of G-protein-coupled receptors: molecular modeling and mutagenesis approaches to receptor structure and function. *Pharmacol Therapeut* **103**, 21-80
3. Freiburger, L. A., Baettig, O. M., Sprules, T., Berghuis, A. M., Auclair, K., and Mittermaier, A. K. (2011) Competing allosteric mechanisms modulate substrate binding in a dimeric enzyme. *Nature Structural & Molecular Biology* **18**, 288-U270
4. Schramm, V. L. (2007) Enzymatic transition state theory and transition state analogue design. *J Biol Chem* **282**, 28297-28300
5. Qi, S. Y., Groves, J. T., and Chakraborty, A. K. (2001) Synaptic pattern formation during cellular recognition. *P Natl Acad Sci USA* **98**, 6548-6553
6. Hu, J. M., Toft, D. O., and Seeger, C. (1997) Hepadnavirus assembly and reverse transcription require a multi-component chaperone complex which is incorporated into nucleocapsids. *Embo J* **16**, 59-68
7. Miller, D. W., and Dill, K. A. (1997) Ligand binding to proteins: The binding landscape model. *Protein Science* **6**, 2166-2179
8. Camacho, C. J., Gatchell, D. W., Kimura, S. R., and Vajda, S. (2000) Scoring docked conformations generated by rigid-body protein-protein docking. *Proteins* **40**, 525-537
9. Mobley, D. L., and Dill, K. A. (2009) Binding of small-molecule ligands to proteins: "what you see" is not always "what you get". *Structure* **17**, 489-498
10. Macomber, R. S. (1992) An Introduction to Nmr Titration for Studying Rapid Reversible Complexation. *Journal of Chemical Education* **69**, 375-378
11. Tsai, C. J., Kumar, S., Ma, B. Y., and Nussinov, R. (1999) Folding funnels, binding funnels, and protein function. *Protein Science* **8**, 1181-1190
12. Mulder, F. A. A., Mittermaier, A., Hon, B., Dahlquist, F. W., and Kay, L. E. (2001) Studying excited states of proteins by NMR spectroscopy. *Nat. Struct. Biol.* **8**, 932-935
13. McQuarrie, D. A., and Simon, J. D. (1997) *Physical chemistry : a molecular approach*, University Science Books, Sausalito, Calif.
14. Cantor, C. R., and Schimmel, P. R. (1980) *The behavior of biological macromolecules*, W. H. Freeman, San Francisco
15. Pilling, M. J., and Seakins, P. W. (1995) *Reaction kinetics*, Oxford University Press, Oxford ; New York
16. Berg, O. G., and Vonhippel, P. H. (1985) Diffusion-controlled macromolecular interactions. *Annual Review of Biophysics and Biophysical Chemistry* **14**, 131-160
17. Smoluchowski, M. (1917) Versuch einer mathematischen theorie der koagulationskinetik kolloider losungen. *Z. Phys. Chem.* **92**, 129-168
18. Zhou, H. X. (2010) Rate theories for biologists. *Q Rev Biophys* **43**, 219-293
19. Ubbink, M. (2009) The courtship of proteins: Understanding the encounter complex. *Febs Lett* **583**, 1060-1066
20. Janin, J. (1997) The kinetics of protein-protein recognition. *Proteins Struct. Funct. Gen.* **28**, 153-161
21. Kahn, D. S. (1949) The Activated Complex of the Protein Molecule. *J Phys Colloid Chem* **53**, 977-996

22. Schramm, V. L. (1998) Enzymatic transition states and transition state analog design. *Annu Rev Biochem* **67**, 693-720
23. Hoff, J. H. v. t. (1884) *Études de dynamique chimique*, Muller, Amsterdam,
24. Arrhenius, S. (1889) *Über die Reaktionsgeschwindigkeit bei der Inversion von Rohrzucker durch Säuren*, Wilhelm Engelmann
25. Einstein, A., Fürth, R., and Cowper, A. D. (1926) *Investigations on the theory of the Brownian movement*, Methuen & Co. ltd., London,
26. Van't Hoff, J. W. (1887) Die Rolle des osmotischen Druckes in der Analogie zwischen Lösungen und Gasen. *Z. physik. Chemie* **1**, 481-493
27. Bird, R. B., Stewart, W. E., and Lightfoot, E. N. (2002) *Transport phenomena*, 2nd, Wiley international ed., J. Wiley, New York
28. Tellinghuisen, J. (2004) Statistical error in isothermal titration calorimetry. *Methods Enzymol* **383**, 245-282
29. Lakowicz, J. R. (2006) *Principles of fluorescence spectroscopy*, 3rd ed., Springer, New York
30. Hansen, S. B., Radic, Z., Talley, T. T., Molles, B. E., Deerinck, T., Tsigelny, I., and Taylor, P. (2002) Tryptophan fluorescence reveals conformational changes in the acetylcholine binding protein. *Journal of Biological Chemistry* **277**, 41299-41302
31. Musacchio, A., Wilmanns, M., and Saraste, M. (1994) Structure and Function of the Sh3 Domain. *Prog Biophys Mol Bio* **61**, 283-297
32. Ding, V. D. H., Sheares, B. T., Bergstrom, J. D., Ponpipom, M. M., Perez, L. B., and Poulter, C. D. (1991) Purification and Characterization of Recombinant Human Farnesyl Diphosphate Synthase Expressed in Escherichia-Coli. *Biochem J* **275**, 61-65
33. Seet, B. T., Dikic, I., Zhou, M. M., and Pawson, T. (2006) Reading protein modifications with interaction domains. *Nat Rev Mol Cell Bio* **7**, 473-483
34. Zarrinpar, A., Bhattacharyya, R. P., and Lim, W. A. (2003) The structure and function of proline recognition domains. *Sci STKE* **2003**, RE8
35. Musacchio, A., Noble, M., Pauptit, R., Wierenga, R., and Saraste, M. (1992) Crystal-Structure of a Src-Homology-3 (Sh3) Domain. *Nature* **359**, 851-855
36. Adzhubei, A. A., Sternberg, M. J. E., and Makarov, A. A. (2013) Polyproline-II Helix in Proteins: Structure and Function. *Journal of Molecular Biology* **425**, 2100-2132
37. Li, S. S. C. (2005) Specificity and versatility of SH3 and other proline-recognition domains: structural basis and implications for cellular signal transduction. *Biochem J* **390**, 641-653
38. Holt, M. R., and Koffer, A. (2001) Cell motility: proline-rich proteins promote protrusions. *Trends Cell Biol* **11**, 38-46
39. Macarthur, M. W., and Thornton, J. M. (1991) Influence of Proline Residues on Protein Conformation. *J Mol Biol* **218**, 397-412
40. Agrawal, V., and Kishan, K. V. R. (2002) Promiscuous binding nature of SH3 domains to their target proteins. *Protein Peptide Lett* **9**, 185-193
41. Wilkin, D. J., Kutsunai, S. Y., and Edwards, P. A. (1990) Isolation and Sequence of the Human Farnesyl Pyrophosphate Synthetase Cdna - Coordinate Regulation of the Messenger-Rnas for Farnesyl Pyrophosphate Synthetase, 3-Hydroxy-3-Methylglutaryl Coenzyme-a Reductase, and 3-Hydroxy-3-Methylglutaryl Coenzyme-a Synthase by Phorbol Ester. *Journal of Biological Chemistry* **265**, 4607-4614
42. Liang, P. H., Ko, T. P., and Wang, A. H. J. (2002) Structure, mechanism and function of prenyltransferases. *Eur J Biochem* **269**, 3339-3354

43. Buhaescu, I., and Izzedine, H. (2007) Mevalonate pathway: A review of clinical and therapeutical implications. *Clin Biochem* **40**, 575-584

44. Pfeffer, S., and Aivazian, D. (2004) Targeting RAB GTPases to distinct membrane compartments. *Nat Rev Mol Cell Bio* **5**, 886-896

45. Berzat, A. C., Brady, D. C., Fiordalisi, J. J., and Cox, A. D. (2006) Using inhibitors of prenylation to block localization and transforming activity. *Method Enzymol* **407**, 575-597

46. Yeganeh, B., Wiechec, E., Ande, S. R., Sharma, P., Moghadam, A. R., Post, M., Freed, D. H., Hashemi, M., Shojaei, S., Zeki, A. A., and Ghavami, S. (2014) Targeting the mevalonate cascade as a new therapeutic approach in heart disease, cancer and pulmonary disease. *Pharmacol Therapeut* **143**, 87-110

47. Luckman, S. P., Hughes, D. E., Coxon, F. P., Russell, R. G. G., and Rogers, M. J. (1998) Nitrogen-containing bisphosphonates inhibit the mevalonate pathway and prevent post-translational prenylation of GTP-binding proteins, including Ras. *J Bone Miner Res* **13**, 581-589

48. Drake, M. T., Clarke, B. L., and Khosla, S. (2008) Bisphosphonates: Mechanism of action and role in clinical practice. *Mayo Clin Proc* **83**, 1032-1045

49. Coleman, R. (2011) The use of bisphosphonates in cancer treatment. *Ann Ny Acad Sci* **1218**, 3-14

50. Kavanagh, K. L., Guo, K. D., Dunford, J. E., Wu, X. Q., Knapp, S., Ebetino, F. H., Rogers, M. J., Russell, R. G. G., and Oppermann, U. (2006) The molecular mechanism of nitrogen-containing bisphosphonates as anti osteoporosis drugs. *Proceedings of the National Academy of Sciences of the United States of America* **103**, 7829-7834

51. Hosfield, D. J., Zhang, Y. M., Dougan, D. R., Broun, A., Tari, L. W., Swanson, R. V., and Finn, J. (2004) Structural basis for bisphosphonate-mediated inhibition of isoprenoid biosynthesis. *Journal of Biological Chemistry* **279**, 8526-8529

52. Cavanagh, J. (1996) *Protein NMR spectroscopy: Principles and practice*, Academic Press, San Diego

53. Mittermaier, A., and Kay, L. E. (2006) New tools provide new insights in NMR studies of protein dynamics. *Science* **312**, 224-228

54. Ikura, M., Clore, G. M., Gronenborn, A. M., Zhu, G., Klee, C. B., and Bax, A. (1992) Solution structure of a calmodulin-target peptide complex by multidimensional NMR. *Science* **256**, 632-638

55. Walters, K. J., Ferentz, A. E., Hare, B. J., Hidalgo, P., Jasanoff, A., Matsuo, H., and Wagner, G. (2001) Characterizing protein-protein complexes and oligomers by nuclear magnetic resonance spectroscopy. *Nuclear Magnetic Resonance of Biological Macromolecules, Pt B* **339**, 238-258

56. Jung, Y. S., Cai, M. L., and Clore, G. M. (2010) Solution Structure of the IIA(Chitobiose)-IIBChitobiose Complex of the N,N '-Diacetylchitobiose Branch of the Escherichia coli Phosphotransferase System. *Journal of Biological Chemistry* **285**, 4173-4184

57. Finerty, P. J., Mittermaier, A. K., Muhandiram, R., Kay, L. E., and Forman-Kay, J. D. (2005) NMR dynamics-derived insights into the binding properties of a peptide interacting with an SH2 domain. *Biochemistry* **44**, 694-703

58. Boehr, D. D., McElheny, D., Dyson, H. J., and Wright, P. E. (2006) The dynamic energy landscape of dihydrofolate reductase catalysis. *Science* **313**, 1638-1642

59. Sugase, K., Dyson, H. J., and Wright, P. E. (2007) Mechanism of coupled folding and binding of an intrinsically disordered protein. *Nature* **447**, 1021-U1011

60. Iwahara, J., and Clore, G. M. (2006) Detecting transient intermediates in macromolecular binding by paramagnetic NMR. *Nature* **440**, 1227-1230
61. Meyer, B., and Peters, T. (2003) NMR spectroscopy techniques for screening and identifying ligand binding to protein receptors. *Angew Chem Int Ed Engl* **42**, 864-890
62. Shuker, S. B., Hajduk, P. J., Meadows, R. P., and Fesik, S. W. (1996) Discovering high-affinity ligands for proteins: SAR by NMR. *Science* **274**, 1531-1534
63. Zarrine-Afsar, A., Mittermaier, A., Kay, L. E., and Davidson, A. R. (2006) Protein stabilization by specific binding of guanidinium to a functional arginine-binding surface on an SH3 domain. *Protein Science* **15**, 162-170
64. Chen, Y., Reizer, J., Saier, M. H., Fairbrother, W. J., and Wright, P. E. (1993) Mapping of the binding interfaces of the proteins of the bacterial phosphotransferase system, HPr and IIA^{glc}. *Biochemistry* **32**, 32-37
65. Liu, Z. H., Sun, C. H., Olejniczak, E. T., Meadows, R. P., Betz, S. F., Oost, T., Herrmann, J., Wu, J. C., and Fesik, S. W. (2000) Structural basis for binding of Smac/DIABLO to the XIAP BIR3 domain. *Nature* **408**, 1004-1008
66. Demers, J. P., and Mittermaier, A. (2009) Binding Mechanism of an SH3 Domain Studied by NMR and ITC. *Journal of the American Chemical Society* **131**, 4355-4367
67. Schuck, P. (1996) Kinetics of ligand binding to receptor immobilized in a polymer matrix, as detected with an evanescent wave biosensor .1. A computer simulation of the influence of mass transport. *Biophysical J.* **70**, 1230-1249
68. Tochtrop, G. P., Richter, K., Tang, C., Toner, J. J., Covey, D. F., and Cistola, D. P. (2002) Energetics by NMR: site-specific binding in a positively cooperative system. *Proc. Natl. Acad. Sci. U.S.A.* **99**, 1847-1852
69. Tugarinov, V., Choy, W. Y., Orekhov, V. Y., and Kay, L. E. (2005) Solution NMR-derived global fold of a monomeric 82-kDa enzyme. *Proceedings of the National Academy of Sciences of the United States of America* **102**, 622-627
70. Bodenhausen, G., and Ruben, D. J. (1980) Natural abundance nitrogen-15 NMR by enhanced heteronuclear spectroscopy. *Chemical Physics Letters* **69**, 185-189
71. Loria, J. P., Rance, M., and Palmer, A. G. (1999) A relaxation-compensated Carr-Purcell-Meiboom-Gill sequence for characterizing chemical exchange by NMR spectroscopy. *Journal of the American Chemical Society* **121**, 2331-2332
72. Farrow, N. A., Zhang, O., Forman-Kay, J. D., and Kay, L. E. (1994) A heteronuclear correlation experiment for simultaneous determination of ^{15}N longitudinal decay and chemical exchange rates of systems in slow equilibrium. *J. Biomol. NMR* **4**, 727-734
73. Renzoni, D. A., Pugh, D. J. R., Siligardi, G., Das, P., Morton, C. J., Rossi, C., Waterfield, M. D., Campbell, I. D., and Ladbury, J. E. (1996) Structural and thermodynamic characterization of the interaction of the SH3 domain from Fyn with the proline-rich binding site on the p85 subunit of PI3-kinase. *Biochemistry* **35**, 15646-15653
74. Gardner, K. H., and Kay, L. E. (1998) The use of ^{2}H, ^{13}C, ^{15}N multidimensional NMR to study the structure and dynamics of proteins. *Annu. Rev. Biophys. Biomol. Struct.* **27**, 357-406
75. Marley, J., Lu, M., and Bracken, C. (2001) A method for efficient isotopic labeling of recombinant proteins. *J Biomol NMR* **20**, 71-75
76. Bai, Y. W., Milne, J. S., Mayne, L., and Englander, S. W. (1993) Primary structure effects on peptide group hydrogen exchange. *Proteins-Structure Function and Genetics* **17**, 75-86

77. Sugase, K., Lansing, J. C., Dyson, H. J., and Wright, P. E. (2007) Tailoring relaxation dispersion experiments for fast-associating protein complexes. *Journal of the American Chemical Society* **129**, 13406-+
78. Johnson, B. A., and Blevins, R. A. (1994) NMR View - A computer program for the visualization and analysis of NMR data. *Journal of Biomolecular Nmr* **4**, 603-614
79. van Beek, J. D. (2007) matNMR: A flexible toolbox for processing, analyzing and visualizing magnetic resonance data in Matlab((R)). *Journal of Magnetic Resonance* **187**, 19-26
80. Vranken, W. F., Boucher, W., Stevens, T. J., Fogh, R. H., Pajon, A., Llinas, P., Ulrich, E. L., Markley, J. L., Ionides, J., and Laue, E. D. (2005) The CCPN data model for NMR spectroscopy: Development of a software pipeline. *Proteins-Structure Function and Bioinformatics* **59**, 687-696
81. Gunther, U. L., Ludwig, C., and Ruterjans, H. (2000) NMRLAB - Advanced NMR data processing in MATLAB. *Journal of Magnetic Resonance* **145**, 201-208
82. Delaglio, F., Grzesiek, S., Vuister, G. W., Zhu, G., Pfeifer, J., and Bax, A. (1995) NMRPipe: a multidimensional spectral processing system based on UNIX pipes. *J. Biomol. NMR* **6**, 277-293
83. Gunther, U. L., and Schaffhausen, B. (2002) NMRKIN: Simulating line shapes from two-dimensional spectra of proteins upon ligand binding. *Journal of Biomolecular Nmr* **22**, 201-209
84. Vetterling, W. T., Press, W. H., Teukolsky, S. A., and Flannery, B. R. (1988) *Numerical Recipes in C*, Cambridge University Press, Cambridge
85. Langmuir, I. (1916) The constitution and fundamental properties of solids and liquids Part I Solids. *Journal of the American Chemical Society* **38**, 2221-2295
86. Wiseman, T., Williston, S., Brandts, J. F., and Lin, L. N. (1989) Rapid measurement of binding constants and heats of binding using a new titration calorimeter. *Analytical Biochemistry* **179**, 131-137
87. Gutowsky, H. S., and Saika, A. (1953) Dissociation, chemical exchange, and the proton magnetic resonance in some aqueous electrolytes. *Journal of Chemical Physics* **21**, 1688-1694
88. McConnell, H. M. (1958) Reaction rates by Nuclear Magnetic Resonance. *Journal of Chemical Physics* **28**, 430-431
89. Rogers, M. T., and Woodbrey, J. C. (1962) Proton magnetic resonance study of hindered internal rotation in some substituted N,N-dimethylamides. *Journal of Physical Chemistry* **66**, 540-&
90. Gupta, R. K., Pitner, T. P., and Wasylishen, R. (1974) Fourier transform NMR of exchanging chemical systems. *Journal of Magnetic Resonance* **13**, 383-385
91. Mittag, T., Schaffhausen, B., and Gunther, U. L. (2004) Tracing kinetic intermediates during ligand binding. *Journal of the American Chemical Society* **126**, 9017-9023
92. Carr, H. Y., and Purcell, E. M. (1954) Effects of diffusion on free precession in nuclear magnetic resonance experiments. *Physical Review* **94**, 630-638
93. Meiboom, S., and Gill, D. (1958) Modified spin echo method for measureing nuclear relaxation times. *Review of Scientific Instruments* **29**, 688-691
94. Palmer, A. G., Kroenke, C. D., and Loria, J. P. (2001) Nuclear magnetic resonance methods for quantifying microsecond-to-millisecond motions in biological macromolecules. *Nuclear Magnetic Resonance of Biological Macromolecules, Pt B* **339**, 204-238

95. Korzhnev, D. M., and Kay, L. E. (2008) Probing invisible, low-populated states of protein molecules by relaxation dispersion NMR spectroscopy: An application to protein folding. *Accounts of Chemical Research* **41**, 442-451

96. Hahn, E. L. (1950) Spin Echoes. *Physical Review* **80**, 580

97. Esadze, A., Li, D. W., Wang, T. Z., Bruschweiler, R., and Iwahara, J. (2011) Dynamics of Lysine Side-Chain Amino Groups in a Protein Studied by Heteronuclear H-1-N-15 NMR Spectroscopy. *Journal of the American Chemical Society* **133**, 909-919

98. Ishima, R., Baber, J., Louis, J. M., and Torchia, D. A. (2004) Carbonyl carbon transverse relaxation dispersion measurements and ms-mu s timescale motion in a protein hydrogen bond network. *Journal of Biomolecular Nmr* **29**, 187-198

99. Ishima, R., and Torchia, D. A. (2003) Extending the range of amide proton relaxation dispersion experiments in proteins using a constant-time relaxation-compensated CPMG approach. *Journal of Biomolecular Nmr* **25**, 243-248

100. Korzhnev, D. M., Neudecker, P., Mittermaier, A., Orekhov, V. Y., and Kay, L. E. (2005) Multiple-site exchange in proteins studied with a suite of six NMR relaxation dispersion experiments: An application to the folding of a Fyn SH3 domain mutant. *Journal of the American Chemical Society* **127**, 15602-15611

101. Mulder, F. A. A., Skrynnikov, N. R., Hon, B., Dahlquist, F. W., and Kay, L. E. (2001) Measurement of slow (mu s-ms) time scale dynamics in protein side chains by N-15 relaxation dispersion NMR spectroscopy: Application to Asn and Gln residues in a cavity mutant of T4 lysozyme. *Journal of the American Chemical Society* **123**, 967-975

102. Skrynnikov, N. R., Mulder, F. A. A., Hon, B., Dahlquist, F. W., and Kay, L. E. (2001) Probing slow time scale dynamics at methyl-containing side chains in proteins by relaxation dispersion NMR measurements: Application to methionine residues in a cavity mutant of T4 lysozyme. *Journal of the American Chemical Society* **123**, 4556-4566

103. Lundstrom, P., Lin, H., and Kay, L. E. (2009) Measuring C-13(beta) chemical shifts of invisible excited states in proteins by relaxation dispersion NMR spectroscopy. *Journal of Biomolecular Nmr* **44**, 139-155

104. Baldwin, A. J., Hansen, D. F., Vallurupalli, P., and Kay, L. E. (2009) Measurement of Methyl Axis Orientations in Invisible, Excited States of Proteins by Relaxation Dispersion NMR Spectroscopy. *Journal of the American Chemical Society* **131**, 11939-11948

105. Hansen, D. F., Vallurupalli, P., and Kay, L. E. (2009) Measurement of Methyl Group Motional Parameters of Invisible, Excited Protein States by NMR Spectroscopy. *Journal of the American Chemical Society* **131**, 12745-12754

106. Vallurupalli, P., Hansen, D. F., Stollar, E., Meirovitch, E., and Kay, L. E. (2007) Measurement of bond vector orientations in invisible excited states of proteins. *Proceedings of the National Academy of Sciences of the United States of America* **104**, 18473-18477

107. Palmer, A. G., and Massi, F. (2006) Characterization of the dynamics of biomacromolecules using rotating-frame spin relaxation NMR spectroscopy. *Chemical Reviews* **106**, 1700-1719

108. Hansen, D. F., Vallurupalli, P., and Kay, L. E. (2008) An improved N-15 relaxation dispersion experiment for the measurement of millisecond time-scale dynamics in proteins. *Journal of Physical Chemistry B* **112**, 5898-5904

109. Ishima, R., and Torchia, D. A. (2006) Accuracy of optimized chemical-exchange parameters derived by fitting CPMG R_2 dispersion profiles when $R_2(0a) = R_2(0b)$. *Journal of Biomolecular NMR* **34**, 209-219

110. Korzhnev, D. M., Salvatella, X., Vendruscolo, M., Di Nardo, A. A., Davidson, A. R., Dobson, C. M., and Kay, L. E. (2004) Low-populated folding intermediates of Fyn SH3 characterized by relaxation dispersion NMR. *Nature* **430**, 586-590

111. Carver, J. P., and Richards, R. E. (1972) General 2-site solution for chemical exchange produced dependence of T_2 upon Carr-Purcell pulse separation. *Journal of Magnetic Resonance* **6**, 89-&

112. Davis, D. G., Perlman, M. E., and London, R. E. (1994) Direct measurements of the dissociation rate constant for inhibitor enzyme complexes via the T1rho and T2(CPMG) methods. *Journal of Magnetic Resonance Series B* **104**, 266-275

113. Luz, Z., and Meiboom, S. (1963) Nuclear Magnetic Resonance Study of Protolysis of Trimethylammonium Ion in Aqueous Solution - Order of Reaction with Respect to Solvent. *Journal of Chemical Physics* **39**, 366-&

114. Kovrigin, E. L., Kempf, J. G., Grey, M. J., and Loria, J. P. (2006) Faithful estimation of dynamics parameters from CPMG relaxation dispersion measurements. *Journal of Magnetic Resonance* **180**, 93-104

115. Millet, O., Loria, J. P., Kroenke, C. D., Pons, M., and Palmer, A. G. (2000) The static magnetic field dependence of chemical exchange linebroadening defines the NMR chemical shift time scale. *J. Am. Chem. Soc.* **122**, 2867-2877

116. Mulder, F. A. A., Mittermaier, A., Hon, B., Dahlquist, F. W., and Kay, L. E. (2001) Studying excited states of proteins by NMR spectroscopy. *Nature Structural Biology* **8**, 932-935

117. Amman, C., Meier, P., and Merbach, A. E. (1982) A simple multinuclear NMR thermometer. *Journal of Magnetic Resonance* **46**, 319-321

118. Findeisen, M., Brand, T., and Berger, S. (2007) A 1H-NMR thermometer suitable for cryoprobes. *Magnetic resonance in chemistry : MRC* **45**, 175-178

119. Hindman, J. C. (1966) Proton resonance shift of water in gas and liquid states. *Journal of Chemical Physics* **44**, 4582-&

120. Radic, Z., Kirchhoff, P. D., Quinn, D. M., McCammon, J. A., and Taylor, P. (1997) Electrostatic influence on the kinetics of ligand binding to acetylcholinesterase. Distinctions between active center ligands and fasciculin. *J. Biol. Chem.* **272**, 23265-23277

121. Foote, J., and Milstein, C. (1991) Kinetic maturation of an immune response. *Nature* **352**, 530-532

122. Wang, Y. H., Shen, B. J., and Sebald, W. (1997) A mixed-charge pair in human interleukin 4 dominates high-affinity interaction with the receptor alpha chain. *Proc. Natl. Acad. Sci. USA* **94**, 1657-1662

123. Jucovic, M., and Hartley, R. W. (1996) Protein-protein interaction: A genetic selection for compensating mutations at the barnase-barstar interface. *Proc. Natl. Acad. Sci. USA* **93**, 2343-2347

124. Schreiber, G., and Fersht, A. R. (1996) Rapid, electrostatically assisted association of proteins. *Nat. Struct. Biol.* **3**, 427-431

125. Zhou, H. X. (1997) Enhancement of protein-protein association rate by interaction potential: accuracy of prediction based on local Boltzmann factor. *Biophys. J.* **73**, 2441-2445

126. Northrup, S. H., and Erickson, H. P. (1992) Kinetics of protein-protein association explained by Brownian dynamics computer simulation. *Proc. Natl. Acad. Sci. USA* **89**, 3338-3342

127. Gabdoulline, R. R., and Wade, R. C. (2002) Biomolecular diffusional association. *Curr. Op. Struct. Biol.* **12**, 204-213

128. Wallis, R., Moore, G. R., James, R., and Kleanthous, C. (1995) Protein-Protein Interactions in Colicin E9 Dnase-Immunity Protein Complexes .1. Diffusion-Controlled Association and Femtomolar Binding for the Cognate Complex. *Biochemistry* **34**, 13743-13750

129. Shen, B. J., Hage, T., and Sebald, W. (1996) Global and local determinants for the kinetics of interleukin-4/interleukin-4 receptor alpha chain interaction - A biosensor study employing recombinant interleukin-4-binding protein. *Eur. J. Biochem.* **240**, 252-261

130. Zhou, H. X. (2001) Disparate Ionic-Strength Dependencies of On and Off Rates in Protein–Protein Association. *Biopolymers* **59**, 427-433

131. Alsallaq, R., and Zhou, H. X. (2008) Electrostatic rate enhancement and transient complex of protein-protein association. *Proteins Struct. Funct. Bioinf.* **71**, 320-335

132. Alsallaq, R., and Zhou, H.-X. (2007) Prediction of protein-protein association rates from a transition-state theory. *Structure* **15**, 215-224

133. Pilling, M., and Seakins, P. (1995) *Reaction Kinetics*, Oxford University Press, Oxford

134. Szabo, A., Shoup, D., Northrup, S., and McCammon, J. A. (1982) Stochastically gated diffusion-influenced reactions. *J. Chem. Phys.* **77**, 4484-4493

135. Sommer, J., Jonah, C., Fukuda, R., and Bersohn, R. (1982) Production and subsequent 2nd-order decomposition of protein disulfide anions - lengthy collisions between proteins. *J. Mol. Biol.* **159**, 721-744

136. Camacho, C., Kimura, S., DeLisi, C., and Vajda, S. (2000) Kinetics of desolvation-mediated protein-protein binding. *Biophysical J.* **78**, 1094-1105

137. Camacho, C., Weng, Z., Vajda, S., and DeLisi, C. (1999) Free energy landscapes of encounter complexes in protein-protein association. *Biophysical J.* **76**, 1166-1178

138. Northrup, S. H., Thomasson, K. A., Miller, C. M., Barker, P. D., Eltis, L. D., Guillemette, J. G., Inglis, S. C., and Mauk, A. G. (1993) Effects of charged amino acid mutations on the bimolecular kinetics of reduction of yeast iso-1-ferricytochrome c by bovine ferrocytochrome b5. *Biochemistry* **32**, 6613-6623

139. Vijayakumar, M., Wong, K. Y., Schreiber, G., Fersht, A. R., Szabo, A., and Zhou, H. X. (1998) Electrostatic enhancement of diffusion-controlled protein-protein association: Comparison of theory and experiment on barnase and barstar. *J. Mol. Biol.* **278**, 1015-1024

140. Schreiber, G., and Fersht, A. R. (1993) Interaction of barnase with its polypeptide inhibitor barstar studied by protein engineering. *Biochemistry* **32**, 5145-5150

141. Escobar, L., Root, M. J., and MacKinnon, R. (1993) Influence of protein surface charge on the bimolecular kinetics of a potassium channel peptide inhibitor. *Biochemistry* **32**, 6982-6987

142. Wallis, R., Leung, K. Y., Pommer, A. J., Videler, H., Moore, G. R., James, R., and Kleanthous, C. (1995) Protein-protein interactions in colicin E9 DNase-immunity protein complexes. 2. Cognate and noncognate interactions that span the millimolar to femtomolar affinity range. *Biochemistry* **34**, 13751-13759

143. Wendt, H., Leder, L., Harma, H., Jelesarov, I., Baici, A., and Bosshard, H. R. (1997) Very rapid, ionic strength-dependent association and folding of a heterodimeric leucine zipper. *Biochemistry* **36**, 204-213

144. Volkov, A. N., Ubbink, M., and van Nuland, N. A. J. (2010) Mapping the encounter state of a transient protein complex by PRE NMR spectroscopy. *J. Biomol. NMR* **48**, 225-236

145. Tang, C., Iwahara, J., and Clore, G. M. (2006) Visualization of transient encounter complexes in protein-protein association. *Nature* **444**, 383-386
146. Sydor, J. R., Engelhard, M., Wittinghofer, A., Goody, R. S., and Herrmann, C. (1998) Transient kinetic studies on the interaction of ras and the Ras-binding domain of c-Raf-1 reveal rapid equilibration of the complex. *Biochemistry* **37**, 14292-14299
147. Stone, S. R., Dennis, S., and Hofsteenge, J. (1989) Quantitative evaluation of the contribution of ionic interactions to the formation of the thrombin-hirudin complex. *Biochemistry* **28**, 6857-6863
148. Taylor, M. G., Rajpal, A., and Kirsch, J. F. (1998) Kinetic epitope mapping of the chicken lysozyme.HyHEL-10 Fab complex: delineation of docking trajectories. *Protein Sci.* **7**, 1857-1867
149. Altschuh, D., Dubs, M. C., Weiss, E., Zeder-Lutz, G., and Van Regenmortel, M. H. (1992) Determination of kinetic constants for the interaction between a monoclonal antibody and peptides using surface plasmon resonance. *Biochemistry* **31**, 6298-6304
150. England, P., Bregegere, F., and Bedouelle, H. (1997) Energetic and kinetic contributions of contact residues of antibody D1.3 in the interaction with lysozyme. *Biochemistry* **36**, 164-172
151. Vallurupalli, P., Hansen, D. F., Stollar, E., Meirovitch, e., and Kay, L. E. (2007) Measurement of bond vector orientations in invisible excited states of proteins. *Proc. Natl. Acad. Sci. USA* **104**, 18473–18477
152. Demers, J. P., and Mittermaier, A. (2009) Binding Mechanism of an SH3 Domain Studied by NMR and ITC. *J. Am. Chem. Soc.* **131**, 4355-4367
153. Mittermaier, A. K., and Kay, L. E. (2009) Observing biological dynamics at atomic resolution using NMR. *Trends Biochem. Sci.* **34**, 601-611
154. Palmer, A. G., Kroenke, C. D., and Loria, J. P. (2001) NMR methods for quantifying microsecond-to-millisecond motions in biological macromolecules. *Methods Enzymol.* **339**, 204-238
155. Hansen, A. F., Vallurupalli, P., and Kay, L. E. (2008) An improved ^{15}N relaxation dispersion experiment for the measurement of millisecond time-scale dynamics in proteins. *J. Phys. Chem. B* **112**, 5898-5904
156. Yu, H., Chen, J. K., Feng, S., Dalgarno, D. C., Brauer, A. W., and Schreiber, S. L. (1994) Structural basis for the binding of proline-rich peptides to SH3 domains. *Cell* **76**, 933-945
157. Mayer, B. J. (2001) SH3 domains: complexity in moderation. *J. Cell Sci.* **114**, 1253-1263
158. Hansen, D. F., Vallurupalli, P., Lundstrom, P., Neudecker, P., and Kay, L. E. (2008) Probing Chemical Shifts of Invisible States of Proteins with Relaxation Dispersion NMR Spectroscopy: How Well Can We Do? *J. Am. Chem. Soc.* **130**, 2667-2675
159. Feng, S. B., Kasahara, C., Rickles, R. J., and Schreiber, S. L. (1995) Specific interactions outside the proline-rich core of two classes of Src homology 3 ligands. *Proc. Natl. Acad. Sci. U. S. A.* **92**, 12408-12415
160. Mittermaier, A., and Kay, L. E. (2004) The response of internal dynamics to hydrophobic core mutations in the SH3 domain from the Fyn tyrosine kinase. *Protein Sci.* **13**, 1088-1099
161. Bolzani, R., Ruggeri, F., and Olivo, O. M. (1979) Average normal temperature of the chicken in the morning and after 1-2 days of fasting. *Bollettino della Societa italiana di biologia sperimentale* **55**, 1618-1622

162. Wishart, D. S., Bigam, C. G., Yao, J., Abildgaard, F., Dyson, H. J., Oldfield, E., Markley, J. L., and Sykes, B. D. (1995) ^{1}H, ^{13}C and ^{15}N chemical shift referencing in biomolecular NMR. *J. Biomol. NMR* **6**, 135-140
163. Luz, Z., and Meiboom, S. (1963) Nuclear Magnetic Resonance Study of the Protolysis of Trimethylammonium Ion in Aqueous Solution—Order of the Reaction with Respect to Solvent. *J. Chem. Phys.* **39**, 366
164. Carver, J. P., and Richards, R. E. (1972) A general two-site solution for the chemical exchange produced dependence of T2 upon the Carr-Purcell pulse separation. *J. Magn. Reson.* **6**, 89-105
165. Ishima, R., and Torchia, D. (2005) Error estimation and global fitting in transverse-relaxation dispersion experiments to determine chemical-exchange parameters. *J. Biomol. NMR* **32**, 41-54
166. Efron, B., and Tibshirani, R. (1986) Bootstrap methods for standard errors, confidence intervals and other measures of statistical accuracy. *Stat. Sci.* **1**, 54-77
167. Di Nardo, A. A., Larson, S. M., and Davidson, A. R. (2003) The relationship between conservation, thermodynamic stability, and function in the SH3 domain hydrophobic core. *Journal of Molecular Biology* **333**, 641-655
168. Cantor, C., and Schimmel, P. (1980) *Biophysical Chemistry Part III: The behaviour of biological macromolecules*, W.H. Freeman and Co.
169. Pace, C. N., Vajdos, F., Fee, L., Grimsley, G., and Gray, T. (1995) How to Measure and Predict the Molar Absorption Coefficient of a Protein. *Prot. Sci.*

4, 2411-2423
170. Smith, A. J. (1997) Amino Acid Analysis. *Meth. Enz.* **289**, 419-426
171. Melander, W., and Horvath, C. (1977) Salt effects on hydrophobic interactions in precipitation and chromatography of proteins - interpretation of lyotropic series. *Arch. Biochem. Biophys.* **183**, 200-215
172. Bennaim, A., and Yaacobi, M. (1974) Effects of solutes on strength of hydrophobic interaction and its temperature-dependence. *Journal of Physical Chemistry* **78**, 170-175
173. Docherty, H., Galindo, A., Sanz, E., and Vega, C. (2007) Investigation of the salting out of methane from aqueous electrolyte solutions using computer simulations. *J. Phys. Chem. B* **111**, 8993-9000
174. Segur, J. B., and Oberstar, H. E. (1951) Viscosity of glycerol and its aqueous solutions. *Industrial and Engineering Chemistry* **43**, 2117-2120
175. Schreiber, G. (2002) Kinetic studies of protein-protein interactions. *Curr. Opin. Struct. Biol.* **12**, 41-47
176. Eyring, H. (1935) The Activated Complex in Chemical Reactions. *J. Chem. Phys.* **3**, 107-115
177. Wherland, S., and Gray, H. B. (1976) Metalloprotein electron-transfer reactions - analysis of reactivity of horse heart cytochrome-C with inorganic complexes. *Proc. Natl. Acad. Sci. U. S. A.* **73**, 2950-2954
178. Alberty, R. A., and Hammes, G. G. (1958) Application of the theory of diffusion-controlled reactions to enzyme kinetics. *Journal of Physical Chemistry* **62**, 154-159
179. Buckle, A. M., Schreiber, G., and Fersht, A. R. (1994) Protein-protein recognition - crystal structural-analysis of a barnase barstar complex at 2.0-angstrom resolution. *Biochemistry* **33**, 8878-8889

180. Xu, D., Lin, S. L., and Nussinov, R. (1997) Protein binding versus protein folding: The role of hydrophilic bridges in protein associations. *J. Mol. Biol.* **265**, 68-84
181. Fitos, I., Heremans, K., and Loontiens, F. G. (1979) Binding Study of 4-Methylumbelliferyl Alpha-D-Mannopyranoside to Dimeric Concanavalin-a under High-Pressure. *React Kinet Catal L* **12**, 393-397
182. Li, T. M., Hook, J. W., Drickamer, H. G., and Weber, G. (1976) Effects of Pressure Upon Fluorescence of Riboflavin Binding-Protein and Its Flavin Mononucleotide Complex. *Biochemistry* **15**, 3205-3211
183. Heremans, K., Snauwaert, J., and Rijkenberg, J. (1980) Stopped-Flow Apparatus for the Study of Fast Reactions in Solution under High-Pressure. *Rev Sci Instrum* **51**, 806-808
184. Torgerson, P. M., Drickamer, H. G., and Weber, G. (1979) Inclusion Complexes of Poly-Beta-Cyclodextrin - Model for Pressure Effects Upon Ligand-Protein Complexes. *Biochemistry* **18**, 3079-3083
185. Torgerson, P. M., Drickamer, H. G., and Weber, G. (1980) Effect of Hydrostatic-Pressure Upon Ethidium-Bromide Association with Transfer Ribonucleic-Acid. *Biochemistry* **19**, 3957-3960
186. Visser, A. J. W. G., Li, T. M., Drickamer, H. G., and Weber, G. (1977) Volume Changes in Formation of Internal Complexes of Flavinyltryptophan Peptides. *Biochemistry* **16**, 4883-4886
187. Dubins, D. N., Filfil, R., Macgregor, R. B., and Chalikian, T. V. (2000) Role of water in protein-ligand interactions: Volumetric characterization of the binding of 2 '-CMP and 3 '-CMP to ribonuclease A. *J Phys Chem B* **104**, 390-401
188. Brandts, J. F., Oliveira, R. J., and Westort, C. (1970) Thermodynamics of Protein Denaturation - Effect of Pressure on Denaturation of Ribonuclease-A. *Biochemistry* **9**, 1038-&
189. Gill, S. J., and Glogovsk.Rl. (1965) Influence of Pressure on Reversible Unfolding of Ribonuclease and Poly-Gamma-Benzyl-L-Glutamate. *Journal of Physical Chemistry* **69**, 1515-&
190. Hawley, S. A. (1971) Reversible Pressure-Temperature Denaturation of Chymotrypsinogen. *Biochemistry* **10**, 2436-&
191. Frye, K. J., and Royer, C. A. (1998) Probing the contribution of internal cavities to the volume change of protein unfolding under pressure. *Protein Science* **7**, 2217-2222
192. Rouget, J. B., Aksel, T., Roche, J., Saldana, J. L., Garcia, A. E., Barrick, D., and Royer, C. A. (2011) Size and Sequence and the Volume Change of Protein Folding. *J Am Chem Soc* **133**, 6020-6027
193. Schweiker, K. L., Fitz, V. W., and Makhatadze, G. I. (2009) Universal Convergence of the Specific Volume Changes of Globular Proteins upon Unfolding. *Biochemistry* **48**, 10846-10851
194. Roche, J., Caro, J. A., Norberto, D. R., Barthe, P., Roumestand, C., Schlessman, J. L., Garcia, A. E., Garcia-Moreno, B., and Royer, C. A. (2012) Cavities determine the pressure unfolding of proteins. *Proceedings of the National Academy of Sciences of the United States of America* **109**, 6945-6950
195. Low, P. S., and Somero, G. N. (1975) Protein Hydration Changes during Catalysis - New Mechanism of Enzymic Rate-Enchancement and Ion Activation Inhibition of Catalysis. *P Natl Acad Sci USA* **72**, 3305-3309
196. Schramm, V. L. (1998) Enzymatic transition states and transition state analog design. *Annu Rev Biochem* **67**, 693-720

197. Schreiber, G., and Fersht, A. R. (1993) Interaction of barnase with its polypeptide inhibitor barstar studied by protein engineering. *Biochemistry* **32**, 5145-5150
198. Altschuh, D., Dubs, M. C., Weiss, E., Zederlutz, G., and Vanregenmortel, M. H. V. (1992) Determination of Kinetic Constants for the Interaction between a Monoclonal-Antibody and Peptides Using Surface-Plasmon Resonance. *Biochemistry* **31**, 6298-6304
199. Mittermaier, A., and Kay, L. E. (2006) Review - New tools provide new insights in NMR studies of protein dynamics. *Science* **312**, 224-228
200. Palmer, A. G., 3rd, Kroenke, C. D., and Loria, J. P. (2001) Nuclear magnetic resonance methods for quantifying microsecond-to-millisecond motions in biological macromolecules. *Methods Enzymol* **339**, 204-238
201. Chalikian, T. V., and Filfil, R. (2003) How large are the volume changes accompanying protein transitions and binding? *Biophys Chem* **104**, 489-499
202. Yu, H. T., Chen, J. K., Feng, S. B., Dalgarno, D. C., Brauer, A. W., and Schreiber, S. L. (1994) Structural Basis for the Binding of Proline-Rich Peptides to Sh3 Domains. *Cell* **76**, 933-945
203. Low, P. S., and Somero, G. N. (1975) Activation Volumes in Enzymic Catalysis - Their Sources and Modification by Low-Molecular-Weight Solutes. *Proceedings of the National Academy of Sciences of the United States of America* **72**, 3014-3018
204. Mittermaier, A., and Kay, L. E. (2004) The response of internal dynamics to hydrophobic core mutations in the SH3 domain from the Fyn tyrosine kinase. *Protein Science* **13**, 1088-1099
205. Dellarole, M., and Royer, C. A. (2014) High-pressure fluorescence applications. *Methods Mol Biol* **1076**, 53-74
206. Lee, B., and Richards, F. M. (1971) Interpretation of Protein Structures - Estimation of Static Accessibility. *Journal of Molecular Biology* **55**, 379-&
207. Richards, F. M. (1977) Areas, Volumes, Packing, and Protein-Structure. *Annual Review of Biophysics and Bioengineering* **6**, 151-176
208. Connolly, M. L. (1983) Analytical Molecular-Surface Calculation. *Journal of Applied Crystallography* **16**, 548-558
209. Voss, N. R., and Gerstein, M. (2010) 3V: cavity, channel and cleft volume calculator and extractor. *Nucleic Acids Research* **38**, W555-W562
210. Ogura, K., and Okamura, H. (2013) Conformational change of Sos-derived proline-rich peptide upon binding Grb2 N-terminal SH3 domain probed by NMR. *Scientific Reports* **3**
211. Musacchio, A., Saraste, M., and Wilmanns, M. (1994) High-Resolution Crystal-Structures of Tyrosine Kinase Sh3 Domains Complexed with Proline-Rich Peptides. *Nature Structural Biology* **1**, 546-551
212. Dundas, J., Ouyang, Z., Tseng, J., Binkowski, A., Turpaz, Y., and Liang, J. (2006) CASTp: computed atlas of surface topography of proteins with structural and topographical mapping of functionally annotated residues. *Nucleic Acids Research* **34**, W116-W118
213. Paci, E., and Velikson, B. (1997) On the volume of macromolecules. *Biopolymers* **41**, 785-797
214. Chalikian, T. V., and Breslauer, K. J. (1996) On volume changes accompanying conformational transitions of biopolymers. *Biopolymers* **39**, 619-626
215. Goldstein, J. L., and Brown, M. S. (1990) Regulation of the mevalonate pathway. *Nature* **343**, 425-430
216. Buhaescu, I., and Izzedine, H. (2007) Mevalonate pathway: a review of clinical and therapeutical implications. *Clin Biochem* **40**, 575-584

217. Dunford, J. E. (2010) Molecular Targets of the Nitrogen Containing Bisphosphonates: The Molecular Pharmacology of Prenyl Synthase Inhibition. *Current Pharmaceutical Design* **16**, 2961-2969

218. Ebetino, F. H., Hogan, A. M. L., Sun, S. T., Tsoumpra, M. K., Duan, X. C., Triffitt, J. T., Kwaasi, A. A., Dunford, J. E., Barnett, B. L., Oppermann, U., Lundy, M. W., Boyde, A., Kashemirov, B. A., McKenna, C. E., and Russell, R. G. G. (2011) The relationship between the chemistry and biological activity of the bisphosphonates. *Bone* **49**, 20-33

219. Russell, R. G. G. (2011) Bisphosphonates: The first 40 years. *Bone* **49**, 2-19

220. Fournier, P. G., Stresing, V., Ebetino, F. H., and Clezardin, P. (2010) How Do Bisphosphonates Inhibit Bone Metastasis In Vivo? *Neoplasia* **12**, 571-578

221. Zhang, Y. H., Cao, R., Yin, F., Hudock, M. P., Guo, R. T., Krysiak, K., Mukherjee, S., Gao, Y. G., Robinson, H., Song, Y., No, J. H., Bergan, K., Leon, A., Cass, L., Goddard, A., Chang, T. K., Lin, F. Y., Van Beek, E., Papapoulos, S., Wang, A. H. J., Kubo, T., Ochi, M., Mukkamala, D., and Oldfield, E. (2009) Lipophilic Bisphosphonates as Dual Farnesyl/Geranylgeranyl Diphosphate Synthase Inhibitors: An X-ray and NMR Investigation. *Journal of the American Chemical Society* **131**, 5153-5162

222. Mao, J. H., Mukherjee, S., Zhang, Y., Cao, R., Sanders, J. M., Song, Y. C., Zhang, Y. H., Meints, G. A., Gao, Y. G., Mukkamala, D., Hudock, M. P., and Oldfield, E. (2006) Solid-state NMR, crystallographic, and computational investigation of Bisphosphonates and farnesyl diphosphate synthase-bisphosphonate complexes. *Journal of the American Chemical Society* **128**, 14485-14497

223. De Schutter, J. W., Zaretsky, S., Welbourn, S., Pause, A., and Tsantrizos, Y. S. (2010) Novel bisphosphonate inhibitors of the human farnesyl pyrophosphate synthase. *Bioorganic & Medicinal Chemistry Letters* **20**, 5781-5786

224. Dunford, J. E., Kwaasi, A. A., Rogers, M. J., Barnett, B. L., Ebetino, F. H., Russell, R. G. G., Oppermann, U., and Kavanagh, K. L. (2008) Structure-activity relationships among the nitrogen containing bisphosphonates in clinical use and other analogues: Time-dependent inhibition of human farnesyl pyrophosphate synthase. *Journal of Medicinal Chemistry* **51**, 2187-2195

225. Cai, M., Huang, Y., Sakaguchi, K., Clore, G. M., Gronenborn, A. M., and Craigie, R. (1998) An efficient and cost-effective isotope labeling protocol for proteins expressed in Escherichia coli. *J Biomol NMR* **11**, 97-102

226. Leung, C. Y., Park, J., De Schutter, J. W., Sebag, M., Berghuis, A. M., and Tsantrizos, Y. S. (2013) Thienopyrimidine Bisphosphonate (ThPBP) Inhibitors of the Human Farnesyl Pyrophosphate Synthase: Optimization and Characterization of the Mode of Inhibition. *Journal of Medicinal Chemistry* **56**, 7939-7950

227. Park, J., Lin, Y. S., De Schutter, J. W., Tsantrizos, Y. S., and Berghuis, A. M. (2012) Ternary complex structures of human farnesyl pyrophosphate synthase bound with a novel inhibitor and secondary ligands provide insights into the molecular details of the enzyme's active site closure. *Bmc Structural Biology* **12**

228. Pervushin, K., Riek, R., Wider, G., and Wuthrich, K. (1997) Attenuated T-2 relaxation by mutual cancellation of dipole-dipole coupling and chemical shift anisotropy indicates an avenue to NMR structures of very large biological macromolecules in solution. *Proceedings of the National Academy of Sciences of the United States of America* **94**, 12366-12371

229. Religa, T. L., Ruschak, A. M., Rosenzweig, R., and Kay, L. E. (2011) Site-Directed Methyl Group Labeling as an NMR Probe of Structure and Dynamics in Supramolecular Protein

Systems: Applications to the Proteasome and to the ClpP Protease. *Journal of the American Chemical Society* **133**, 9063-9068

230. Larda, S. T., Bokoch, M. P., Evanics, F., and Prosser, R. S. (2012) Lysine methylation strategies for characterizing protein conformations by NMR. *Journal of Biomolecular Nmr* **54**, 199-209

231. Liu, X. Y., Hanson, L., Langan, P., and Viola, R. E. (2007) The effect of deuteration on protein structure: a high-resolution comparison of hydrogenous and perdeuterated haloalkane dehalogenase. *Acta Crystallographica Section D-Biological Crystallography* **63**, 1000-1008

232. Tugarinov, V., Kanelis, V., and Kay, L. E. (2006) Isotope labeling strategies for the study of high-molecular-weight proteins by solution NMR spectroscopy. *Nature Protocols* **1**, 749-754

233. Hansen, A. L., and Kay, L. E. (2011) Quantifying millisecond time-scale exchange in proteins by CPMG relaxation dispersion NMR spectroscopy of side-chain carbonyl groups. *J Biomol NMR* **50**, 347-355

234. Niesen, F. H., Berglund, H., and Vedadi, M. (2007) The use of differential scanning fluorimetry to detect ligand interactions that promote protein stability. *Nature Protocols* **2**, 2212-2221

235. Vedadi, M., Niesen, F. H., Allali-Hassani, A., Fedorov, O. Y., Finerty, P. J., Wasney, G. A., Yeung, R., Arrowsmith, C., Ball, L. J., Berglund, H., Hui, R., Marsden, B. D., Nordlund, P., Sundstrom, M., Weigelt, J., and Edwards, A. M. (2006) Chemical screening methods to identify ligands that promote protein stability, protein crystallization, and structure determination. *Proceedings of the National Academy of Sciences of the United States of America* **103**, 15835-15840

236. Jahnke, W., Rondeau, J. M., Cotesta, S., Marzinzik, A., Pelle, X., Geiser, M., Strauss, A., Gotte, M., Bitsch, F., Hemmig, R., Henry, C., Lehmann, S., Glickman, J. F., Roddy, T. P., Stout, S. J., and Green, J. R. (2010) Allosteric non-bisphosphonate FPPS inhibitors identified by fragment-based discovery. *Nature Chemical Biology* **6**, 660-666